IMPLANTABLE OPTICAL NEURO STIMULATORS WITH WIRELESS POWER AND DATA TELEMETRY

By

Wasif Afsari Khan

A DISSERTATION

Submitted to
Michigan State University
in partial fulfillment of the requirements
for the degree of

Electrical Engineering - Doctor of Philosophy

2020

ABSTRACT

IMPLANTABLE OPTICAL NEURO STIMULATORS WITH WIRELESS POWER AND DATA TELEMETRY

By

Wasif Afsari Khan

Neural interfaces provide a direct communication pathway between nervous systems and the external environment. Clinical and therapeutic treatments for neurological diseases and events such as spinal cord injury, stroke, and traumatic major amputations have gained a promising pace through the introduction of these interfaces. Some Artificial neural interface relies on electrical signals to evoke sensation in the central- and peripheral- nervous systems (CNS and PNS respectively), and have most commonly been used in the scientific practice for decades. However, due to the limitations and difficulties of electrical stimulation, these neural interfaces require improved technology. Optogenetics, a recent and fascinating technique that combines optics and genetics, has established its ability by direct optical stimulation of genetically modified target neuron population and achieving sub-millisecond temporal precision. As neuron stimulation in optogenetics is achieved by light, efficient and validated engineered light delivery tools are of great importance towards an effective experiment or clinical trial.

This dissertation provides a development process towards a wireless and fully implantable micro-LED based opto-neuro stimulator. GaN micro LED's were the source of the optical stimulation and a process was described for the fabrication, etching morphology and characterization of such LED's. In order to enhance the optical efficiency, a micro optic element (reflector) was coupled with the LED stimulator and the electrical, optical and thermal characteristics of the as-fabricated

neuro stimulator were characterized.

In order to realize a untethered optical neuromodulation and simultaneous neural data recording, a head mounted battery powered module has been developed, coupled with a 4 channel μ-LED array stimulator and a 2 channel recording electrode. This module can wirelessly transmit and receive signals using Bluetooth low energy (BLE), store data in a PC and simultaneously show real time neural recordings on a GUI. Efficacy of the stimulation was validated by c-Fos biomarker detection and signal processing indicating phase lock synchrony.

Finally, a demonstration of an intensity enhanced, miniaturized (millimeter scale), single channel optical stimulator has been developed, capable of being wirelessly powered through a transmitter (Tx) and millimeter scale receiver (Rx) coil link. The fabrication methods have been discussed with the electrical, optical, and thermal characteristics of the stimulator being quantified. The effect of two coil alignment were verified both from simulation and from experimental results. Sufficient power transfer (4mW) was achieved to drive the stimulator at a low frequency (96MHz), and an immunohistology analysis showing effective neuron activation with c-Fos biomarker expression establishes the efficacy of the stimulation.

ACKNOWLEDGEMENTS

This dissertation would not be complete without acknowledging my advisor Dr. Wen Li for her guidance throughout my graduate training period. Dr. Li's support, mentorship and insightful suggestions allowed the works mentioned in this dissertation to come to a reality.

I want to offer my gratitude to my committee members: Dr. Tim Hogan, Dr. Premjeet Chahal and Dr. Erin Purcell for their support and suggestions towards my research. I want to express my gratitude to our collaborators Dr. Maysam Ghovanloo and Dr. Yaoyao Jia for their assistance with the circuits and data processing, Dr. Arthur Weber and Ms. Fatma Madi for their assistance in histology and animal surgeries, Dr. Erin Purcell and Ms. Monica Setien for their support with the in vitro experiments. This works in this dissertation would not have been possible without the help from our learned collaborators.

My sincere thanks goes to my colleagues from Micro-technology lab: Dr. Ki Yong Kwon, Dr. Xiaopeng Bi, Dr. Bin Fan, Yue Guo, Weiyang Yang and Yan Gong for their help and support during my doctoral training. Colleagues at Michigan State University, especially Dr. Baokang Bi from Keck Microfabrication Facility and Mr. Brian Wright from ECE shop for their numerous suggestions and help.

I have received guidance and support, both in academic and emotional perspective from my friends. Although during my doctoral training I might not have been able to catch up with them

regularly, but they kept providing emotional support and feedback to make the journey a smoother one.

Finally, and most importantly, I would like to thank my family. During the confusing times when I was kept losing faith on my abilities, my family have put their faith and trust on me to achieve bigger things.

Thank You!

TABLE OF CONTENTS

LIST OF TABLES

LIST OF FIGURES

Chapter 1. Introduction

1.1 Background

Optogenetics, the "Nature method of the year 2010", is a fast growing technology that expands its applications in fundamental neuroscience[1]–[3], brain mapping[4], gene therapy[5] and also for discovery of new medical approaches[6] to fight a variety of neurological diseases, such as Parkinson's, neuropsychiatric diseases, and vision impairments[7], [8]. This is a technology that combines optical and genetic approaches to achieve function of events within cells of living tissues. Function of events could indicate the activation or inhibition of a neuron if this technique is performed on the nervous system[9]. In neuroscience applications, it is a technique to control and monitor the activities of neurons in living tissue—even within freely-moving animals[10], [11]—and to measure the effects of those manipulations in real time.

Optogenetics could be classified to have 3 primary components[12]. The first one involves microbial opsins[13], which are members of organism families such as algae and archaebacterial, and these organisms consist genes to encode a distinct protein which in application of sufficient and specific wavelength of light elicit electrical current[12] across cellular membranes by creating ion channels. The second component is the general method for targeting sufficiently strong and specific opsin gene expression to well-defined cellular elements in the brain while the third component being the general methods for providing intense, precisely timed and specific wavelength light[12] towards target brain regions, cells or parts of cells as the experimental subject (rodent, primates) carries out behaviors of interest simultaneously.

Expanding on the first component, the microbial opsin-which are proteins that transduce photons into electrical current. Three families of these opsins have commonly found their use in optogenetics. The excitatory channel rhodopsin (ChR2) creates sodium ion channels on the membranes of the target neurons[13], and the application of light ensures flow of positive sodium ion into the cell as the channel opens. Influx of Na+ ion depolarizes the neuron from its rest potential (-70mV). Sufficient depolarization would cause the neuron to generate an action potential (also known as a spike or impulse) and thus activating or turning 'on' the target neuron[14]. The
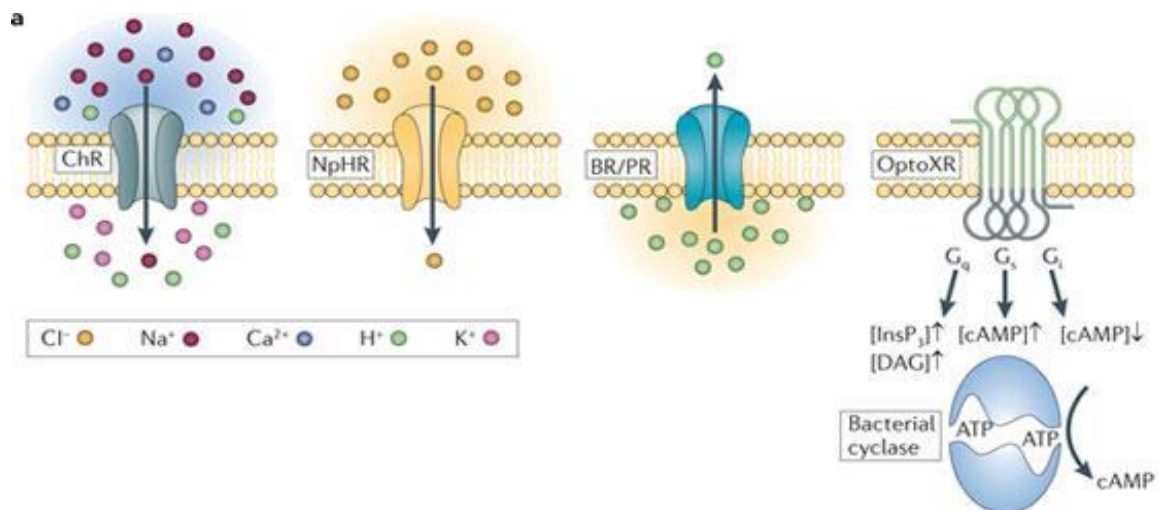
Figure 1-1. Channelrhodopsin, Halorhodopsin and Bacteriorhodopsin and their mechanisms in optogenetic stimulation. Adapted from [8].

ChR2 is maximally excited by a wavelength of 470nm[15] (blue region in the visible spectrum) and requires a minimum optical irradiance of $1mW/mm^2$ [16], [17] [15]for effective activation, and 5 mW/mm^2 [17] for faster off kinetics. The halo-rhodopsin (inhibitory) creates chloride ions and with the application of 589nm [18] (yellow light) and a minimum of $7mW/mm^2$ intensity light, the opsin pumps chloride ions out of the cell body. The chloride efflux hyperpolarizes the cell membrane,

and effectively turns 'off' the cell by suppressing the action potentials. The bacteriorhodopsin/ proteo rhodopsin (BR/PR) pump protons out of the cell thereby inhibiting the neurons by making it harder to generate action potentials[18], [19].

Although the initial incidence of the microbial opsins was reported back in 1971[20], it was not until 2007 that the mammalian behavioral ultimately came to completion[21], and indicating that the microbial opsins will come into helpful uses. Much work has been done to achieve a well-tolerated and stable expression of the crucial vectors, then to test and acquire the real time readouts through their electrophysiology and behavior in vitro[22]. Moving towards the crucial in vivo experiment and readout eventually motivated the design and implementation of bi-directional neural interfaces for in vivo[23] light delivery. Researchers managed to selectively target a microbial opsin gene within a defined population of neurons deep in the brain of adult mice with significant specificity and penetrance[21]. Later, activation patterns from those cells were obtained through an optical fiber and simultaneous multimodal system readouts via electroencephalography (EEG) and electromyography (EMG) that described the sleep/wake status[21] of those rodents. These experiments demonstrated the causal role in sleep/wake transitions for the defined activity patterns, given a specific population of cells.
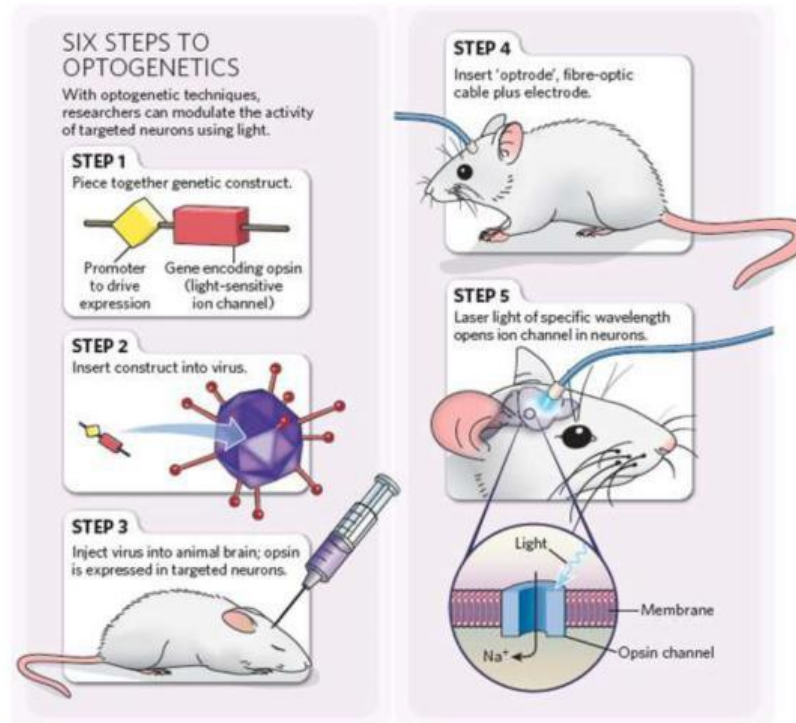
Figure 1-2. Steps of optogenetics. Adapted from [24]

The need to understand the neural circuitry of symptoms related to disease states have motivated a number of discoveries. The circuit level mechanisms and tissue level manifestations of neuropsychiatric disease have long been a mystery and the applications of optogenetics[25] are indicating a promising effort in discovering them. Studies of the cellular activity of seizure propagation[26] have demonstrated some of the first closed loop approaches in behaving animals[27]–[29], simultaneously identifying immediate seizure termination sites which are remote from the initiation sites[29]. Optogenetic investigations have also discovered the cells and pathways that promote or inhibit normal and parkinsonian movements[30], [31].

Before the outspread of optogenetic techniques, electrical neuromodulation[32] was executed to

stimulate a certain region of interest of the brain. Although electrical stimulation provided
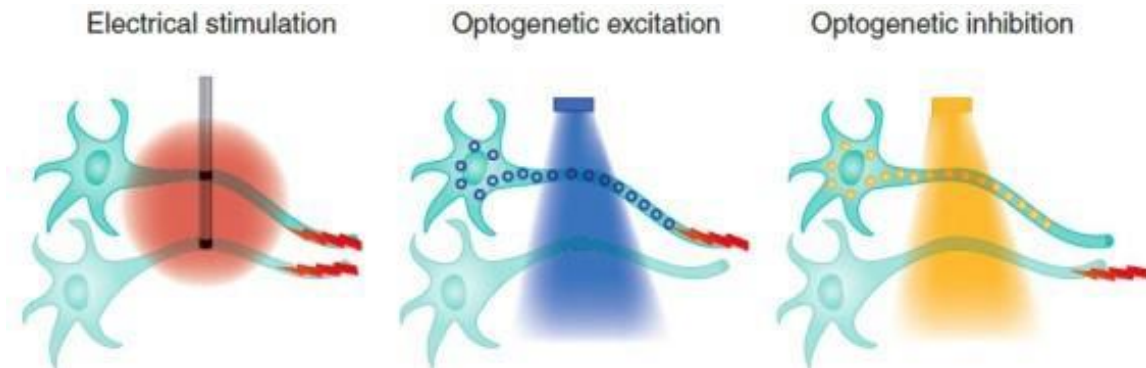
Figure 1-3. Electrical and optogenetic stimulation, adapted from [1]

groundbreaking results, however it should be noted that neurons are electrically interconnected and providing an electrical pulse usually stimulated all of the neurons within the vicinity. Cell level specificity is not possible to achieve using electrical stimulation and the spatial resolution is also lower when compared with optical stimulation, in specific cases where we consider the current spreading. Another advantage over electrical stimulation is the generation of minimal electrical artifacts and instrumental interference with electrophysiological recording[33], which thereby allows simultaneous recording of light-evoked neural activity. Generally, a conductive probe needs to be inserted into the brain for deep brain stimulations, which across time could damage and inflame the tissues of interest and could thereby compromise the purpose of the stimulation. However, insertion of probes or invasive surgeries are not exclusive in cases of electrical stimulations only, but also applicable for optogenetics too.

1.2 Challenges in the light delivery methods

From engineering perspective, the third component to deliver precisely timed and sufficiently

intense light to the target population of neurons is of great interest. Numerous optogenetics applications have inspired the development of optical stimulators as well as the instruments for light delivery. Although mammalian brain surfaces have been reported to have demonstrated opsin expressions[34]–[37] after optical stimulation and responses were mapped after acute exposure and light illumination, however, the deep regions of the brain still remained inaccessible to optogenetics and hence control of behavior had not been achieved[12]. It is therefore important indeed to develop a opto-neuro stimulator to safely, focally and flexibly deliver visible light to the deep brain regions of the freely behaving mammal. To ensure effective opsin expression and imaging needs, it is desirable to extract much high intensity at the neuro-stimulator interface, preferably greater than needed at the opsin-expressing cells themselves as dispersion and scattering losses are expected over the target neuron population.

1.3 Challenges while using micro LED's

Techniques that enable simultaneous optogenetic stimulation and recording with near cellular resolution typically features micro-structured features with recording and illumination/stimulation capabilities[38]. Light emitting diodes, along with electrical recording sites structured on a GaAs substrate to create an injectable needle, was reported, which enables the illumination and signal recording in a small space for high spatial resolution. The drawback is the low efficiency of the LEDs. This bottleneck in LED efficiency limit the emission power levels that can be achieved without adverse effects (>1.5 µW corresponding to 1 mW/mm^2 and 2°C increase in local temperature). The adverse effects could be explained as the cell damage, undesired artifacts in the recorded signals and alteration in cellular activity which could be linked

6

with the thermal load. These adverse conditions limit the activation depth to less than 100 µm with standard opsins, making broad illumination of larger brain areas difficult.

1.4 Layout of the dissertation

This work focuses on the development of a reflector coupled optical neural stimulator for optogenetics that aims toward intensity enhancement and furthermore, paves the path towards the development of a truly untethered optical stimulator, capable of wirelessly powered through miniaturized coil links, and coupled with a reflector for effective opsin expression by optogenetic stimulation, while fulfilling the requirements for biomedical implants (i.e. being biocompatible, low operating temperature increase). A battery powered head borne module has also been developed to stimulate and simultaneously record neural activity (ECoG), store the data in a PC for future analysis, and show real time neural activity on a GUI. In detail, chapter 2 discusses the general light delivery methods used in optogenetics, limited within tethered stimulators. Chapter 3 discusses the advances in the untethered optogenetic stimulators. Chapter 4 provides an approach towards the fabrication process for in house micro-LED production for optogenetic purposes, specifically targeted to the 473 nm excitation region of the ChR2 opsin. Chapter 5 demonstrates a method to enhance the optical intensity from a planar micro LED surface, by incorporating a reflector. In addition to intensity enhancement, this method effectively reduces the power consumption for a micro LED for a given intensity threshold. Chapter 6 illustrates an approach towards developing a head-mounted battery powered module capable of simultaneous stimulation, recording, data representation and data storing. Chapter 7 focuses on the concept of a miniaturized, wirelessly powered single channel neuro stimulator.

Chapter 2. A Review of Light Delivery Methods: Tethered Systems

One of the core components [12] of optogentics is the efficient delivery of specific wavelength and high intensity light to the genetically modified cell population for opsin expression- in order to achieve the desired inhibition or activation of neurons[39]. Much research has been done towards developing interfaces for efficient light delivery[40]–[43]. The light delivery methods have been evolved from high power Xenon lamps to fiber optic based focused stimulation, and more recently towards μLED arrays to provide more flexibility and better spatial resolution. From the device perspective, the fiber optic coupled stimulators gained much popularity due to their superior light intensity[18] while being coupled with a laser or a high power LED.

2.1 Laser coupled Optical fibers for light delivery

In examples where fiber optic based light delivery method demonstrated successful and effective expression of the opsins, the fiber in use was coupled to a powerful optical source (laser diode, LED) on one end[42], [44], the other end being inserted through the skull of the experimental animal using craniotomy. Figure 2-1 (a, b) shows an example of an optical fiber coupled stimulation
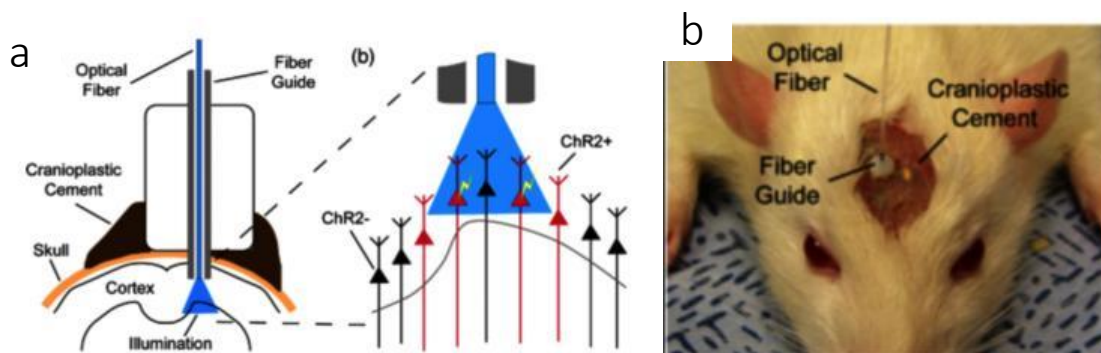
Figure 2-1. (a) Concept diagram of optical neural interface mounted on a rat skull, showing optical fiber guide, optical fiber inserted and blue light transmitted to the cortex. b) Close-up view of the optical neural interface showing fiber guide attached with translucent cranioplastic cement.

interface both as a schematic and as an experimental setup. The interface development took up

pace with the incorporation of laser diode–coupled fiber optics[11] and researchers were also

been able to incorporate other features with the optical fiber including heat isolation and activity

feedback, registering virus injection to illumination site- allowing new opportunities for targeted
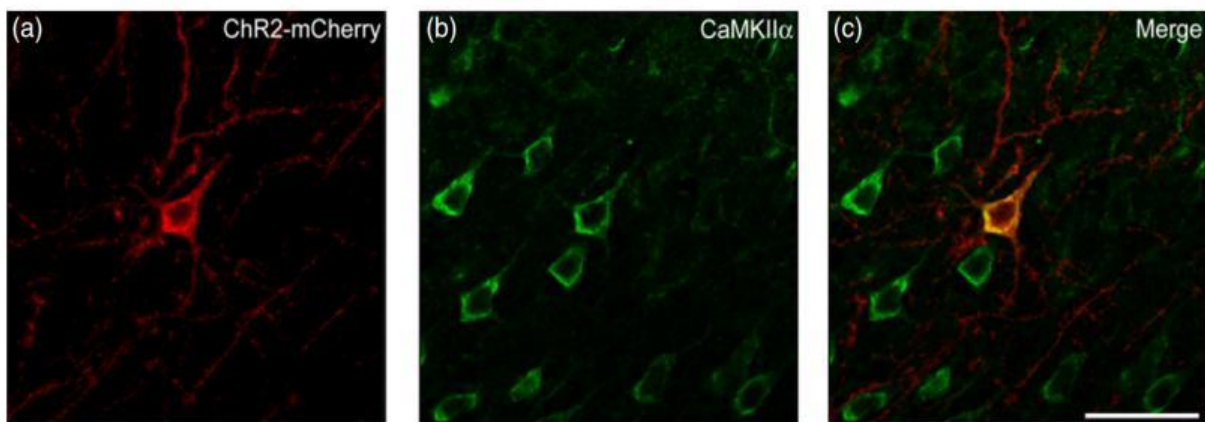
Figure 2-2. Cortical sections of mouse brains infected with lentiviruses carrying the ChR2-mCherry fusion protein under the CaMKIIα promoter were immuno-stained for mCherry. (b) Same section in (a) immunostained for the excitatory glutamatergic neuronal marker CaMKIIα. (c) Merged image of (a), (b) showing co-localization between ChR2-mCherry and CamKIIα. Adapted from [11]

control and readout while the experimental animal expresses behavior change. The core optical

technology described in [11] by Aravanis *et. al.* demonstrates a blue laser diode coupled to an

optical fiber, where the laser diode was capable of millisecond precision pulses to output 20 mW

of power at 473 nm. Coupling the optical source with a flexible stripped multimode optical fiber

generated 380 mW/mm^2 light intensity at the end, which was sufficient enough to excite the

genetically modified neurons even within millimeters of the fiber end and also accounted for the

attenuation. After immunohistochemistry, an observation of 95% ChR2-positive cells in the cortex

also expressing CaMKIIα validates the efficacy of the stimulator as CaMKIIα was used as the promoter to drive ChR2 expression, as seen in an example illustrated in Figure 2-2 (a-c).

2.2 LED coupled Optical fibers for light delivery

LED coupled optical fibers were another advancement for optical neural interfaces[45]–[48]. Nussinovitch *et. al* in [49] used a 2-mm- diameter-fiber-coupled monochromic LED (450 nm) in order to stimulate the ChR2 transgene site with flashes of blue light. The group used optogenetic stimulation to control cardiac excitability in a rat heart *in vivo* in order to demonstrate a biological pacemaker approach, in a clinically relevant manner. Similar approaches have also been mentioned in [50], [51], where the researchers aimed at controlling the heart beat rate using optogenetic stimulation, in order to mimic a clinical/biological pacemaker. Nussinovitch *et. al* were able to optogenetically induce the activation of the ventricle, by increasing the heart beat rate from 180 beats/min to 300 beats/min during stimulation. The success rate of the optical induction varied while using different frequencies of stimulation and also with the irradiance Figure 2-3 (a,c). On the other hand, the researchers did not observe any pacing due to stimulation to areas injected with the control virus, in the same hearts or in other animals. A close up view of the animal heart is shown in Figure 2-3 (b).
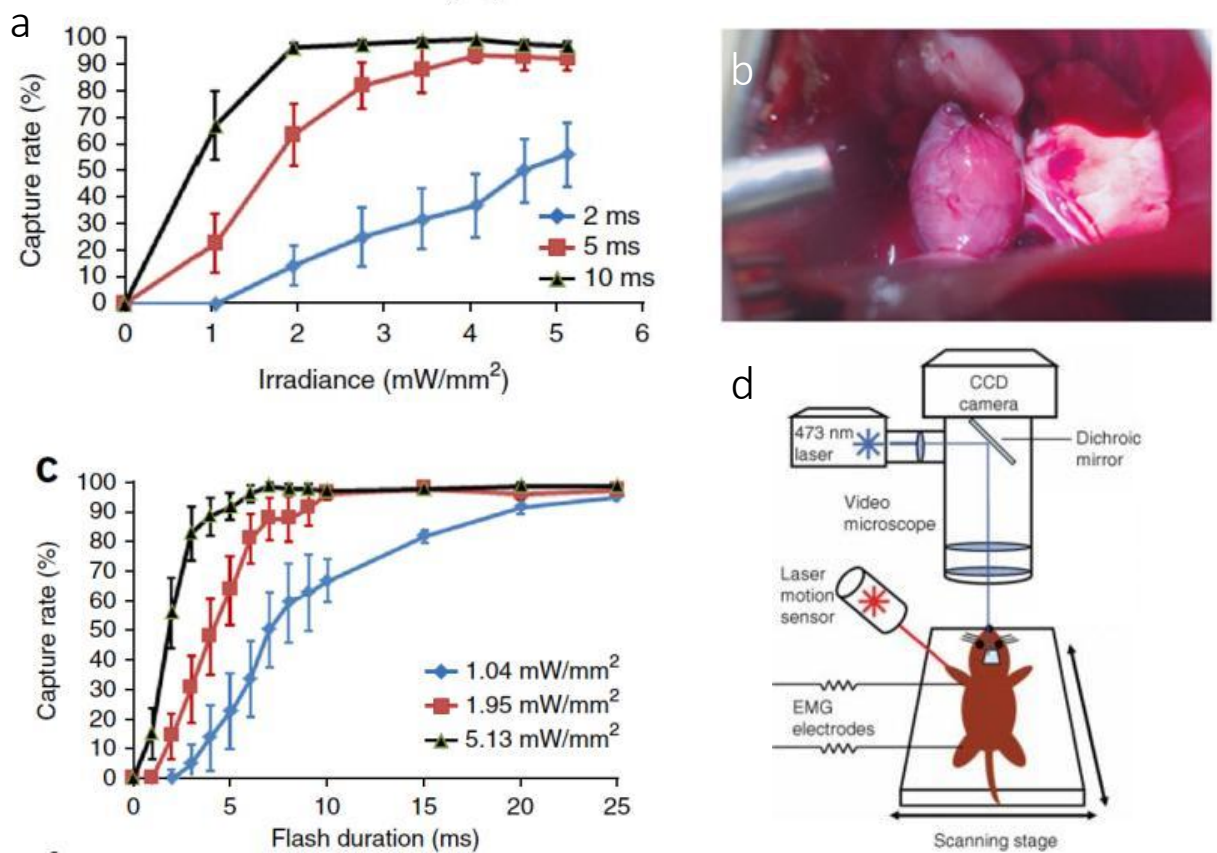
Figure 2-3. Response curves summarizing the effects of altering flash duration a) with respect to irradiance c) with respect to flash durations b) a photograph showing the experimental design, in which the heart was exposed and a LED-coupled fiber optic represented was placed in close proximity, adapted from [49] d) Anaesthetized mouse was placed on a scanning stage and was stimulated by a 473nm laser directed through a microscope objective, motor output was detected by EMG electrodes in front and hind-limb muscles, and by a laser motion sensor fixed with the stage. Adapted from [44].

2.3 Microscope focused light delivery

Other techniques to focus a collimated light beam to the target population of neurons using microscope have also been explored. As described in [44], Ayling *et. al.* used a 473 nm laser targeted through a simple microscope as seen in Figure 2-3 (d). In order to obtain a light based

mapping of the brain, a fixed mouse was moved relative to the focused laser beam. Electromyogram (EMG) and electroencephalogram (EEG) data was collected after delivering flashes of laser light towards the brain. Ayling *et. al.* observed that light intensity varying from 40-600 mW/mm^2 with a stimulus duration ranging 1-35 ms was sufficient enough to produce motor response (i.e. EMG response). However, a significantly large photo electric artefact [52]–[54] accompanies this method which was confirmed by observing the artefact while conducting the same experimental procedure on a control mouse[44].

2.4 Waveguide directed light delivery

Introduction of microscale out of plane waveguides improved the spatial resolution of the optical stimulators. Micro-machined, tapered tipped and thin out-of-plane waveguide shanks reduced implant invasiveness also. Usually for these devices, a butt coupled laser acted as the optical source and light being emitted from the tip of the shanks to provide multi-site stimulation. Integration with the UTAH multi electrode array probes enabled simultaneous stimulation and recording of neural activity[55]. One reported work is a SiO$_2$ Utah waveguide array[56] capable of optical stimulation with both visible and infrared (IR) light. Consisting of 10×10 arrays of optrodes with length of 0.5-2 mm at a 400 µm pitch, these waveguide arrays were bulk micromachined using fused silica or quartz diced at 50mm diameter with a 3mm thickness. A dicing saw with a bevel blade was used to shape the pyramidal tips with a precisely controlled taper slope. Zhang et al. demonstrated an optrode array[57] with dual modality[55], [57]–[59] modified from a previously developed silicon Utah multielectrode array. The reported array had 100 Si shanks, while one was replaced with a multimodal optical fiber. The process of replacement was

performed by removing a shank, using ablative laser machining they drilled a hole and inserted the fiber mechanically through the hole. Packaging was done with adhesive epoxy.

In contrast to the out-of-plane arrays, in-plane micro-waveguide probes[60], [61] benefit more from modern microelectromechanical system (MEMS) technology evolved from process technology in conventional semiconductor device fabrication. These devices have a generic configuration- a silicon or polymer shaft carrying in-plane microwaveguide for optical stimulation and capable of electrophysiological recording and/or microfluidic modalities. There are reports on various dielectric materials as the waveguide components such as oxynitride core (refractive index: 1.51) with oxide clad (refractive index: 1.46)[62], and SU-8 core with either silicon oxide[63], Tungsten-titanium alloy (10% titanium)[65], or glass clad[66]. With microfluidic modality, integrated micro-channels were constructed by either photo-patterning of SU-8 [65] or reflow of borosilicate glass followed by chemical mechanical polishing (CMP) [66].

Although using the fiber optic approach provides higher light intensity, and groups also have demonstrated the proof of optogenetic stimulation using this method[67]–[69]; however using a tethered fiber optic greatly reduces the free moving behavior of the experimental animal[70], [71]. A tethered stimulation system limits the animal to enter small areas or spaces, and hinders the usual interaction of the experimental animal (i.e rodent) with other animals[72]. Experimentation with a coupled optical fiber requires manual attachment/detachment, which requires precision handling by the researchers. Implementing a rigid fiber optic can also create chronic tissue damage or inflammation of the tissue. Using a microscope coupled laser only allows an anaesthetized
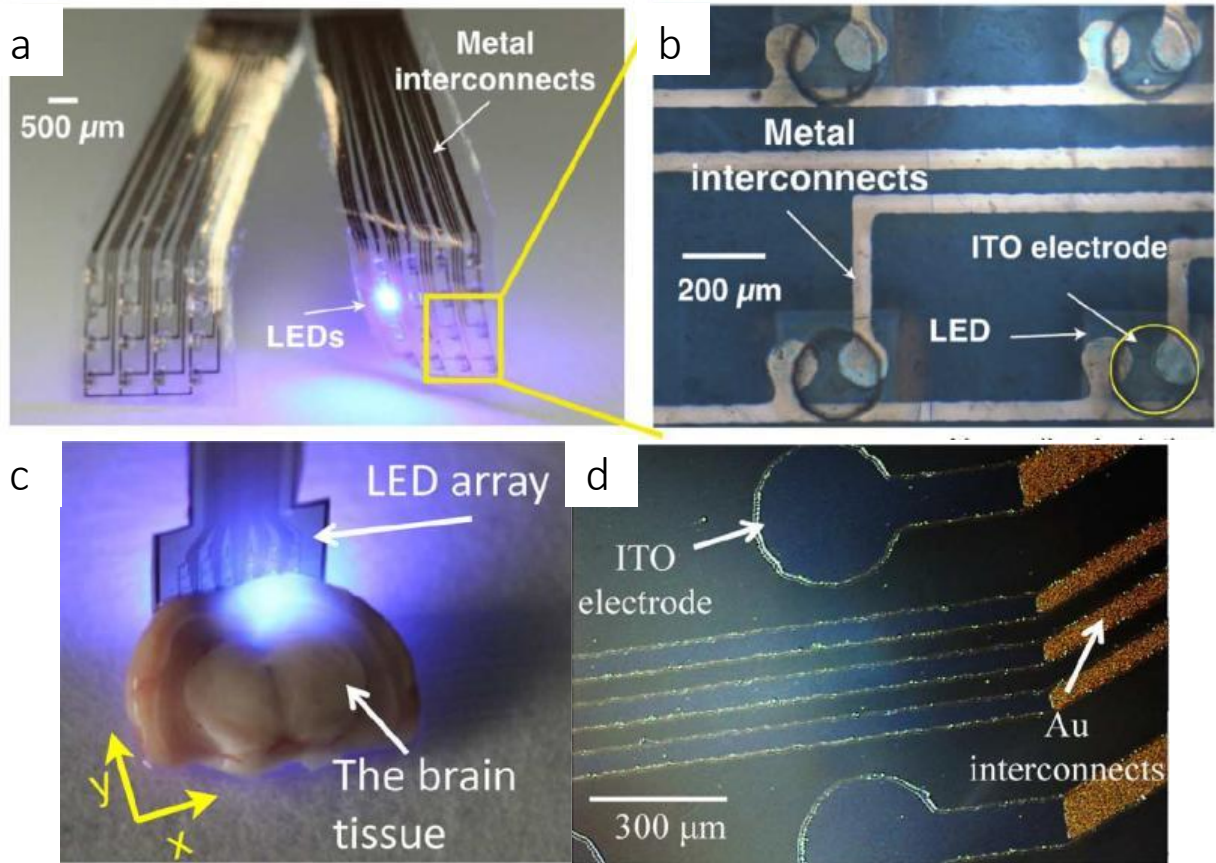
Figure 2-4. a) an assembled opto-μEcoG array b) Zoomed-in image of individual modules c) Light scattering property of the –LED chip was estimated in brain tissue d) ITO electrode array. Adapted from [64].

animal to be used in the experiment as both the light source and the light projection site is fixed[44]. A lower spatial resolution which inherently limits multi-site stimulation accompanies both the fiber coupled or a microscope based optical stimulator.

2.5 Micro-LED based light delivery

LED array based light delivery techniques have recently got much attention[64], [73]–[76]. Use of micro-LEDs (μ-LEDs) gained popularity as they are power-efficient, low-cost, and offers the

14

potential to be integrated with wireless electronics. M-LEDs in an array could be individually addressed [77] through the means of micro fabrication techniques, and thereby enhances the possibility of multi-site in vivo stimulations. These benefits of μ-LED based stimulators have encouraged researchers to investigate flexible, multi-channel stimulators with simultaneous neural data recording capabilities.

The prior work of our group by Kwon *et. al.* in [64] mentions a LED array of 4x4 μ-LED on each of a two subarray design. The active μ-LED array area was 2.5x2.5 mm^2. The stimulator had a two sub array design as the device was intended to simultaneously record EcoG (electro-corticogram) from the bilateral cortical surface. Micro fabrication of μ-LED incorporated neural stimulators on flexible substrates are particularly desirable for both stimulation and EcoG recording as the cortex surface is curved instead of being flat. A flexible substrate capable of bending offers to be in direct contact with the cortical tissue, resulting in valid and efficient EcoG data recording and light delivery. However, the optrode demonstrated by Kwon *et. al.* is a tethered device and has to be wired connected with outside electronics for power and data transmission. None the less, they have the potential to be converted into a truly untethered stimulator with further development. Being a low power system[78], [79], they also have the potential to function with wireless power transmission and wireless telemetry, with further development.

Although LED arrays provide advantages over the fiber optic coupled stimulators in offering the potentials mentioned previously, a challenge still remains for as LED's have low out-coupling efficiency when coupled with a fiber optic and have wide irradiation angles due to the Lambertian

emission pattern [80], resulting in a big loss of radiation. This loss could be compensated by driving the LED's at a higher power to surpass the minimum threshold of effective activation at the target neuron population of the excitatory and inhibitory opsins, 1 mW/mm^2[11] and 7 mW/mm^2 respectively. Application of high LED driving power could potentially damage both the tissue and the neural interface, due to the heat generated by the operating LED's. Higher driving power could increase the temperature of the tissue by >2ºC resulting in neuron damage and degradation; at the same time could potentially damage the solder bonding the LED's, could also burn the packaging material and drain the power source (such as batteries) very quickly. For wireless power transmission and telemetries, transfer of this high power is very difficult to achieve[81] as implants have small coils and cannot be driven by very high frequency and power to maintain tissue and nerve vitality. Also, due to the low power transfer efficiencies for wireless wireless power, only a limited power is possible to transfer to the receiver coil. Therefore, a method offering enhanced intensity along with reduced power consumption is desirable for efficient optical stimulation and to establish a complete untethered system.

The following table lists the difference in the optical interfaces discussed in this section, along with their advantages and disadvantages.

Table 2-1. Comparison among optical interfaces

Interface	Advantages	Disadvantages	Other remarks
Laser coupled fiber optics	High intensity, focused beam	High power required, low spatial resolution, localized heat generation, tethered system, wireless stimulation not possible	Conversion to untethered system not possible
LED/laser diode Coupled fiber optics	Collimated beam. Lower power required than laser coupled interfaces. Fast Switching.	Tethered system, low spatial resolution, localized heat generation, wireless stimulation and telemetry difficult for laser diode.	Conversion to untethered system might be possible
Microscope coupled optics	Focused beam, high intensity	Tethered system, anaesthetized animal required. localized heat generation, low spatial resolution, wireless stimulation or telemetry not possible.	Conversion to untethered system not possible
μ-LED based flexible neuro-stimulator	Flexible, high spatial resolution, multi-site stimulation, low power device, Fast Switching.	light not collimated, low intensity compared with fiber optics interfaces	Untethered development, wireless control and telemetry possible

Chapter 3. A Review of Light Delivery Methods: Untethered Stimulators

An ideal optogenetic stimulator, in general would be capable of effectively and practically deliver sufficient light (of high power density)[1], [12] to the target neural population in order to create behavioral changes on the experimental animals[82], [83]. Early development of optical stimulation tools requires penetrating optical fibers with interconnections to externally located electronic control and light sources (i.e. lasers) [1]. Recent demonstration of surface mounted optical sources and electronics (i.e. LED and Bluetooth data transmission systems) also exposes necessity of being connected with batteries or outside power sources[84]. These tethered systems require manual and physical attachment/detachment of an optical fiber or batteries[85], [86] before behavioral testing, thereby limiting the environments in which freely behaving optogenetic experiments and data collection could be performed. To address this issue, some groups have implemented fiber rotation techniques during animal movements[10], [22]. Although this approach has improved the ease of device attachment and detachment, the tethering could increase chronic physical trauma at the implanted site as well as bias the results of behavioral studies[87] as the animal is not familiar with this pain and hence it is uncomfortable during the experiment. Furthermore, surface mounted stimulation sources and data acquisition systems suffer from deficiency in penetrating into the volumetric depths of the tissues, which poses a significant challenge in their operations [88]–[90].

The optical stimulators mentioned in the previous section were examples of untethered systems, as one end of the devices are connected with outside power sources or telemetry links. As mentioned before, although the tethered stimulators provide more than sufficient output

intensity for effective opsin expression, however they restrict the free moving behavior and natural/social interaction of the animal. LED array stimulators are more preferable than the microscope or fiber optic coupled ones in regards of multi-site, high spatial resolution[91], [92] stimulation and because of their potential to be converted into wirelessly power transferred stimulators and connected to wireless telemetry electronics. To eliminate the deficiencies of wire tethering, several wireless powered optical stimulation sources have been demonstrated in previous reports[48], [68], [72], operating at high frequencies (910 MHz or 1.5 GHz) to achieve the desired untethered power transfer.

3.1 Battery powered head mounted systems

To eliminate the tethers, recent efforts have been made to provide optical stimulation via wireless head-mounted systems [48], [68], [71], [81], [93]–[95]. Development of both wirelessly powered [71], [81] and battery powered [48], [84], [95] devices have been pursued to deliver light to the surface of the animal brain with an LED. In order to stimulate the deeper brain regions, targeting with a flexible, injectable LED system with the option to be powered wirelessly through a head-mounted receiver [68], [93] or with a battery powered module assembled from commercial off-the-shelf components [84], [94] have been explored. However, one of the limitations of these devices are in the mass and size. Head mountable devices in general, have a mass larger than the
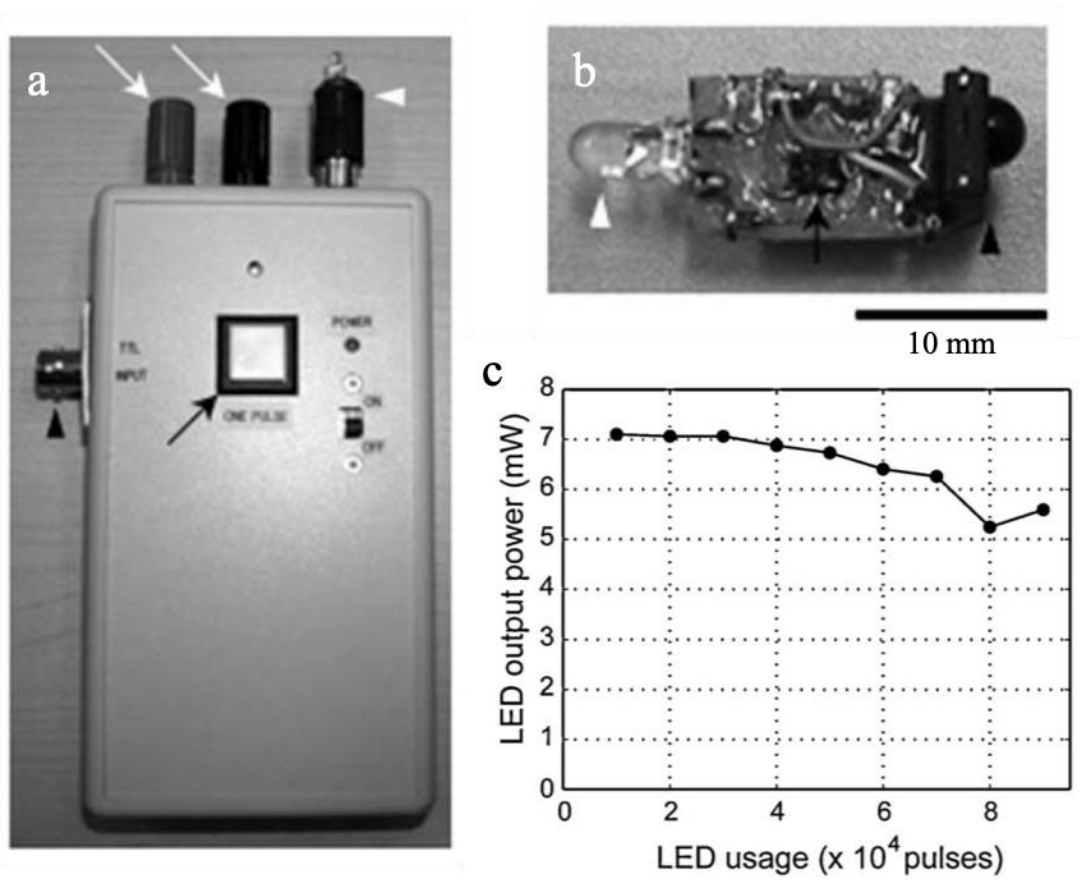
Figure 3-1. a) Image of the transmitter b) Image of the receiver c) averaged output powers of the LED after every10,000 pulses of 25ms duration. Adapted from [48].
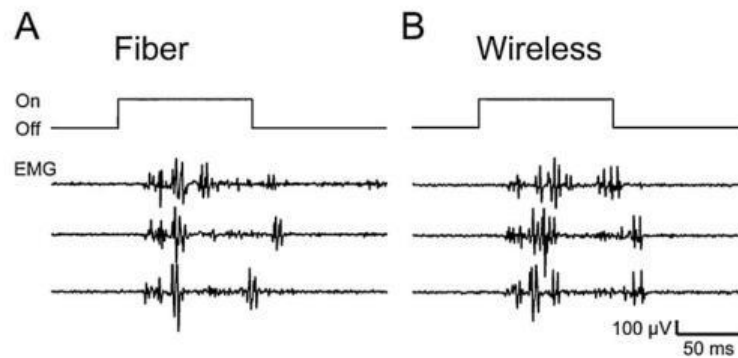
Figure 3-2. EMGs from the right hind-limb with light stimulations delivered by an optic fiber on the left motor cortex. (B) EMGs from the right hind-limb with light stimulations delivered by the wireless LED receiver unit. Adapted from [48].

animal (mouse) head itself and usually protrudes millimeters beyond the skin. Generally, these head mountable devices are connected with a connector and requires attachment and detachment before and after the experiments, and cannot be left attached to the animal for prolonged periods of time. This limitation is more prominent when stimulating the spinal cord or the peripheral nervous system, as the size and mass prohibit and limit the central structures that can be targeted [96]. Moreover, bearing a load on the head prevents the animal from entering very small enclosures. A small power receiver turning on an LED was reported by Yeh et al, however stimulation of opsin expressing cells or any target neuron population was not performed [97].

The approach of Iwai *et. al.* provides a head mounted battery powered stimulation system[48] consisting of a transmitter and a receiver, illustrated in Figure 3-1 (a-b). The transmitter in Figure 3-1 (a) was an infrared (IR) remote to control the receiver, sending output signals at 38KHz. The receiver in Figure 3-1 (b) consisted of a 3mm diameter blue LED (NSPB300B, Nichia), and was powered through 2 Li batteries (CR1025). The total mass of the receiver, as reported by the researchers was 3.1g while the batteries were 1.4g approximately in total. However, the system lacks the capability of data recording. Iwai *et. al.* reported a 65% (74 out of 114 trials) success rate in stimulation for a 100 ms pulse width, success rate was defined by whole body muscle twitch detection after stimulation. For the same experiments, 28 trials also detected whisker movement. Figure 3-1(c) indicates that the LED provided a constant output power for a 40K pulses, and then starts to reduce.

Figure 3-2 shows the stimulation efficacy of the wireless device demonstrated by Iwai *et. al.* in contrast with a fiber optic stimulation. For stimulations with identical parameters, they achieved similar EMG responses for both the fiber coupled stimulator and their wireless stimulator, for multiple trials.
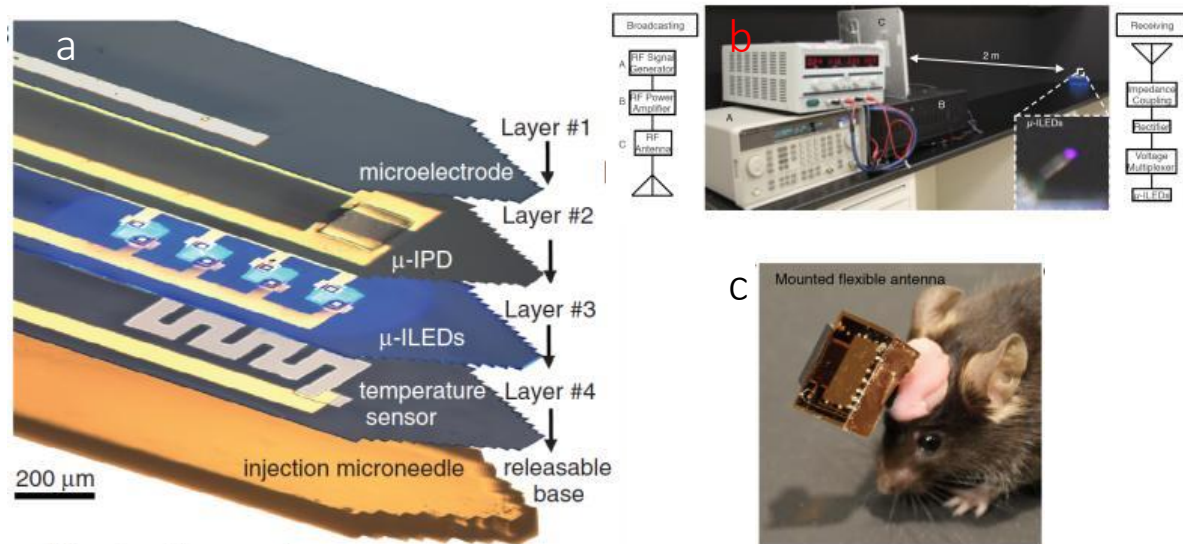
Figure 3-3. a) A multifunctional, implantable optoelectronic device, illustrating various components. b) Photo and diagram explaining the components of the system and demonstrating wireless power c) Mice with acutely mounted head-stage antennas. Adapted from [68]

Ideally, a fully wireless system that enables chronic experiments, and supports experimentation with multiple animals is desired. Although promising, however battery-based systems suffer from operational charge limitation[48], [98], especially when the LED's are driven by high current for targeting deep brain structures; battery powered modules are particularly disadvantageous when many LED's are required. The weight of the batteries comprises most of the head mounted modules weight- as an example the batteries for Iwai *et. al.* receiver makes up 50% of the total weight.
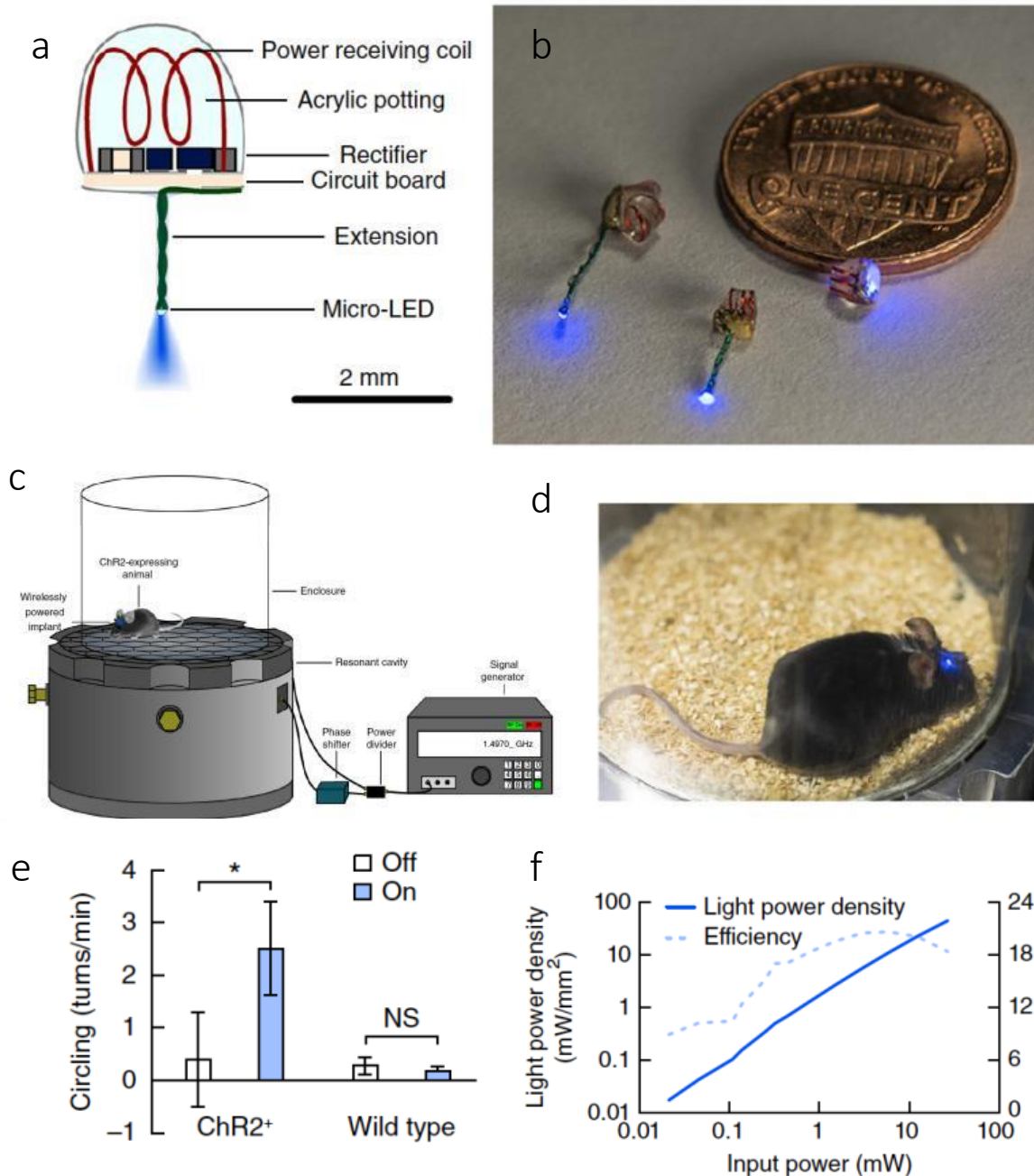
Figure 3-4. a) Schematic of wireless implant customized for the brain. b) Size comparison of wireless implants (left to right: peripheral nerve endings, brain, spinal cord) with a US 1-cent coin. c) Diagram of light-delivery system. d) Freely moving mouse with the brain implant e) Mean circling rate of ChR2+ mice significantly increased (0.40 turns/min to 2.5 turns/min; n = 5 ChR2+ mice, paired t-test, *P = 0.021 f) Light power density and efficiency of the LED as a function of input power. Adapted from [72]

3.2 Far field wireless stimulation systems

The approach followed by Kim *et. al.* introduces a novel injectable cellular scale optoelectronic based stimulator[68]. Apart from 4 custom fabricated micro LED, this injectable and releasable neuro stimulator also consists a platinum electrode for electrophysiological recordings or electrical stimulation, light detector and a temperature sensor, depicted in figure 3-3 (a).

For wireless operation, as shown in figure 3-3 (b,c) the system relies on a head mountable printed circuit board (PCB) consisting of an antenna to receive power at 910 MHz from a signal generator. Montgomery *et. al.* reported a wirelessly powered fully internal device for optogenetic stimulation of brain, spinal cord or peripheral nerve endings[72]. The stimulator consisted of a LED, a power receiving coil and necessary circuitry- accumulating a total size of 10-25 mm^3 and of 20-50 mg in weight. The receiver unit is powered through a 21-cm diameter, 15-cm height aluminum resonant cavity to couple electromagnetic energy towards the tissue at 1.5 GHz. This group from Stanford adjusted the light power density by varying the input power to the resonant cavity. With a maximum power output efficiency of 19% (emitted light power/input power) throughout the power densities suitable for optogenetic stimulation (1–20 mW/mm^2), their stimulator generated behavioral change (circling of the animal during stimulation).

3.3 Near field wireless stimulation systems

Mickle et. al. introduced a miniaturized bio-optoelectronic implant [99] providing an optical stimulation interface using microscale inorganic light-emitting diodes to activate the opsins, eventually stimulating the transgenic neurons the opsins are bound with. They implemented a

soft, high-precision biophysical sensor system allowing continuous organ function measurements, simultaneously providing a control module and data analytics approach. Significance of this approach, as explained by Mickle et. al. was to support closed-loop operation of the system in order to eliminate the occurrence of pathological artifacts in real time. Their interesting prototype included a soft strain gauge that transmitted real-time bladder function information, experimented in a rat model. In addition to the prototype demonstration, they have utilized data algorithms and identified pathological behaviors, and have automated the optogenetic closed-loop neuromodulation of bladder sensory afferents to show the normalization of bladder function. The wireless control and power (WCP) module as they have described, is a thin flexible component subcutaneously inserted in the rat abdomen. Similarly interesting as their approach towards pathological artifact reduction is their use of wireless power transfer to the implant. Utilizing the principal of a three coil resonant inductive coupling, Mickle et. al. loaded the transmitter side with a 13.56-MHz radio frequency identification driver, impedance-matching circuitry along with a primary coil. The resonator coil wrapped around the bottom of the cage to enhance the efficiency of power transfer, and a load/receiver coil in the WCP module constitute the receiver end. Taking the advantage of impedance matching of the receiver coils to resonate at 13.56 MHz establishes a loosely coupled wireless power transfer system. This specific design assisted to reduce sensitivity mismatches in the antenna characteristics to ensure wireless power transfer property with a coverage of the rat cage. Although their system introduces an unique design and efficient method for delivering wireless power, the size of their prototype and receiver coil (~10mm in diameter) is still a limiting factor while establishing a miniaturized wirelessly powered implant.

These reported untethered approaches have shown the efficacy of battery powered head mounted module with IR signaling, injectable μ-LED's capable of receiving wireless power through rigid PCB and flexible polyimide substrate with antenna, and miniaturized receiver unit receiving power from a resonant cavity. However, the limitation still exists in the size of the receiver unit, the difficulties in attachment and detachment of the receiving antenna with the stimulator, and more importantly, the frequency (1.5 GHz or 910 MHz) at which the transmitter is transferring the wireless power. The high operating frequency range of the reported systems mentioned in this section is proved to be unsafe towards nerve vitality[100], simultaneously induces possibilities regarding electromagnetic radiation over-exposure and microwave-induced heating of nerve tissues[101].

To meet these challenges, a truly untethered system is desired which is capable of wirelessly transmit power to the stimulators at a low frequency that does not damage the nerve and their vitality, at the same time is small enough to be fully implanted and provide deep brain stimulations while increasing minimal heat during operation and provide efficient optogenetic opsin expression for the target neuron population.

In this thesis, the author has proposed a wirelessly powered, miniaturized, reflector coupled multichannel optical stimulator that operates at low frequencies and is capable of efficient opsin express, both for *in vivo* and *in vitro* experiments. In order to realize that, the author has integrated an aluminum coated hemispherical reflector-fabricated using silicon isotropic etching to enhance the optical intensity from each channel. A reflector coupled stimulator was demonstrated to prove

the viability of an intensity enhanced multichannel stimulator- where each channel could be individually addressed and the device as a whole is capable of multisite stimulation. To realize the untethered property, the author has demonstrated a battery powered head mounted module as a first generation interface. This module uses Bluetooth low energy (BLE) for data transmission and has simultaneous stimulation and recording capability, as well as providing real time data update using a computer GUI and storing the data in a PC for further analysis. In vivo animal experiment was successfully performed using this first generation untethered device on an experimental animal. In order to realize a truly untethered interface using wireless power transfer, the author has demonstrated proof of concept of a single channel stimulator coupled with a two coil link to wirelessly power the optical source. The expectation for this interface was to successfully transfer energy wirelessly to operate a single channel stimulator using low frequency (<100MHz). A successful demonstration of the working stimulator has been provided in this thesis, and in vivo experiment on an anaesthetized rat proved the efficacy of the stimulation on the living tissue.

The work done by the author expects a significant optical intensity increase due to the collected backside emission from the coupled reflector. The miniaturized single channel stimulator is expected to be wirelessly powered and effectively stimulate neurons for in vivo experiments. In order to be a fully implantable biomedical device, the implants are expected to be miniaturized, and dissipate low heat-subsequently generating low temperature increase (<2ºC). Multisite stimulation is required to increase the spatial resolution of the proposed devices by using higher channel counts. Meeting these requirements are imperative in order to achieve the ultimate goal

of the project- an intensity enhanced, truly untethered (wirelessly powered) miniaturized, multichannel optical stimulator for both in vivo (on behavioral experimental subjects) and in vitro studies as a biomedical implant.

The following chapter provides a detailed description on the fabrication and characterization of a development process on micro scale LED arrays to be used in optogenetic applications. Typically, inductively coupled plasma reactive ion etching (ICP-RIE), an expensive and complicated etching process is used to fabricate LEDs commercially. The author has implemented low cost conventional RIE technique using SF_6 gas plasma. Blue LEDs having a peak emission wavelength of ~470nm were fabricated monolithically, then characterized and compared with the commercially available one. The process developments sets the footprint for microscale LED fabrication towards the light delivery tools needed for optogenetic stimulation.

Chapter 4. Gallium Nitride Micro LED: the optical stimulus source

Light emitting diodes (LEDs) are the semiconductor devices that can efficiently convert electrical energy into electromagnetic radiation[102]. Most of this radiation falls within the visible light spectrum for humans. The semiconductor germanium was the first material to be used to fabricate LEDs. However, germanium was quickly replaced by silicon due to its superior power handling performance, electrical properties, and temperature stability[103]. Efficient luminescence requires the photon energy comparable with the energy band gap of the semiconductor and semiconductors with energy gaps >2 eV is desirable[102]. This property is available in the III-V compound semiconductors. The III-V nitride materials have shown a great potential in the fabrication of optoelectronic devices due to their wide band gaps and reasonable electron mobility[103].

4.1 Use of Gallium Nitride (GaN) as a wide bandgap LED material

One of the prominent III-V compound semiconductors is gallium nitride (GaN). To date, GaN and its alloy nitrides, such as InGaN and AlGaN, have been widely utilized in the manufacturing of optoelectronics, such as light emitting diodes, lasers, detectors and high-temperature devices. The band gap for GaN is 3.2 eV and electron affinity is 4.1 eV, thus making GaN-based optoelectronics operate in the blue/green and UV region of the light spectrum with a wide variety of applications [104]–[106]. Of particular interest is the application of blue/green LEDs in optogenetics, which has attracted a great attention of the neuroscience community[107]–[109]. Various LED neural interface devices have been developed using wide bandgap materials, for site-specific and multi

photon-stimulation of opsin expressing neurons[64], [76], [110]. With the rapid growth of this field, there has been an increased need for the development of high-resolution, high-channel-count LED light sources to fully realize the potential of optogenetics. This requires a reliable, low-cost technique for patterning GaN and its alloys in order to increase the control precision and minimize the damage to devices.

4.2 Review on GaN Etch methods

Chemically, GaN is known to be a very stable material with high bond strength, which makes it insoluble in common mineral acids and bases at room temperature. Carosella et al. reported that AZ400K (active ingredient KOH) etched molecular beam epitaxially (MBE) grown GaN at 80 °C but did not etch GaN synthesized by metal organic chemical vapor deposition (MOCVD) or hydride vapor phase epitaxy (HVPE) methods[111]. GaN can also be etched in hot phosphoric acid and alkali solution at a very slow rate. However, in order to achieve high yield and fine pattern transfer, slow etching in acids and base is not a very practical option.

As an alternative, plasma etching techniques have been explored for efficient dry etching of GaN with fast etching rates. Commonly used dry etching techniques include the electron cyclotron resonance reactive-ion etching (ECR-RIE) and inductively coupled plasma RIE (ICP-RIE) that utilize high-density plasma under a lower operating pressure of 0.133-0.266 Pa and lower ion energy[112]. For example, Pearton et al. reported the dry etching of GaN by ECR-RIE, using different gasses of CCl_2F_2, CH_4, Cl_2, and BCl_3 activated by an ECR plasma source biased with a

13.56 MHz RF power[113]. Humphreys and Govett reported the etching rate of greater than 100 nm/min using Cl2/ CH4 gas mixture plasma generated by ECR-RIE[114]. Other specialized plasma etching techniques have been reported, such as reactive ion beam etching (RIBE) and chemically assisted ion beam etching (CAIBE) with Cl2 and BCl3 as reactive gasses[115]. Although ECR-RIE, ICP-RIE, and IBE have a unique ability to control the ion flux and ion energy separately, these techniques usually involve corrosive chlorine, chlorine mixtures and chlorine-based halocarbons based plasmas[116], [117] that damages the vacuum system and requires expensive reactive chamber and specific filtration system[118] in contrast with less corrosive SF6, CH4, Ar and H2 based plasmas[117]. In addition, hydrogen diffusion in GaN during ECR-RIE can create electrically neutral complexes with dopants[119]. The incorporation of hydrogen leads to uncontrolled variations in conductivity of a semiconductor. Moreover, due to the wide band gap and high bond strength of group-III nitride materials, the dry etching techniques generally rely on high-density ion bombardment to assist the chemical etching and to promote both bond breaking and sputter desorption of III and N–reaction products[115]. This may, in turn, degrade the structural quality of the material, leading to optical and carrier losses.

Conventional RIE techniques, on the other hand, are seldom used in GaN etching. Several researchers explored GaN etching using Cl or F based gasses, such as CHF3/Ar, C2ClF5/Ar, SiCl4, CCl2F2/Ar, and Cl2/H2[103], [113], [120]–[122]. Hydrogen containing gasses like CH4 and HBr have also been used for RIE patterning of GaN[123], [124], by breaking the stable bonds of GaN using high energy ions. However, these approaches still suffer from the diffusion of hydrogen in the hydrogen gas plasmas, the requirement for expensive reaction chamber, and the special gas

residue disposal system[118]. While Basak et al. reported the reactive ion etching (RIE) of GaN using SF6 with the etching rate of 5.4-15.4 nm/min in[125], no LED devices were implemented using such a process to demonstrate its viability.

In this work, we report a low-cost, hydrogen-free fabrication method for making GaN blue LED arrays using SF_6 plasma etching alone in a conventional RIE system. We have focused our efforts on studying the etching rate and surface roughness of MOCVD grown epitaxial GaN on a sapphire wafer with different carrier materials and with different etching recipes. GaN LED arrays were successfully implemented using the developed process, and their optical, electrical, and thermal properties were fully characterized. Improvement in the electrical and optical characteristics by annealing the LEDs in a nitrogen environment was also studied. Compared to the techniques reported by other researchers, our RIE etching method is less expensive and corrosive, and enables reasonably fast etching rate of GaN.

4.3 GaN LED fabrication by reactive ion etching

Figure 4-1 illustrates the process flow for making GaN LEDs using SF6 plasma etching[126]. MOCVD grown GaN epitaxial LED on sapphire wafers (2 inches in diameter) were obtained from Xiamen Powerway Advanced material Co, China and diced into 1 cm × 1 cm chips. Each LED was 400 µm × 150 µm in dimension. Cu was selected as the mask material for GaN etching because the low etch rate of Cu in SF6 plasma[127]. For the mask, 500 nm copper with a 5 nm titanium adhesion layer was deposited by thermal evaporation Edward Auto306, Edwards). A positive photoresist mask

(Shipley S1813, MICROCHEM) was patterned using ultraviolet (UV) lithography. The unwanted Cu

and Ti was removed chemically using copper etchant (Ferric chloride, MG chemicals) and buffered

hydrofluoric acid (MicroChem) respectively. Prior to RIE processing, the chips were attached to

different substrates, in order to study the effect of substrates on the etching rate. RIE was carried

out in a Nordson March RIE-1701 plasma etching system using SF6 with the gas flow of 40 sccm

and the base pressure of 15 mTorr. The RF power was varied during plasma etching. Table 4-1 lists

the processing parameters under different conditions.

Table 4-1. Processing parameters of GaN samples

Recipe #	Processing pressure (mTorr)	RF power (W)	Carrier substrate
1.	200±50	200	Sapphire
2.	200±50	200	Silicon
3.	200±50	200	Glass
4.	200±50	400	Glass
5.	200±50	600	Glass

To fabricate the LED structure, 30 nm SiO2 was deposited at 300 °C using plasma enhanced

chemical vapor deposition (PECVD) machine (Plasmalab 80 Plus, Oxford) to create an insulation

between n-GaN and p-GaN layer contact metals. The oxide layer was later patterned using S1813

photoresist to create an active current injection site of 20 μm diameter at the RIE etched n-GaN

surface. After that, metallic materials (Ti/Al/Ni/Au) were deposited using thermal evaporation (for

Ti, Al, Au) and e-beam evaporation (for Ni), and patterned using lift-off with a photoresist mask to form the contact pads. The contacts were made by Ti/Al/Ni/Au (50/400/50/150 nm) for the n-GaN and Ni/Au (50/150nm) for the p-GaN, respectively. Multilayer metal contacts were carefully designed to reduce the contact resistance at the metal-GaN interface. For the n-GaN, in particular, Ti was chosen as the direct contact on n-GaN because its work function (4.3 eV) is closer to n-GaN (4.1 eV), resulting in a small potential barrier[128]. Ti reacts with the nitrides to form TiN or AlTi2N layers by annealing, which reduces the native gallium oxide at the AlGaN/GaN interface[129] to further improve the contact resistance[130]. Au in the outer layer prevents oxidation of the Ti/Al metals during annealing. A diffusion barrier layer (Ni) is applied to minimize the diffusion of Au[129]. For p-GaN, Ni was chosen because of its very high work function (5.15 eV), allowing efficient charge carrier transport[131]. To ensure a good adhesion of metal on the GaN surface, an oxygen plasma etching was used before metal deposition to remove photoresist residues. The layer structure of the LED is shown in Figure 4-1. Post-fabrication, the LED samples were annealed in a nitrogen atmosphere at temperatures of 150 °C, 300 °C, and 450 °C for 10 mins each.
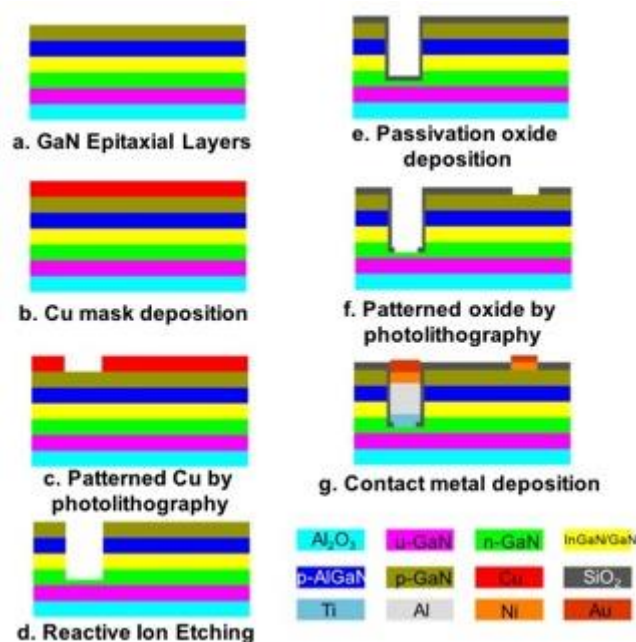
Figure 4-1. Simplified fabrication process flow for making GaN LEDs.

4.4 Device characterization

The etched step-heights were measured by an atomic force microscope (Dimension 3100 SPM, Veeco Bruker) to quantify the etching rate of GaN. The surface roughness of the etched n-GaN surface was also analyzed by AFM, since spatial disorders and rough etched surface may result in unwanted light scattering[115]. The electrical properties of the fabricated LEDs were characterized using a semiconductor parameter analyzer (4145B, Hewlett Packard). The light intensity of the LED was measured using an optical detector (818-SL, Newport) and quantified using an optical power meter (815 series, Newport). The temperature variation of the LED before and after being turned on was measured using a thermal imaging camera (FLIR E6, FLIR) in air at the ambient temperature of 22 °C.

4.5 Surface morphology results

The step heights of the etched GaN were measured along the diagonals of the 1 cm×1 cm chips etched using the recipes in Table 4-1. Figure 4-2 (a) shows the average etch rates and standard deviations (n=50, number of LED's for each recipe), calculated from the step heights. We tested the etching rates of GaN with three different substrates: sapphire (recipe 1), silicon (recipe 2), and glass carrier substrates (recipe 3-5). Etching recipe 2 and 3 shows a smaller standard deviation than recipe 1, suggesting that the addition of a carrier substrate improves the uniformity of GaN etching under the same processing pressure and power of RIE. In addition, adding the glass
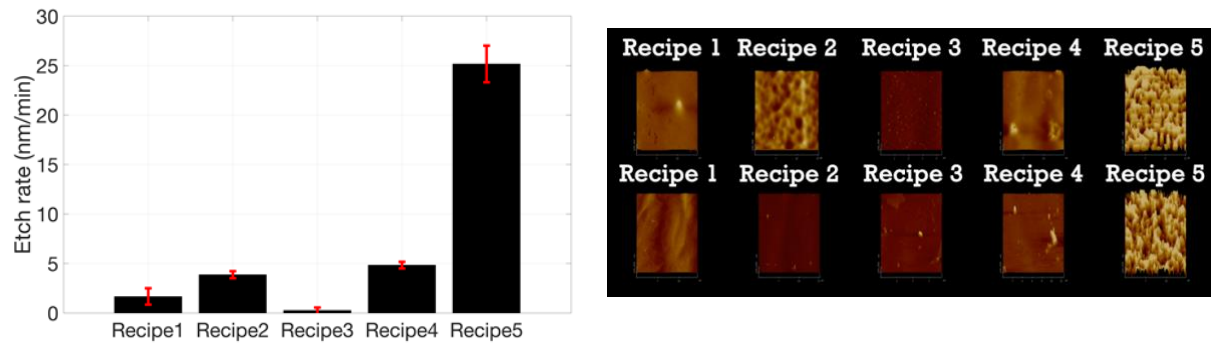
Figure 4-2. (a) Mean etch rates for the recipes listed in table 1. (b) AFM images of etched n-GaN (top row) and p-GaN (bottom row) (number of samples, n=22).

substrate reduces GaN etching rate while the additional silicon substrate enables higher etching rate compared to samples with sapphire substrates. This difference in etching rates could be due to the different thermal conductivity of glass (0.8-0.9 W/mK), sapphire (27.21 W/mK) and silicon (149 W/mK) at 300 K. The higher thermal conductivity of silicon and sapphire than glass might have assisted to disperse the heat generated during the reactive ion etching step which in turn, might have increased the etch rate[132].

The effect of RF power on etching rate was tested with the various power of 200, 400, and 600W, using samples with additional glass substrates. As expected, increasing RF power enhances the etching rate significantly, as shown in Figure 4-2 (a). However, 600W RF power created fractures on GaN layers due to high-energy ion bombardment that results in pinholes and deformation in the metal mask.

Three-dimensional (3D) surface roughness images of the etched and mask covered surfaces are provided in Figure 4-2 (b). Surface roughness images also illustrate the deformation of the masked surface due to rapid plasma removal, which is prominently significant when higher RF power is used. This phenomenon could be eliminated by using other mask materials like aluminum[127]. Figures 4-3 (a) and (b) show the average surface roughness of the RIE etched surface and the mask-covered surface, respectively. For the same RF power, it was found that adding a silicon carrier generates more roughness, resulted from the higher etch rates. Also, the surface became rougher as the power increased, indicating the surface roughness to be correlated with higher energy plasma[133].
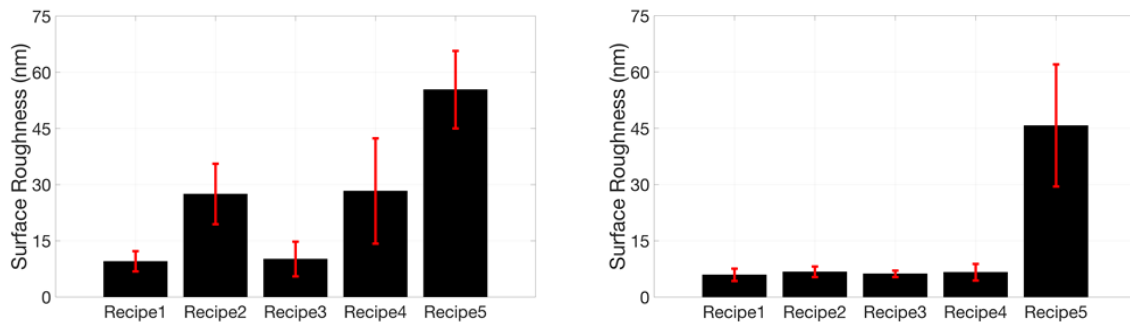
Figure 4-3. Mean surface roughness for the recipes listed in table 1. (a) on the n-GaN layer (b) on the masked p-GaN layer. (number of samples, n=22).

4.6 Electrical properties

Figure 4-4(d) illustrates current (I) vs. voltage (V) characteristics of LEDs for annealing temperatures of 150, 300, and 450 °C compared with the IV characteristics of a commercially available LED. LEDs fabricated using recipe 2 were chosen due to the comparatively high etching rate. Moreover, recipe 2 has a higher surface roughness on the n-GaN surface, providing better contact metal adhesion and simultaneously reducing contact impedance. The comparison indicates higher impedance for the as-fabricated LED's which could result from the oxide layer formed on the metal contacts. The post-fabrication annealing treatment improves ohmic contact between metal and GaN, presumably by creating better metal alloy contact at the metal interface. Annealing at higher than 300 °C effectively reduced the contact impedance, hence increasing the current output at a given voltage. The IV performance, however, still needs to be improved. Figure 4-4 (e) shows the threshold voltage of the LEDs, which is defined as the voltage when the LED starts to conduct current (in our case 0.1 mA). The threshold voltage was decreased from ~3.9V to ~2.8V, corresponding to annealing temperatures of 450°C and making the forward voltage of the as-fabricated LED's comparable to commercial ones[134].
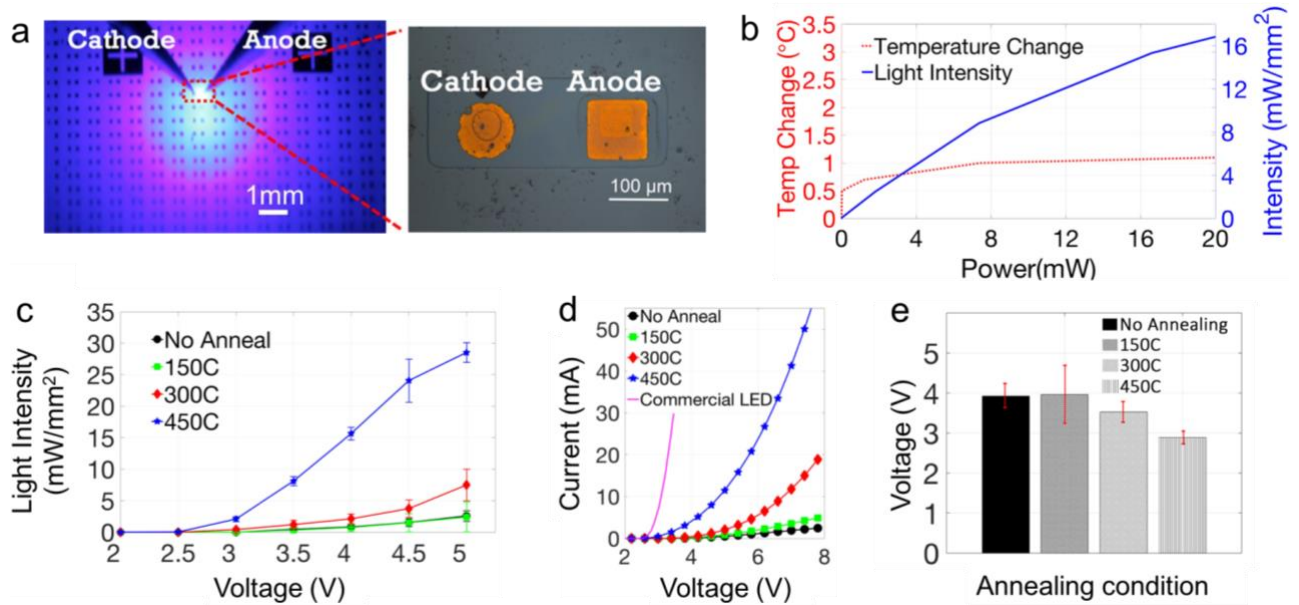
Figure 4-4. A fabricated LED array and a microscope image of a single LED (b) change of the LED surface operating temperature with input power and optical intensity (c) Change of light intensity in as-fabricated LED's (n=4). (d) I-V characteristics of as-fabricated LED's under different annealing temperatures compared with a commercial LED's characteristics (e) The threshold voltage of the LEDs under different conditions. Figures represent results from LEDs fabricated using recipe 2.

4.7 Optical and thermal properties of LEDs

Similar to the electrical properties, the optical performance of the arrays was also improved after annealing, as shown in Figure 4-4 (c, d). The LED's provided a light intensity of 15 mW/mm^2 when ~4V were supplied, after annealing at 450 °C. Shown in figure 4-4 (b), the temperature change was found to be less than 1 °C when 20 mW electrical power was applied to drive the LED, which at the same time provided ~16 mW/mm^2 light intensity. These properties of the fabricated LED's makes it suitable for complete device fabrication, especially towards biomedical implantations[135].

Table 4-2. Comparison of GaN etching with RIE and methods reported by other groups.

Work	Etching method	Etching rate (nm/min)	Etching gas	Intensity (mW/mm2)
[125]	RIE (120-250W)	5.4-15.4	SF6	N/A
[136]	ICP-RIE (250W RF, 1000W ICP power)	360	Cl2/CH4 /H2/Ar	N/A
[137]	ICP-RIE (250 W RF power)	N/A	Cl2/Ar	15
[138]	ICP-RIE (100W RF, 800W ICP power)	300	Cl2/Ar	N/A
[139]	ECR-RIE (200W RF,100W ECR)	13	BCl2/Cl2	N/A
this work	RIE (200-600W)	2-25	SF6	16

Table 4-2 lists the etching method and used gases, etch rate and optical intensity of our RIE method compared with other LED fabrication approaches reported in the literature.

This method provides a number of advantages. First, the use of conventional RIE and less corrosive fluorine gas not only reduces the production cost but also lowers the risk of corrosion in the RIE chamber and corrosive gas hazards[116]–[118]. Second, the etching rate for our LED arrays with substrates varies from 2-25 nm/min, which is significantly higher than the RIE etching methods reported by other groups[125], [133], [139]. Third, our fabrication method is compatible with conventional microfabrication techniques, facilitating the integration of the LED arrays with other electronic elements to achieve complex, system-level functionality. However, it should be noted that the electrical efficiency of our LED's is lower than that of a commercial GaN LED in figure 4-4

(d). The optical output intensity at an applied power in figure 4-4 (c) indicates the necessity in improving the power conversion efficiency. This performance reduction is mainly attributed to oxide layers formed in between metal contacts, thereby increasing the contact impedance, which could be addressed by maintaining a better vacuum during metal deposition and creating a better contact metal alloy.

In this chapter, the author has systematically characterized a low-cost and less-corrosive method for GaN LED fabrication based on SF_6 plasma etching in a conventional RIE system, and successfully applied this method for making high-density LED arrays. The results demonstrate that improved etching uniformity and surface roughness could be achieved by adding carrier substrates during plasma etching. High-temperature annealing effectively reduces the contact impedance between metal and GaN, resulting in lower threshold voltage and higher light intensity of the LEDs. The low-temperature change together with sufficient light intensity at low supplied power expands the horizon of the microfabricated LEDs for different biomedical applications, especially aiming towards optogenetics implants.

The following chapter discusses the concept of a first generation prototype, including the description of a tethered, hemispherical reflector coupled multichannel (32 channels) stimulator array capable of multi-site stimulation with an enhanced optical power density (maximum of 65% enhancement from a bare LED).

Chapter 5. Optical Intensity Enhancement and Beam Collimation

In this chapter the author attempted to address the issue of compensating the backside emission loss and enhance output light intensity with a low power consumption- by using a promising approach of incorporating an optical element with the LEDs. The LED array stimulators currently in use is able to collect one-sided radiation of the optical source[81], while the backside radiation is not contributing towards the activation of opsin transfected neurons. This chapter proposes the micro fabrication of a cavity reflector coupled with the LED arrays in order to enhance output light intensity by capturing the backside reflection of the LEDs. The objective of this prototype device is to establish our capability of fabricating multichannel stimulators, while enhancing the intensity for opsin activation at a lower power, thereby enabling wireless power transfer and telemetries for stimulation and data recording.

5.1 Method

As shown in figure 5-1, the proposed reflector coupled LED array design consists of 32 stimulation channels, being distributed in a 4x4 configuration on two subarray panels of 3mm x 3mm each. Each channel contains a μ -LED with a surface area of 220 μm x 270 μm x 50 μm aligned on a reflective silicon cavity with a diameter of 300 μm[140]. The overall device dimensions are 23 mm x 10.5 mm. The two-panel design allows the stimulator to be used in in-vivo animal experiments, where we can selectively stimulate each of the cortices of the brain.

Expanding over the cortices, this device design is capable of stimulating our entire region of interest (the visual cortex) in multiple sites by individually controllable stimulators. Release from

the silicon wafer makes the device fully flexible and implantable on an experimental subject.

Table 5-1. Design properties of reflector coupled two panel stimulator

Property	Dimensions
Panels	2
Each panel length x width	3x3 mm
No. of stimulation site on each panel	16
Distance between stimulators	800 um x 600 um
LED dimensions	270 um x 220 um x 50 um
Distance between panels	3 mm

5.2 Device design

As illustrated in figure 5-1 , the proposed stimulator consists of an array of 32 stimulation channels distributed in two symmetric panels, with 4x4 channels on each panel[140]. Each of these stimulation channels has a μ-LED coupled with a reflective silicon cavity. The μ-LED (CREE TR2227tm) has a surface area of 270 μm x 220 μm and a thickness of 50 μm, and the central illumination wavelength of 465 nm for excitation of optogenetic opsins. The diameter of each hemi-spherical reflective cavity is 300 μm and the distance between adjacent cavities is approximately 430 μm. The overall dimension of each panel is 3 mm x 3 mm, which is intended to cover one hemisphere of the primary visual cortex (V1) of rats. The two-panel design exclusively allows stimulation of both cortices individually. To reduce the number of interconnects to control circuitry, LEDs on each panel share a single ground wire while having separate power wires to

enable individual control of one or more LEDs at a time.
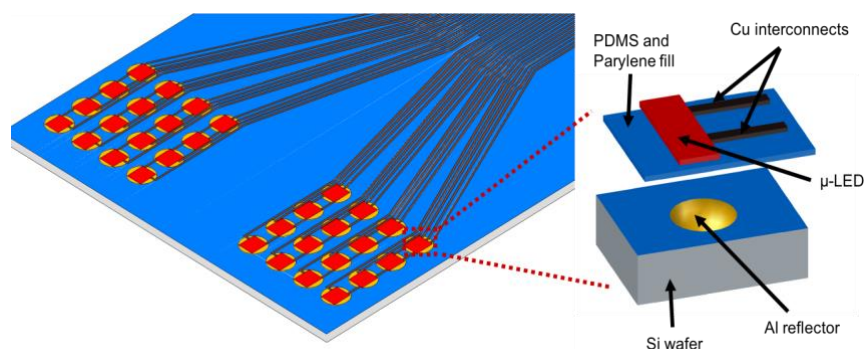
Figure 5-1. Conceptual schematic of the reflector coupled μ-LED array stimulator.

Figure 5-2 illustrates a simplified process flow for device fabrication, which includes the following major steps.

5.3 Device fabrication steps

5.3.1 Wafer preparation for silicon etching

Silicon wafers with 300 nm standard low-pressure chemical vapor deposited (LPCVD) nitride were purchased from University Wafers, Boston, MA, USA. Fabrication initiated by cleaning the wafers in acetone and isopropyl alcohol (IPA), followed by deionized (DI) water rinse. Post cleaning, a layer of 4 nm/500 nm titanium (Ti)/ copper (Cu) was thermally evaporated (Auto306, Edwards) and chemically patterned using a photoresist mask. Ti was deposited as an adhesion layer and Cu
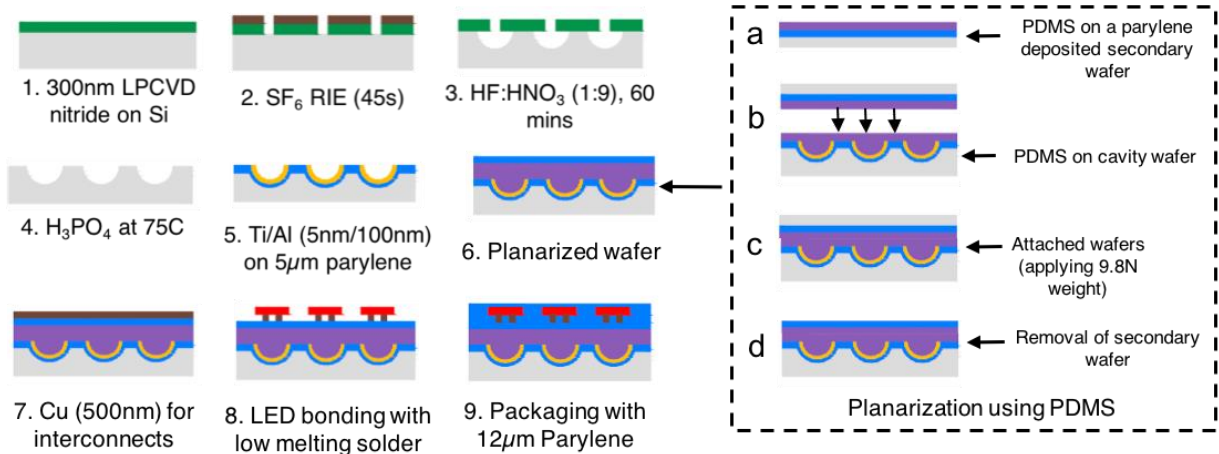
Figure 5-2. A simplified fabrication process flow. Steps (a)-(d) illustrate the planarization process.

acted as a mask for nitride etching because of its low etching rate in SF6 plasma[127]. A positive photoresist mask (Shipley S1813, MICROCHEM Corp.) was patterned using ultraviolet (UV) lithography. The unwanted Cu and Ti were removed chemically using Cu etchant (ferric chloride, MG chemicals) and hydrofluoric acid (HF) respectively, followed by DI water rinse. After that, the LPCVD nitride was patterned in a reactive ion etcher (RIE 1701, Nordson March) using 20 sccm SF6 plasma at 250W RF power for 45 seconds. After the reactive etching, the Cu and Ti used for masking were completely removed using the process mentioned above.

5.3.2 Silicon etching

The formation of hemi-spherical cavities utilizing chemical etching is achieved by a mixture of hydrofluoric and nitric acid, $HF:HNO_3$. Based on the solution recipe reported by Albero et al., in this paper[141], we studied several different combinations of masking materials to determine the best protocol for wet silicon etching, including plasma enhanced chemical vapor deposition (PECVD) silicon oxide (SiO), PECVD nitride and LPCVD nitride. For the samples, PECVD nitride was

45

deposited at 300 °C on 375 μm thick silicon wafers using an Oxford PlasmaLab 80 Plus PECVD. It was observed that for a PECVD nitride coated silicon wafer, the nitride layer was rapidly stripped in an $HF:HNO_3$ (1:9 by volume) solution. An addition of acetic acid, to create a solution of $HF:HNO_3:CH_3COOH$ (1:9:1 by volume) did not retard the etching rate of the PECVD nitride. A single layer of SiO (100 nm) and a stacked layer of PECVD nitride (100-300 nm) and SiO (100 nm) on silicon were also studied, which, however, show faster etching rates in the 50°C $HF:HNO_3$ solution. LPCVD nitride, on the other hand, was very resistant to the $HF:HNO_3$ chemical, thereby providing an optimum masking layer for the etch.

To fabricate hemi-spherical cavities, LPCVD nitride coated silicon wafer samples were submerged in the $HF:HNO_3$ (1:9 by volume) solution for 60 minutes at room temperature. No agitation was applied during this step in order to better control the etching rate and surface smoothness. From our experiments, it was evident that the LPCVD nitride mask is imperative for the wet etching, in contrast with PECVD nitride or SiO. After the etching, the nitride mask was stripped off using phosphoric acid at 75 °C. Finally, the wafer was rinsed with DI water before the metallization step.

5.3.3 Reflector formation

A 5-μm-thick Parylene C layer was deposited (SCS Labcoter 2-PDS 2010, Specialty Coating Systems) over the etched silicon cavity, followed by thermal evaporation of 100 nm aluminum (Al) (Auto306, Edwards). The deposited Al was selectively patterned using a Shipley S1813 photoresist mask and etched with Transene Aluminum Etchant A. It should be noted that this selective Al etching is optional, however, this step was performed to eliminate the possibility of reflection from LED side

emission which might reduce the spatial resolution. Moreover, because the interface strength between large area Al and PDMS is not well understood, the Al layer was selectively etched to ensure a good adhesion. Due to its high reflectivity, the Al within the cavity is expected to work as the mirror for reflecting the LED backside emission and focusing the diverged light beams.

5.3.4 Planarization using PDMS

Due to the presence of the cavities, planarization using polymers was desired in order to create an even surface for fabricating interconnect wires and contact pads for LED integration. Polydimethylsiloxane (PDMS) was selected as the planarization polymer due to the ease of processing and also its lower refractive index (1.4) when compared with SU-8 (1.67). PDMS pre-polymer was prepared by mixing the elastomer base and curing agent in a weight ratio of 10:1 (Sylgard 184, Dow Corning). During planarization (Figure 5-2), a Parylene C coated secondary wafer was spin-coated with a 10-μm-thick PDMS layer (5000 rpm, 60 seconds). Concurrently, a thin layer of PDMS was coated on top of the primary wafer where the cavities were constructed. Both the primary and secondary wafers were coated with PDMS to ensure sufficient PDMS filling in the reflector cavity and optimal adhesion. The primary wafer was then attached with the secondary wafer on the PDMS coated sides. The bonded wafers were subjected to a 9.8 N weight (16.33kPa pressure) for 24 hours at room temperature (25 °C) until the PDMS adhesive cured completely. This slow curing step allows PDMS to flow into the cavities with minimal air bubbles. After the soft curing, the bonded samples were baked in a vacuum oven at 50 °C for 30 mins, followed by a 100 °C bake for 5 mins. The higher temperature baking at 100 °C ensured hardening of the PDMS layer towards further metallization and LED bonding processes. After hard baking, the secondary wafer

47

was completely detached from the rest of the sample by delamination at the Parylene-silicon interface, resulting in the planarized Parylene-PDMS-Parylene structure to rest only on the primary wafer[142].

5.3.5 Interconnect metal deposition and LED bonding

A 5 nm/600 nm Ti/Cu layer was thermally evaporated, followed by UV photolithography with a Shipley S1813 photoresist mask. The photoresist mask was stripped off by rinsing the sample with acetone, IPA, and DI water. Afterward, a thin Parylene C layer (2 μm) was deposited and selectively patterned to expose the bonding pads by oxygen plasma (58 sccm O2, 250 W). Commercially available CREE TR2227 blue LEDs were bonded onto interconnect metal pads by applying low melting point (LMP) solder (melting point at ~ 62 °C, 144 ALLOY Field's Metal, Rotometals, Inc.) on the exposed metal contacts[64].

5.3.6 Packaging

After LED assembly, the arrays were completely encapsulated by 15 μm Parylene C to protect the devices from delamination, deformation, and corrosion due to the humidity and tissue fluids present in the in vitro and in vivo environments. The contact pads were connected to the power supply through flexible wires.

5.4 Device characterization

Surface morphology and optical property measurement

Silicon cavities were scanned in a NanoMap-500LS Surface Profilometer to quantify the horizontal

and vertical etch profiles of the cavities. Inspection of surface topography was done using a Hitachi S-4700II field emission scanning electron microscope (FESEM). The surface roughness of the Al-coated reflective layer was measured using an atomic force microscope (AFM, SPM 3100, Veeco). Light intensity for both the bare LED and reflector-coupled devices were measured using a Newport 818-SL optical detector and Newport 843-R series optical power meter. The devices were tested under a probe station in air, and the detector was placed at a distance of 7 mm above the LED surface in all of the optical measurements.

5.5 Thermal property measurement

The temperature profile of the stimulator during continuous operation provides critical information to study the effect of the silicon reflector on LED heat dissipation. When a single LED was continuously powered by ~1-25 mA current (~2.6-73 mW), the thermal energy dissipation of the array was characterized in air using a thermal imaging camera (FLIR E6, FLIR® Systems, Inc) with an infrared resolution of 160x120 pixels and a temperature sensitivity of 0.06 °C. The imaging camera was calibrated by the manufacturer. The temperature of the LED surface, being the spot where the temperature would be the highest, was recorded using the imaging camera. The maximal temperature increase at the activated LED site was quantified with respect to the ambient temperature (22 ºC) and compared to that of a bare µ-LED.

5.6 Finite Element Analysis

Optical intensity captured at a specific parallel plane from the LED surface was simulated using TracePro (Lambda Research Corporation). As illustrated in Figure 5-3(a), the model used for the

simulation consisted of a micro LED with the same physical dimensions as the CREE TR2227 LED (270 µm x 220 µm x 50 µm) and a silicon cavity with a reflective layer of a standard mirror (95%). Air was used as the surrounding medium to mimic the actual environment of device measurements. The effect of the reflective mirror on the optical intensity of the overall device was studied by varying the cavity diameter and the distance of the detector plane from the LED surface. For this study, the detector diameter of 10 mm was selected, which is consistent with the detector (Newport 818-SL) aperture used in the experimental setup. The percentage increase was calculated by normalizing the increased light intensity from the reflector-coupled LED with respect to the intensity of a bare µ-LED at a certain separation: $(I_{ref} - I_{bare})/I_{bare}$, where I_{ref} and I_{bare} are the simulated light intensity of reflector-coupled and bare LEDs, respectively. Figure 5-3 (b) shows that the intensity enhancement goes higher as the diameter of the reflector cavity increases from 100 µm to 400 µm, and then drops gradually as the cavity diameter continuously increases. For a 300 µm diameter reflector, an intensity enhancement of 78% was achieved, when compared to a bare LED without a reflector. A better localization of light beams was observed when the hemi-spherical cavity was compared with a planar mirror in simulation. Figure 5-3(c) shows the quantitative analysis of centralized illumination area using spherical reflector over a planar mirror calculated at different distances from the LED surface, while Figure 5-3 (d, e) shows the examples of simulated light spots at the same separation in the same intensity range. The center spot beam localization was estimated by calculating the central area of the beam (from the planar mirror or hemi-spherical reflector) at the same intensity level and at the same distance from the detector. Fitted curves have been included in Figure 5-3(c) to indicate the trend of center beam localization for the mentioned geometries, and shows an advantage of the hemi-spherical cavity reflector over a

planar mirror, in terms of localized beam area reduction. This advantage will enable better spatial resolution of optical stimulation, which is desired for optogenetics applications.
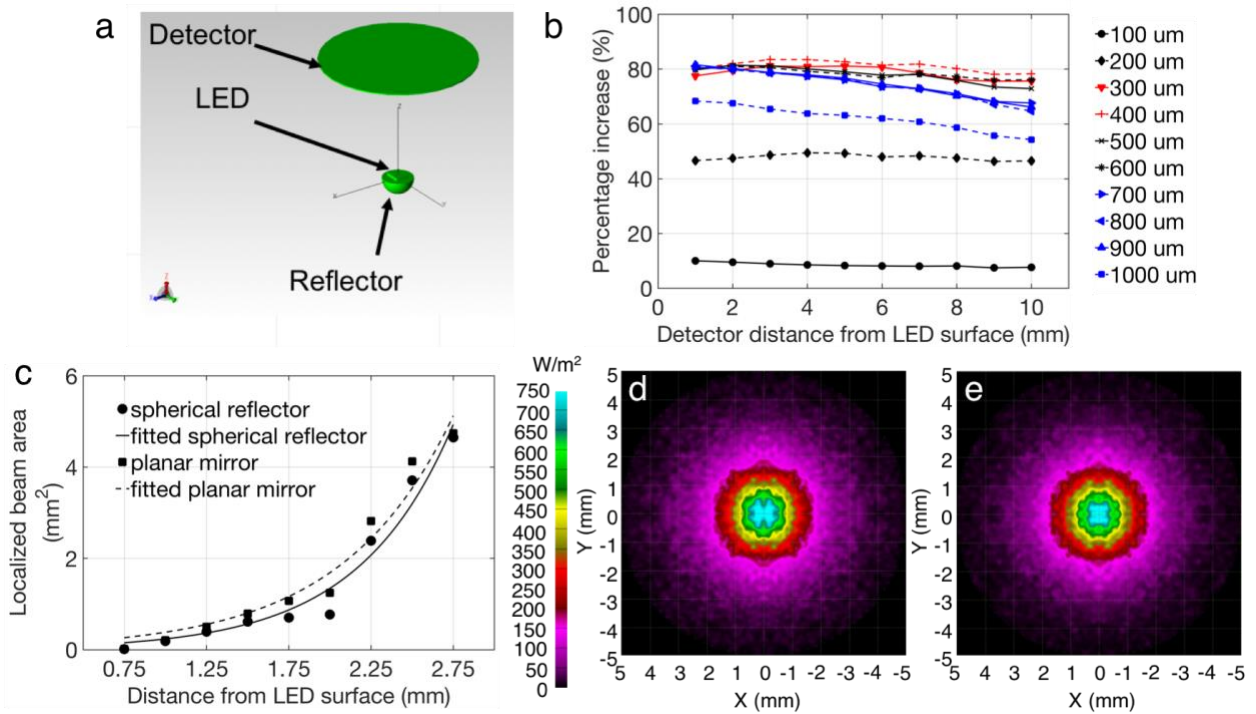
Figure 5-3. (a) Simulation model in TracePro. (b) Simulation showing the optical intensity enhancement of the reflector-coupled device, as compared with a bare LED (without any reflector). Legend refers to cavity diameter. (c) Focused beam areas using planar and spherical reflectors with fitted curves, calculated at various distances from the LED surface (d), (e) example of beam localization between a planar mirror and spherical reflector, respectively at 1.5mm from the LED surface, colormap is the same for both (d), (e).

5.7 In vitro experiments

To establish proof-of-principle for application with an optogenetic system, we assessed the efficacy of the μ-LEDs to activate an optically-induced gene expression system[142] (with and without reflectors). Successful induction is confirmed by the visual identification of the expression

of a red fluorescent reporter following genetic modification and exposure to blue light. For these in vitro experiments, human embryonic kidney cells (HEK 293) were used. HEK 293 were maintained under Dulbecco's modified Eagle's medium (DMEM; Life Technologies) supplemented with 10% fetal bovine serum (FBS; Sigma) and 1% penicillin/streptomycin (Life Technologies). Colonies were passaged every 3-4 days by chemical dissociation utilizing TrypLE (Life Technologies). Cells were kept in an incubator at 37 °C with 5% $CO2$. Prior to light induction experiments, cells were passaged onto 24-well plates at 68,000 cells/well. Cells were then transiently transfected utilizing Lipofectamine 3000 (Invitrogen) by following the manufacturer's protocol. Each well was transfected with 200 ng of DNA including 40 ng of activator plasmid ("EL222", a blue light-activated gene expression system)[143], [144], 20 ng of reporter gene (red fluorescence protein, RFP) and 140 ng of PUC (an empty plasmid). Twelve (12) to sixteen (16) hours after DNA transfection, cells were exposed to blue light (465 nm) from LEDs for either 240 or 480 minutes. Two wells were exposed to standard (bare) LEDs, two wells were exposed to reflector-coupled LEDs, and four were kept under dark conditions as a control.

After light stimulation, cells were maintained in the incubator. After 72 hours, each well was imaged using a fluorescent microscope (Leica MZ10 F) to assess optical induction of the RFP reporter construct. All plasmids used in this study were provided by BiomiLab, LLC[144]. Individual images received manual threshold utilizing Ocular software (QImaging) to eliminate background fluorescence. Images from all wells were further analyzed with an in-house MATLAB script to calculate the number of "zero" pixels (where a fluorescent signal was not detected) and non-zero pixels (where fluorescent signal was detected) to obtain the percentage of pixels above threshold

(number of non-zero pixels divided by total number of pixels, % PAT, multiplied by a factor of 10,000 to facilitate comparison, Table 5-2) for each image. Lastly, an additional MATLAB script[145], [146] was used to assess the spatial gradient of gene expression in a preliminary test by creating bins of intensity in area increments (two wells were exposed to light for 480 minutes: one with the bare LED stimulator and the other with the reflector coupled stimulator). To assess images spatially, bins were utilized to quantify mean intensity as a function of distance from the center of the LED location. Twelve 200 micron-width bins were analyzed which projected radially from the center of the LED site. Location of the center was manually selected to accurately represent the center of the region that received direct light exposure. The LEDs were manually positioned at the center on each well, based on visual inspection. The manual procedure for LED placement, as well as the flexibility of the LEDs, likely contributed to a slightly off-center placement relative to the center of the well in Figure 5-6(a).

5.8 Results

5.8.1 Fabricated devices

Figure 5-4 (a) provides SEM images showing the morphology of the silicon cavity after wet etching. The cavity formation is the most important step for the reflector fabrication, and the surface morphology of the cavities need to be comparatively smooth to ensure efficient light reflection with minimum scattering. AFM analysis in Figure 5-4 (d) shows a small mean roughness of ~ 72 nm, confirming the smooth surface of the etched cavity. The horizontal and vertical etching rates of silicon cavities were calculated based on the profilometry data, as shown in Figure 5-4 (c). The results indicate that the etching rates in the horizontal and the vertical direction are not the same,
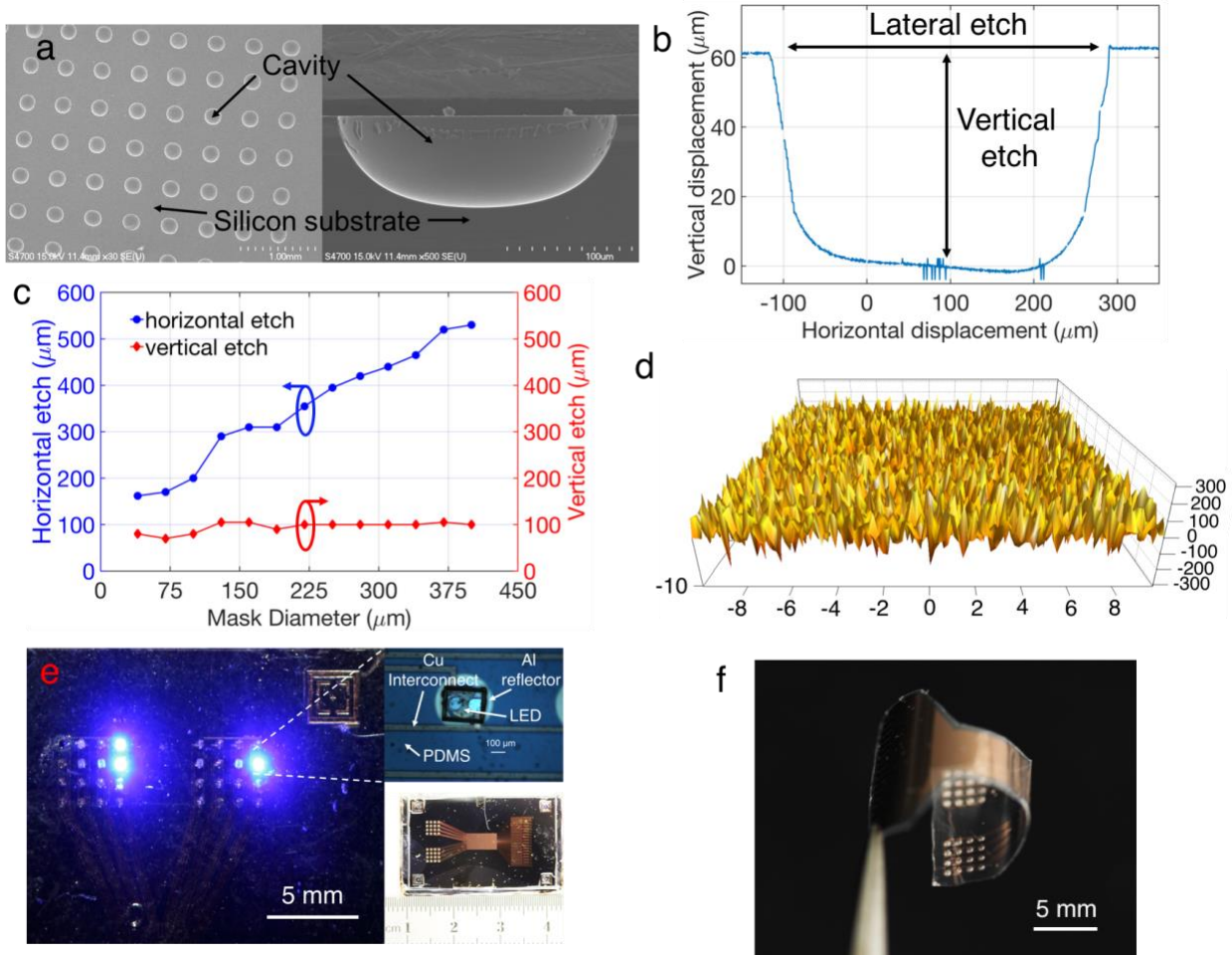
Figure 5-4. (a) SEM images of the etched silicon cavity (b) Surface profilometer results for calculating the etched lateral and vertical distances (c) The etched distance with respect to mask diameter. (d) AFM image showing the smoothness of the etched cavity (x axis units in μm, y axis units in nm) (e) A fabricated array stimulator, coupled with the cavity reflector (f) A released stimulator array before LED bonding.

with the opening of the nitride mask being a limiting factor. Due to the lack of agitation, the vertical etching rate is slower than the horizontal rate and less dependent on the size of nitride opening in Figure 5-4(c). This phenomenon forced the cavities not to be perfectly hemi-spherical, thereby creating a deviation between the theoretical concept and the realized cavity geometry.

Consequently, a deviation should also be expected between the simulation results (which considers the cavity to be perfectly hemi-spherical) and the experimental results. Figure 5-4 (e) illustrates a fabricated 32-channel stimulator array on a silicon chip, with illuminated LEDs on both panels. There is a slight misalignment between the LED bonding pads and cavity, due to the inaccuracy of the photolithography process. Deposition of the Parylene C layer allows the release of the array from the silicon substrate and transform it to a fully flexible free-standing stimulator array to adapt with corrugated brain surfaces by conformal contact. Figure 5-4 (f) shows a released array from the substrate wafer, where the bending is due to the mechanical stress of the thin Parylene C layer after release, and could be reduced by stabilizing and flattening the array on a separate substrate using water as adhesive.

5.8.2 Optical properties

Figure 5-5 (a) shows the optical intensity enhancement due to the coupled reflector, which was measured experimentally with respect to a bare (no-reflector-coupled) optical stimulator. The reflector-coupled devices achieved the minimal and maximal enhancement of 49% and 65%, respectively, verifying the effectiveness of the reflector to collect the rear surface emission of the LED. For these benchtop experiments, the LEDs were coupled with 300-μm-diameter reflectors that ensure the optimized intensity enhancement as suggested by the simulation above. The experimental data was slightly lower than simulated values, which could be attributed to several factors: fabrication imperfections, oval-shaped cavity profile, inaccuracy of manual alignment between the LED and reflector layers, and high contact impedance of the LED-solder-contact interface. Regarding in-vivo experiments, a common excitatory opsin is channelrhodopsin (ChR2)

that can be activated by blue light with threshold of 1 mW/mm^2[11]. Preliminary benchtop measurements indicate that our intensity enhanced stimulators surpass this threshold even at a low applied current of < 2.5 mA. It is of note that the detector and LED surface had a separation of 7 mm due to the use of a probe station. The measured intensity might be further improved if the separation could be reduced by improving the measurement setup.

5.8.3 Thermal properties

Although the brain is only 2% of the body's mass, 20% of the cardiac output is delivered towards it, indicating a high metabolic demand in the brain[147]. A high resting blood flow clears the heat generated by the brain. Adverse effects of increased temperature due to implants, on top of this high metabolism activity have been observed in the central nervous system (CNS) where breakdown of blood-brain barrier was observed after 60 minutes at 42 °C along with some neuronal death (6%) after 60 minutes of heating at 40.5 °C[148]. A maximum tolerable heat dose of 42.0 to 42.5 °C for 40 to 60 minutes or 43 °C for 10 to 30 minutes[149] was established after a review study on regional exposure of the animal brain and spinal cord. The American Association of Medical Instrumentations (ANSI/AAMI) has a standard limit of 2 ºC increase for chronic biomedical implants for neuro-stimulators (ISO-14708-1). A change in temperature was calculated by subtracting the initial temperature (~22 ºC when the LED was off) from the operating temperature of the LED measured by the infrared camera. A temperature increase of < 1 ºC was observed when our stimulators were operated under continuous current inputs in Figure 5-5 (b), even at higher light intensities (> 8 mW/mm2). It could be noted that when compared with bare LEDs, the reflector-coupled stimulators dissipate less heat at > 8 mW/mm2 intensities,

potentially due to the decreased thermal conductivities of silicon and PDMS at higher temperatures [150].
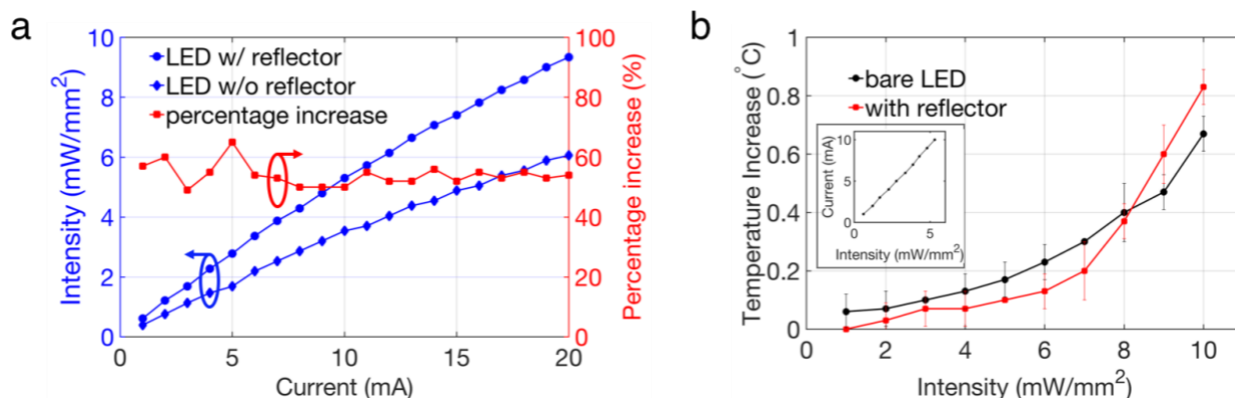
Figure 5-5. (a) Optical intensity and (b) temperature increase compared with a bare micro LED stimulator (in inset-correlation of intensity vs current for reflector coupled stimulators)

5.8.4 In vitro results

In vitro tests confirmed proof-of-principle for the successful induction of red fluorescent reporter expression with μ-LEDs, as well as a more robust and spatially localized area of induction with the use of reflectors (Figure 5-6, Table 5-2). Fluorescent microscope images of each well were analyzed for either %PAT or intensity at each of the various duration settings chosen for light exposure. Qualitatively, light-induced gene expression was visually observable following 240 minutes of exposure in Figure 5-6 (a). Table 5-2 shows %PAT values obtained from our first in-house MATLAB script and represents average values of %PAT for two images per condition (n=2, where the entire image area is quantified to deliver a single output value) for a blue-light exposure duration of 240 minutes and %PAT values for one image per condition (n=1) for a blue-light exposure duration of 480 minutes. As expected, light-stimulated wells registered higher %PAT
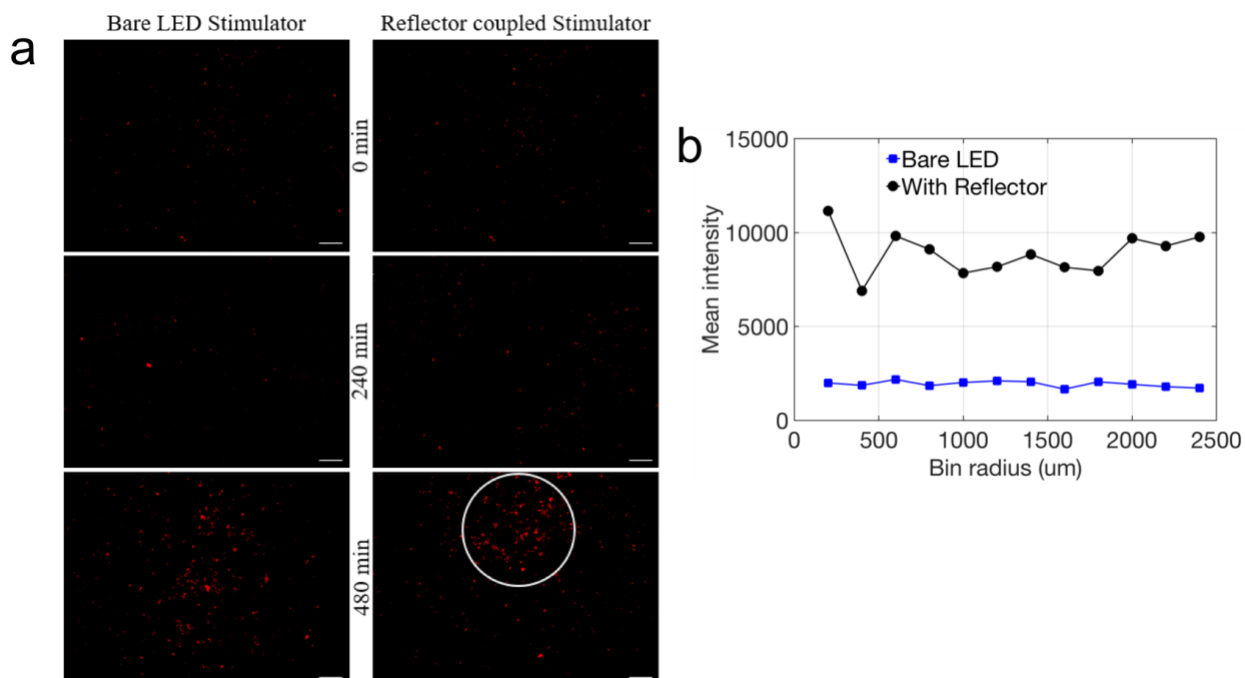
Figure 5-6. (a) Comparison of bare LED stimulator and reflector coupled stimulator fluorescence of RFP reporter for 0 min, 240 min and 480 min (scale = 1 mm) (b)Mean intensity data with respect to bin radius (n=1).

Table 5-2. Average %PAT (multiplied by a factor of 10,000 to facilitate comparison) for control,

bare LED stimulator and reflector coupled stimulator.

Average %PAT per condition	240 min (n=2)	480 min (n=1)
Control (no light)	6.86	17.21
Bare LED stimulator	12.12	83.41
Reflector coupled stimulator	17.37	88.39

values than non-exposed wells, verifying successful optical induction of the reporter gene (Table

5-2). Due to the residual dark-state binding of the activator, some fluorescence in dark conditions

was observed and served as a baseline for quantification. At 480 minutes, higher %PAT values were measured for the cells exposed to both the reflector coupled LEDs and for the bare LEDs when compared to the 240 min exposure duration (Table 5-2). Additionally, reflector-coupled LEDs registered slightly elevated %PAT values for both timepoints.

Utilizing our second MATLAB script, preliminary observations suggest a more spatially localized pattern of reporter expression at 480 minutes [white circle in Figure 5-6 (a)] potentially related to focused illumination enabled by the reflectors. To analyze the expression pattern as a function of distance from the center of induction, mean intensity per bin was calculated and normalized by using the corners of each image. This confirmed elevated expression in comparison to standard LEDs within the highlighted region of interest in Figure 5-6(a).

In this chapter, the author has designed, fabricated, simulated and characterized a multichannel, reflector-coupled μ-LED array for optogenetic experiments. A wafer-level fabrication method was implemented to monolithically integrate multichannel reflectors with μ-LEDs. Our experimental results demonstrate that using the Al-coated cavity as a back reflector enables significant enhancement in light intensity by at least 49% and a maximum of 65% in comparison to a bare μ-LED. Simulation using optical ray tracing verified the effectiveness of the reflector to improve the output light intensity, while also providing a guideline towards future optimization of device design. Additionally, the 32-channel stimulator array allows high-resolution spatial stimulation, enabling multi-site stimulation for localized neuronal activity analysis. Furthermore, the structural and packaging material used in our device is Parylene C, which ensures the biocompatibility and

reliability of the stimulators in the brain fluids. When compared with optical fiber based stimulators, the proposed array is advantageous in terms of multi-site stimulation and motivates toward an untethered wireless device. In addition, the array demonstrated improved heat dissipation (<1°C), compared to an optical fiber based stimulator reported by Y. Shin et al.[151] where a temperature increase of 1-1.5°C was observed . Finally, the effectiveness of the reflector-coupled LEDs for localized light induction of optogenetic DNA was validated *in vitro* using human embryonic kidney cells.

With the aim towards a multichannel untethered optical stimulator (as a 2nd generation prototype), the following chapter demonstrates a head mounted battery powered module with multichannel (2x2) stimulators and recording electrodes (1x2) being capable of wirelessly receive signal and transmit ECoG data modalities, show real time recorded ECoG using a GUI and store data in a PC for further analysis.

Chapter 6. A Battery Powered Optrode With Wireless Telemetry

The previous chapter describes the approach of coupling a passive reflector to enhance the light intensity in flexible μ LED array stimulator. Although the flexible μ-LED array stimulator paves the way for a truly untethered stimulation device, however the device demonstrated in the previous section still remains as a tethered device as it has to receive the operating power from wired power source.

6.1 Concept description

As a transition towards an untethered system, this chapter proposes and demonstrates a wireless opto-electro neural interface system, including ECoG recording and optical stimulation modalities for experiments with small freely behaving animals. The system consists of 1) a headmounted module, which would be attached on an animal subject, 2) a opto-electro neural interface, integrating 4 μLEDs and 2 recording electrodes, 3) a custom-designed dongle, and 4) a personal computer (PC) in order to store data and provide a graphical user interface (GUI). The headborne module wirelessly communicates with the dongle through a bluetooth low energy (BLE) link. The module's bi-directional signal transmission capability could be driven selectively by receiving and acting on user commands set in the GUI. Simultaneously, the recorded ECoG signal are amplified, digitalized, and wirelessly sent to the dongle, which is plotted in GUI in real time to monitor the functionality of the system. Also, the ECoG signal is saved in the PC for further data processing.

6.2 Control circuitry and flexible stimulator design

A simplified conceptual diagram of the proposed wireless optoelectro neural interface system[84]
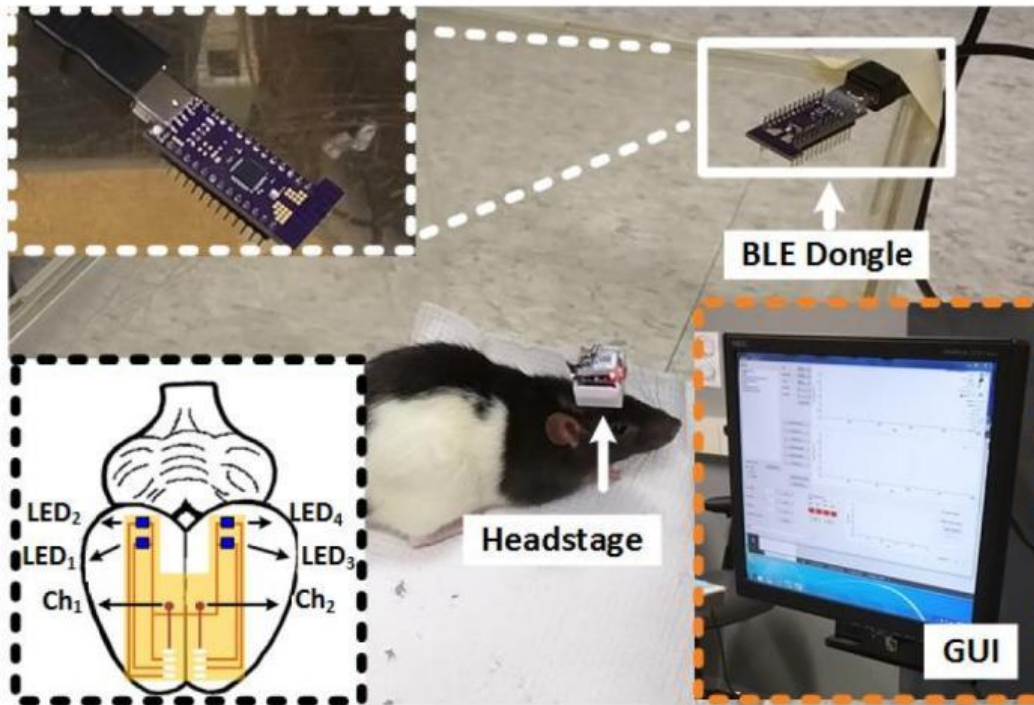
Figure 6-1. In vivo experimental setup of the wireless opto-electro neural interface system with a freely behaving rat. Reprinted with permission and courtesy of Dr. Yaoyao Jia (Georgia Institute of Technology) and Adapted from [84].
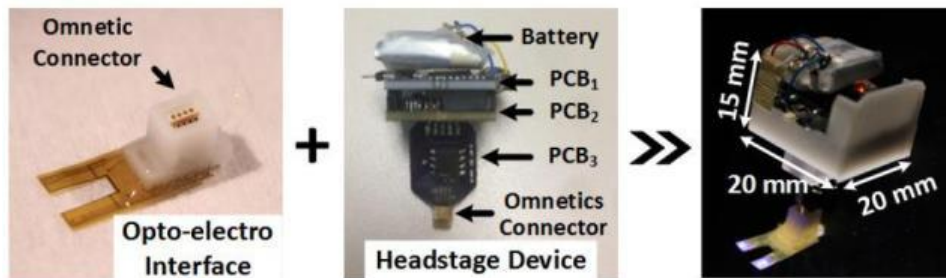
Figure 6-2. Close-up view of the hesadstage with the implanted neural interface. Reprinted with permission and courtesy of Dr. Yaoyao Jia (Georgia Institute of Technology) and adapted from [84].

for small freely behaving animals is provided in figure 6-1. The GUI serves a dual purpose of sending instruction to the headborne unit and to provide real time ECoG feedback. Upon receiving user commands from the GUI, the master micro controller (CC2540) in the dongle establishes a link via BLE with the slave micro-controller in the headborne module (CC2541). The later module's

firmware includes two main functions: 1) periodical stimulation and recording and 2) data tranmission. The establishment of BLE link enables the user to trigger the periodic stimulation/recording function.

6.3 Optrode design

The concept of the optrode[152] includes two separate flexible and biocompatible film panels, i) the stimulation panel and ii) the recording panels bonded together to erect the complete structure. The stimulation panel had two sub arrays, each having two bonded µ-LEDs separated by 1 mm distance. The optrode had a two shank design in order to evoke excitable cell activity from both cortices. Reducing photo electric artifact is a persisting challenge and to address the issue, recording electrodes were designed to be at a distance ~5 mm from the closest stimulation channel. The stimulation and recording channels were connected to the head-mounted PCB's via an 8pin omnetics connector.

6.4 Optrode fabrication

Fabrication of the stimulation panel started by spin coating positive photoresist (S1813, Shipley) on a 9um double sided copper (Cu) cladded polyimide film. Cu was patterned by UV lithography and excess Cu was etched with Cu etchant (Ferric Chloride solution, MicroChem). µLED's (CREE TR2227tm) were bonded on the copper using low temperature melting solder. The panel was packaged with a layer of Parylene to provide insulation and protection from damage.
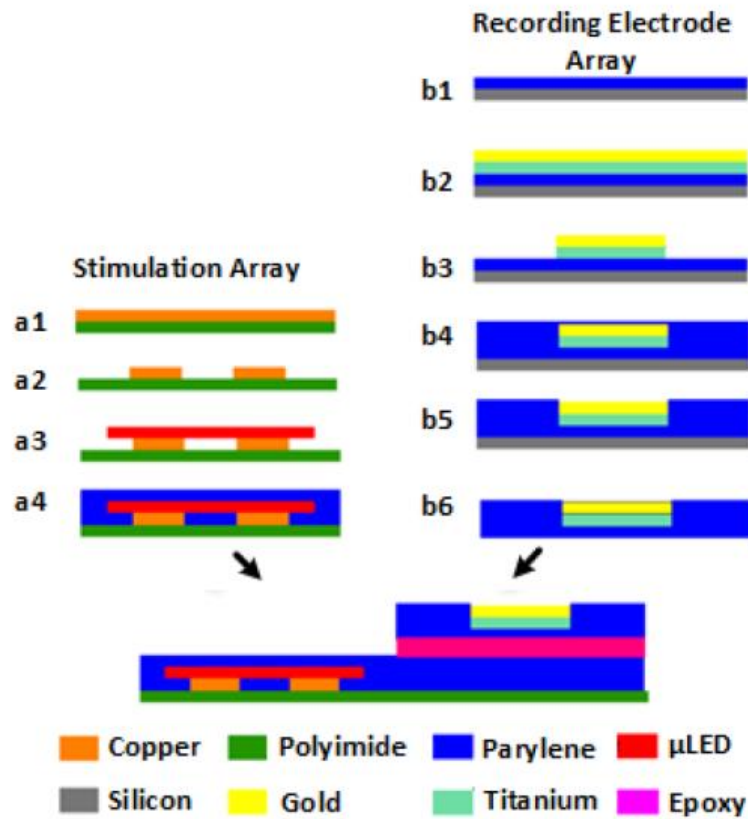
Figure 6-3. The fabrication process flow of the opto-electro neural interface.

Fabrication of the 500 μm diameter recording electrodes initiated with chemical vapor deposition of 12 μm Parylene on a silicon wafer, followed by thin films of titanium (Ti) and gold (Au) deposition. Au and Ti were patterned by potassium iodide and hydrofluoric acid, respectively. The array was then packaged by Parylene followed by oxygen plasma etching to selectively expose the recording sites. The fabricated stimulation and recording panels were bonded using medical grade epoxy. The fabrication steps are illustrated in Figure 6-3.

6.5 In-vivo behavioral experiment on free moving rodents (rats)

To verify the surgical and functional applicability of the proposed head mounted module and the implanted wireless opto-electro neural interface system, in vivo animal experiments were conducted. All procedures were approved by the Institutional Animal Care and Use Committee (IACUC) at Michigan State University. Adult rodent subjects (Long Evans, female, 300– 400 g) received virus injection (AAV-hSyn-hChR2 (H134R)-m Cherry; UNC Vector Core) in the primary visual cortex (V1) to express neurons with light sensitive channelrhodopsin-2 (ChR2) prior to device implantation. The injection surgery was performed under a inhalation anesthesia (Isoflurane and oxygen mixture, 2-4% vaporizer) while the subject was on a stereotaxic apparatus. 3-4 cm incision was created in the skin and 3 equidistant holes were drilled on each cortex. The AAV virus (10^{12}~10^{13} genome/mL) was injected to the brain through the holes, delivering 1.0 µL in each drilled location. After successful injection procedures, the cortex was covered with gelfoam and then the skin sutured close.

The injected rats were housed separately and given pain medications to reduce discomfort and antibiotics to prevent infections. Two weeks' post injection surgery, the subjects were placed back on the stereotaxic apparatus again with the anesthesia procedure mentioned above. The flexible multichannel opto-electro array was surgically implanted over V1 and firmly attached onto the skull using dental cement. A grounding wire was inserted under the skin to reduce artifacts. The skin was sutured while the Omnetics connector (housed in a 3D printed case to prevent short circuit and damage) was exposed for connection to the detachable, wireless head-mounted control module. Manual attachment and detachment of the headborne module was performed

before and after the experiments. The experimental subject was allowed to move freely in the homecage while stimulation with different parameters (i.e. current level, frequency and duty cycle) were applied on the animal cortex. Simultaneous animal movements were recorded using a Kinect sensor (Kinect 2.0, Microsoft) to analyze the movement of the animal during stimulations. A total of four experimental subjects were used with an experiment interval of 7 days, for each subject. Data analysis indicates a constant result, thereby validating the stability and reliability of our system up to 21 days after implantation.

6.6 Experimental Results

6.6.1 Immunohistology analysis

To validate the efficacy of the optical stimulation, immunohistology analysis using c-Fos biomarker was performed on the stimulated and control cortex (V1). As a standard c-Fos protocol, the anaesthetized experimental subject's brain was stimulated for 45-60 minutes. A 75-90 min. survival period was provided post stimulation. Later, the subject was perfused with chilled saline and 4% paraformaldehyde, post-fix brain overnight at 40ºC in the same solution. Brain sections
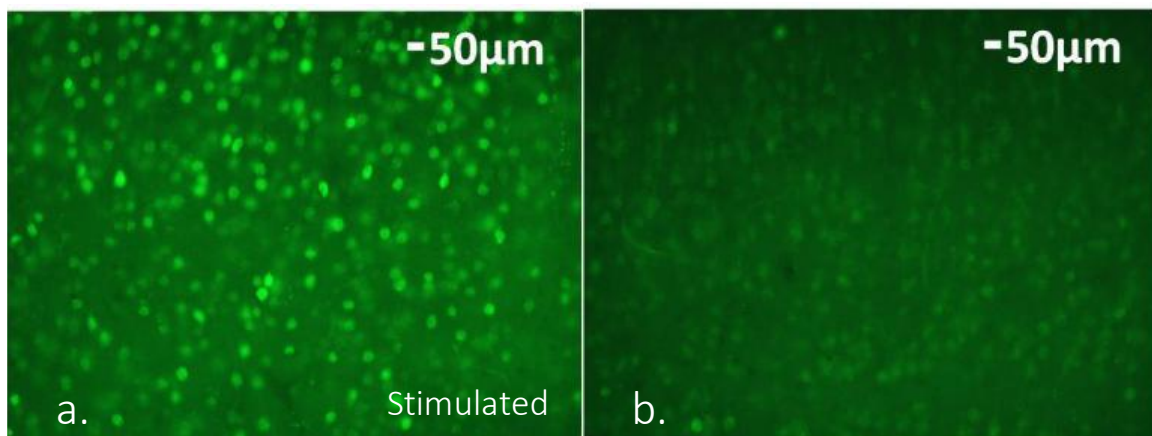
Figure 6-4. Immunohislogy analysis results on the a) stimulated V1 b) Control V1

were cut (50 μm thickness) and chilled in 0.1M phosphate buffer and place in 12 or 24 well shaped tissue culture dishes for immunohistology analysis. 2ml solution was found to be sufficient for immunohistology. Sections were washed three times for 10 minutes in PBS (phosphate-buffered saline). Post wash, sections were soaked in PBS containing 1% NGS and 0.3% Triton X-100 for 2hrs at room temperature (25ºC). 1ml of pre-made antibodies (rabbit mAb) were placed in 1.5ml Eppendorf tubes. Eppendorf tubes were clipped onto a rotating mixer and stored at 40ºC for 24 or 48 hr. incubation. Sections were poured into 24 well shaped culture dish wells for washing, three times by 10 mins each- in 0.1% Tween-20 in PBS. Later, they were incubated in the dark with 20 antibodies (ThermoFisher A27034 goat anti-rabbit IgG superclonal Alexa Fluor 488 conjugate) for 2hrs. at room temperature. Finally, they were washed in 0.1M phosphate buffer, mounted and cover slipped with anti-fade solution – and stored in a cool dark place.

The results illustrated in Figure 6-4 (a) indicated a higher population of neurons (bright green in the image) expressing c-Fos biomarker in comparison with the control cortex in Figure 6-4 (b). This up regulation in the stimulated cortex is a metric of the stimulation efficacy provided by our stimulators *in vivo*[153], [154]. It should be noted that the control cortex also shows some c-Fos expression, which could be due to the mechanical pressure on the cortex during the surgical procedures.

6.6.2 ECoG signal analysis

Optical stimulation was provided to the right visual cortex using constant-intensity light pulses with pulse width of 10 ms, frequency of 1 Hz, and optical intensity of ~4mW/mm^2, and the
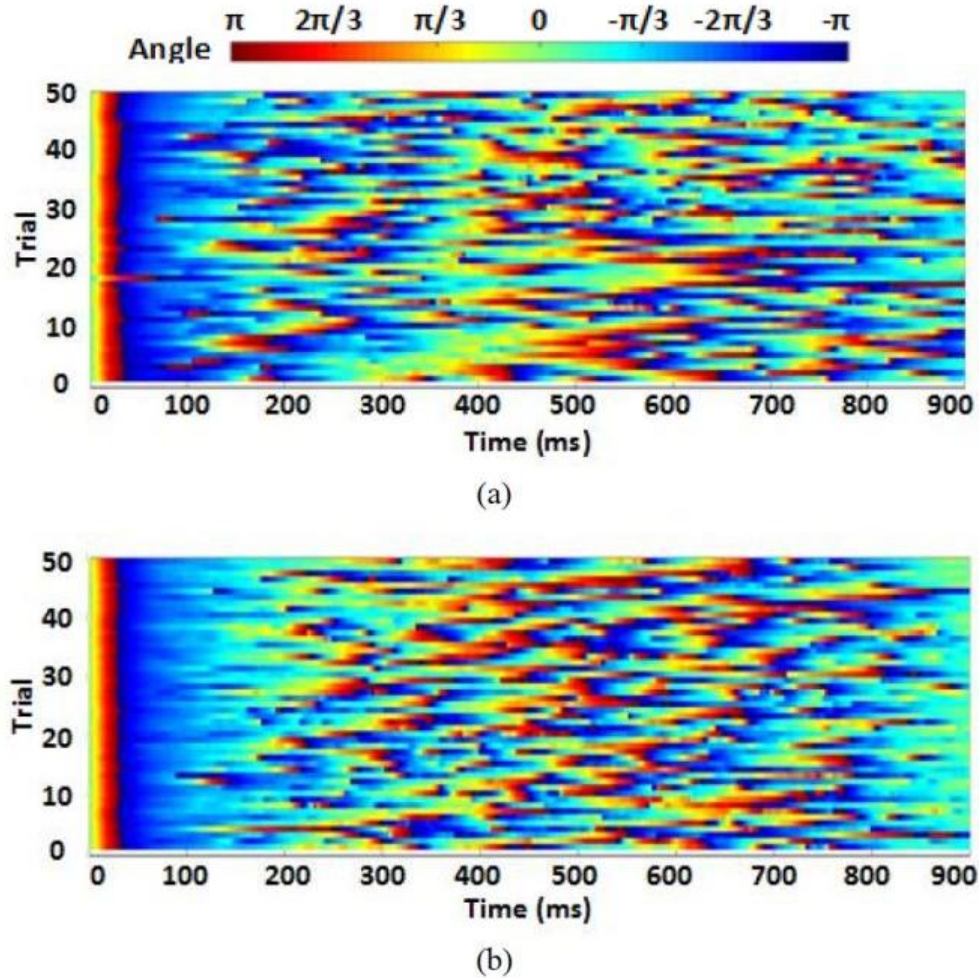
Figure 6-5. Instantaneous phase of the light-evoked ECoG signal with stimulation current of (a) 5 mA and (b) 10 mA. Reprinted with permission and courtesy of Dr. Yaoyao Jia (Georgia Institute of Technology).

non-stimulated left cortex was used as control to compare the difference. Using the recording

modality of the head mounted module, microelectrode on the right visual cortex recorded the

light evoked ECoG simultaneously. Stored digitized ECoG data was later analyzed with MATLAB

and chronux toolbox. The analysis presented in this chapter is reprinted with permission and

courtesy from Dr. Yaoyao Jia, Georgia Institute of Technology that includes 50 one-second trials of

stimulation and simultaneous neuronal changes. In order to clearly visualize the light evoked

changes on the stimulated V1, instantaneous phases of the ECoGs (2 ~ 25 Hz) were measured based on Hilbert transform and shown in figure 6-5 (a,b). It was observed that a stronger phase synchronization is achieved with a larger stimulation current. Prominent phase locked neuronal oscillations with ~200ms latency was obtained with an applied stimulation current of 10mA in Figure 6-5(b), and ~150ms phase synchronization was seen to be prominent with the application of 5mA in Figure 6-5(a). The prominent phase locked oscillations indicate the reliability of the neuromodulations over the trials and confirms the efficacy of the proposed stimulation and recording system.

This chapter discusses the development and efficacy of a battery powered head mounted module capable of bi-directional communication. The multi-channel stimulator effectively activated the light sensitive opsins, which was validated by the detected up regulation of the c-Fos biomarkers. The efficacy of the stimulation was further enhanced by the ECoG data analysis which demonstrated a prominent phase lock for 150ms and 200ms for multiple trials, for 5mA and 10mA current respectively.

Although the head mounted battery powered module provided significant efficacy towards optical neuromodulation and provides a game changing approach towards achieving untethered and wireless neural interface, however the challenges of manual attachment and detachment, the implant size and the head mounted modules size and mass affects the natural behavior of the experimental subject. The manual handling of the interface and the mass could create pain for the subject, and hence could significantly alter its behavior. More importantly, the size and weight of

the head-mounted electronics it might not be viable for longer duration experiments.

In order to establish a truly untethered, miniaturized and efficient neural interface, the following chapter explores the concept of wireless power transfer using coil links to operate a single channel, miniaturized optical neural interface, aiming to reduce the size and mass and provide a fully implantable neuro-stimulator.

Chapter 7. Inductively Coupled Single Channel Neuro Stimulator

The optical stimulators described in the previous sections were either tethered or had to be connected with a head borne power supply and telemetry module. Although the tethered optical stimulators provide more than sufficient optical intensity, and the head borne power supply and telemetry module provides flexibility and free behavior of the experimental animal to some extent, they however have their own disadvantages.

The drawbacks of the tethered stimulators had been mentioned in chapter 2 previously. The head borne module however, needs manual attachment/detachment by the researchers during each experiment session. This requires application of force and could possibly damage the module itself, and could also damage or cause inflammation of the target tissue. The added mass and size of the head mounted module could possibly initiate pain on the surgical wound. These conditions could significantly influence the natural behavior of the animal, especially when behavioral change
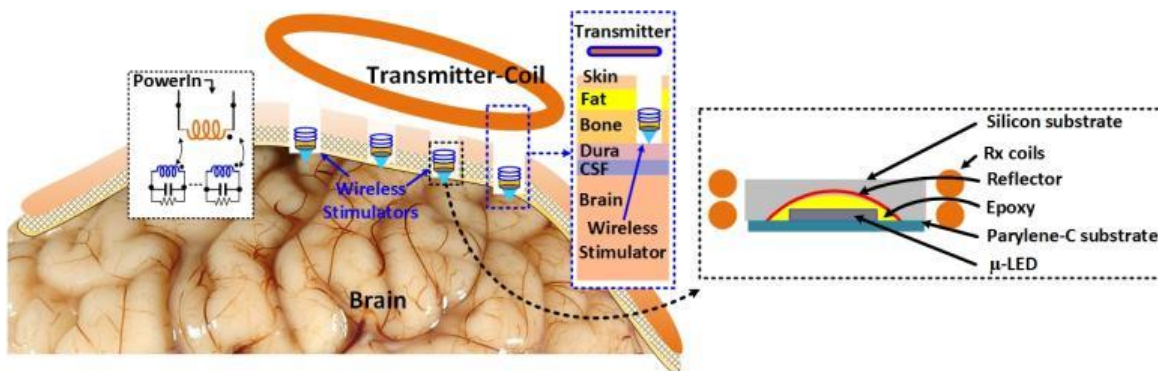
Figure 7-1. Conceptual diagram of the wirelessly-powered opto neuro-stimulator and its placement in animal brain.

is expected from the experiment. A solution to this challenge lies in the concept of a wirelessly powered and miniaturized neuro stimulator as an implant. However, power transfer at a high

frequency is harmful for the tissue, and could cause reduction in nerve vitality and tissue damage[100]. Also there is possibility of radiation over exposure and microwave induced tissue heating when frequencies are in GHz range[100]. In this chapter, the author proposes a fully implantable, miniaturized, wirelessly powered optical stimulator, using a mm-sized Rx coil optimized at a low resonant frequency of ≤100 MHz to deliver sufficient power for μ-LED operation. The optical source consists of a single μ LED being coupled to a microscale, highly reflective lens to enhance optical throughput and penetration depth of LED illumination for effective epidural neuro-stimulation with minimal invasiveness and good spatial resolution. In this chapter, the author proposes the optical-neuro stimulator and validates its efficacy through immuno-histology analysis.
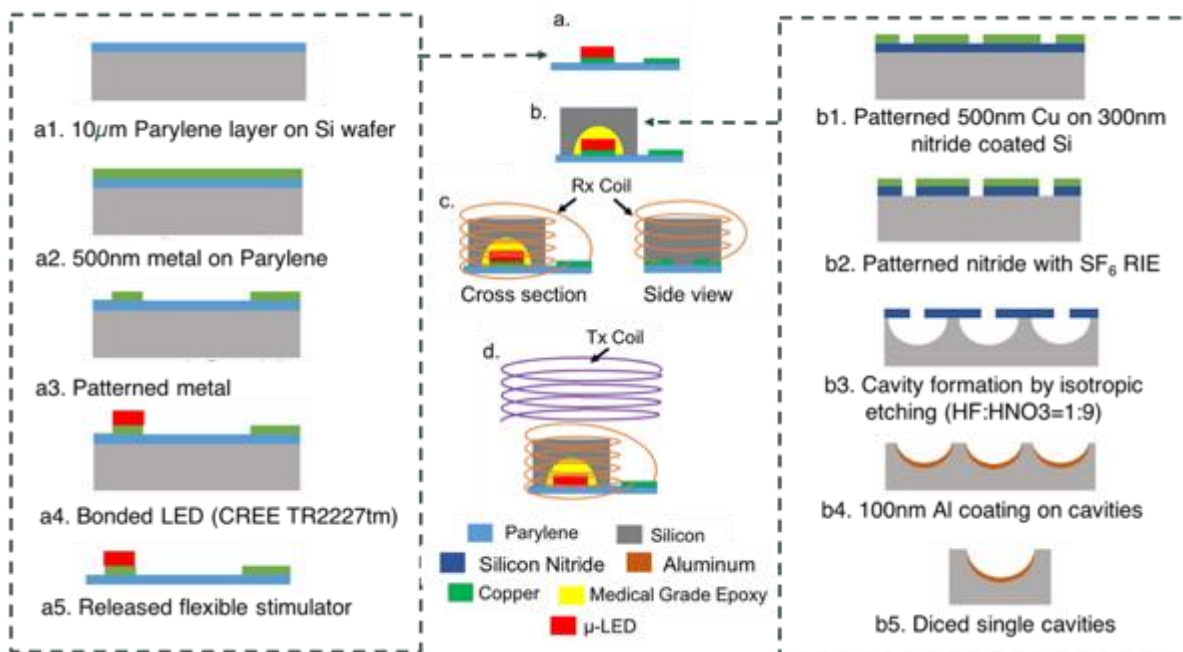
Figure 7-2. Simplified fabrication and integration process flow
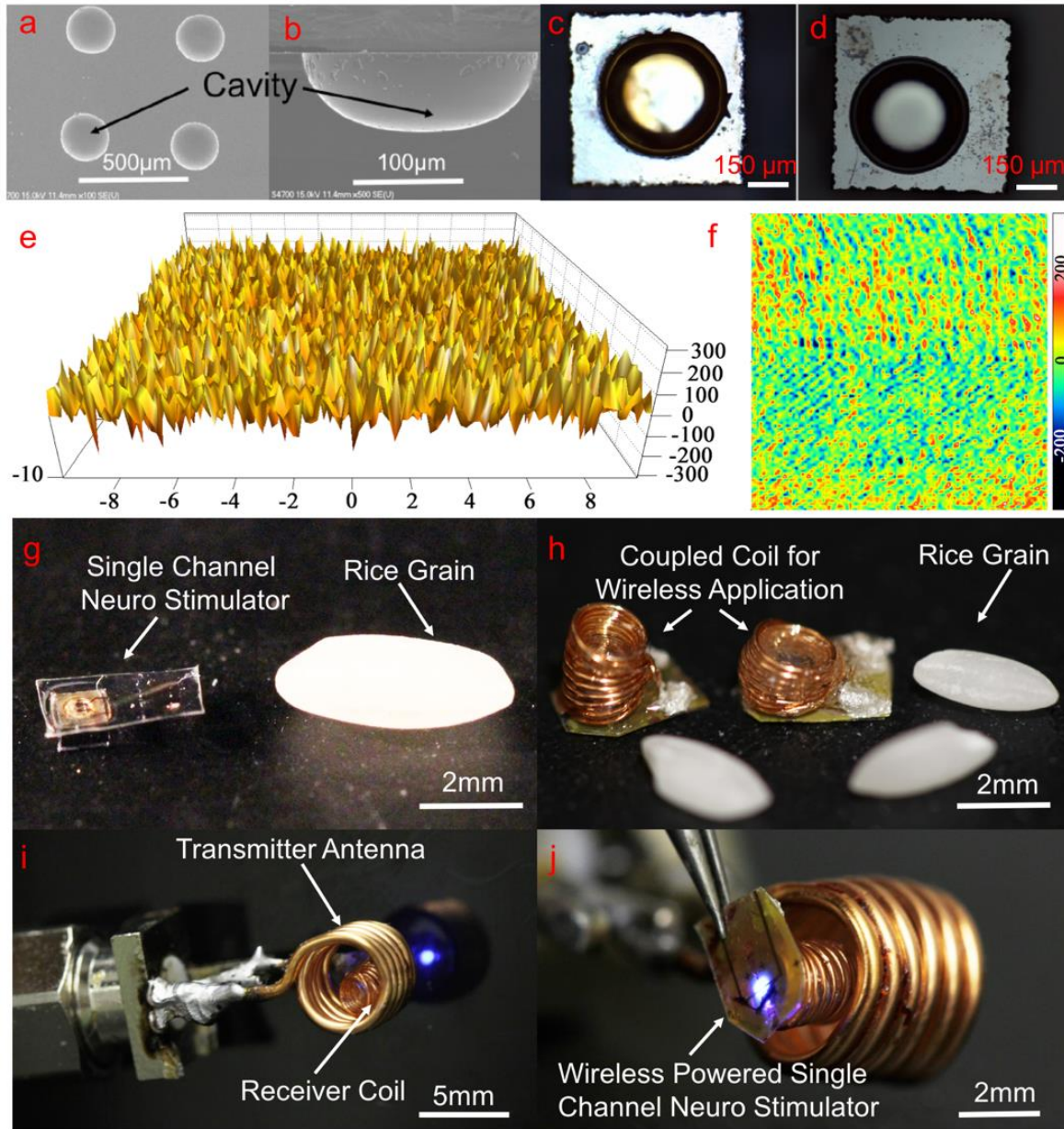
Figure 7-3. (a), (b) SEM images of the etched Si cavity. (c), (d) Post and prior Al coating of the cavity respectively. (e), (f) AFM images for quantitative analysis of cavity surface roughness (x axis units in μm, y axis in nm). (g) Fabricated single-channel opto neurostimulator. (h) Rx-coil coupled single-channel opto neurostimulators. (i), (j) An opto stimulator powered wirelessly by a Tx coil.

Coupling the LED to the micro-fabricated cavity reflector provides a significant boost in optical intensity, as seen in previous studies[155]. Figure 7-3(a, b) show the SEM images of a cavity array after isotropic Si etching and cross-section of a single cavity, respectively, where a smooth surface morphology was observed. AFM analysis in Figure 7-3(e) and (f) shows a small mean roughness (~72 nm) for the etched cavity, confirming the smooth morphology of the cavity resulted from the wet isotropic etching. This roughness, compared with the radius of the cavity (~100 µm), is supposed to create a negligible light scattering, thereby allowing the reflector to optimally enhance the intensity. Figure 7-3(I, j) shows a fabricated neurostimulator, and its activation through inductive powering on a benchtop setup.
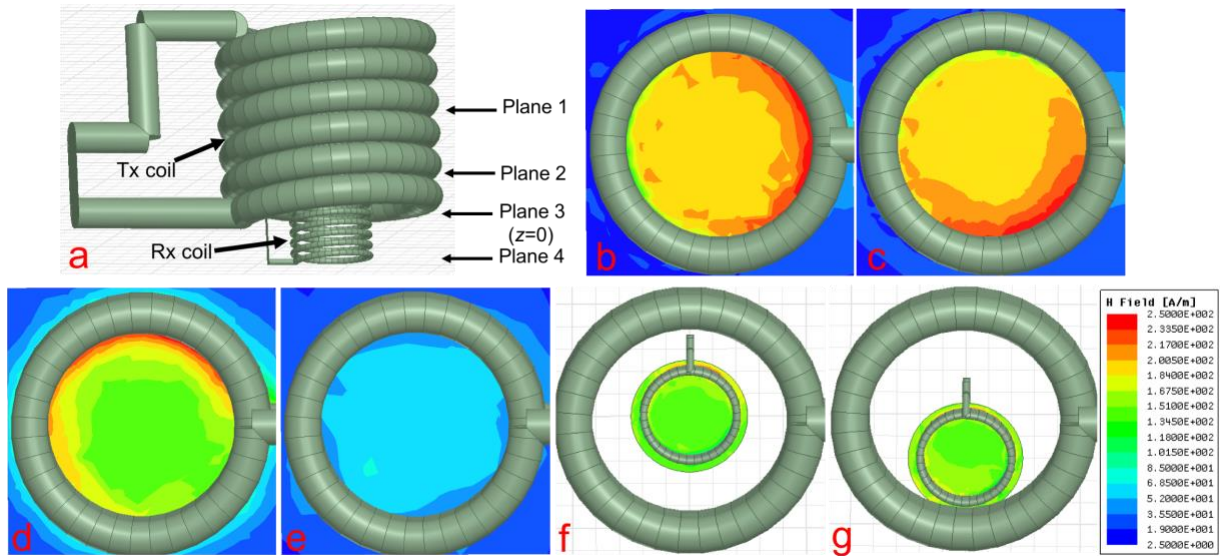
Figure 7-4. Simulation model for the inductive coupling at cross section planes. Plane 3 refers to the bottom plane of the Tx coil (z axis displacement, z=0), plane 1,2,4 refers to z=2.5mm, z=1mm and z=-1mm, respectively. (a) The simulation model in HFSS. Magnetic flux distributions for (b) plane 1 (c) plane 2 (d) plane 3 (e) plane 4. Induced magnetic flux by the Rx coil at plane 2, while the Rx is positioned at (f) Tx center (g) Tx periphery. Units of flux distributions provided in the color map legend.

7.1 Methods and materials

7.1.1 Finite element simulation

Electromagnetic properties of the inductive link between the Rx and Tx coils were also simulated using the finite element method (FEM) in High Frequency Structure Simulator software (HFSS-Ansys electromagnetics suite 17.2, Ansys). Figure 7-4 illustrates the HFSS device model of the two-coil telemetry link, and Table 7-1 provide a set of parameters used to design the Rx and Tx models for FEM simulation. In this study, the dimensions of the simulated Tx coil were similar to those of the fabrication coil. The inner and outer diameters of the Rx coils remained the same as the fabricated devices, while the number of turns was varied to study its effect on the resonant frequency and power transfer efficiency (PTE) of the inductive power link. The pitch between adjacent turns was estimated using the overall length of the solenoid coil and the diameter of the copper wire.

Table 7-1. Simulation parameters for two coil inductive couple link

	Wire radius (mm)	Coil radius (mm)	Pitch (mm)	# of turns
Tx	0.406	2.5	1	6
Rx	0.08	1.0	0.275	3,6,9,12,15

Magnetic flux distribution of the Tx coil was simulated as cross-sectional planes at the mid-point, bottom, and 1mm below the bottom plane of the Tx[156]. As shown in Figure 7-4 (d, d, e), a stronger magnetic flux is generated at the periphery of the Tx coil due to the asymmetrical winding of the Tx loops. Consequently, the inductively induced magnetic field in the Rx coil is stronger when the Rx coil is aligned to the periphery of the Tx coil, as shown in Figure 7-4 (f) and (g). In

addition, the magnetic flux is concentrated in the middle plane of the coil and the strength of the flux reduces significantly as the simulated plane approached towards the bottom of the coil, as indicated in Figure 7-4(b-e).

7.1.2 Equivalent circuit design
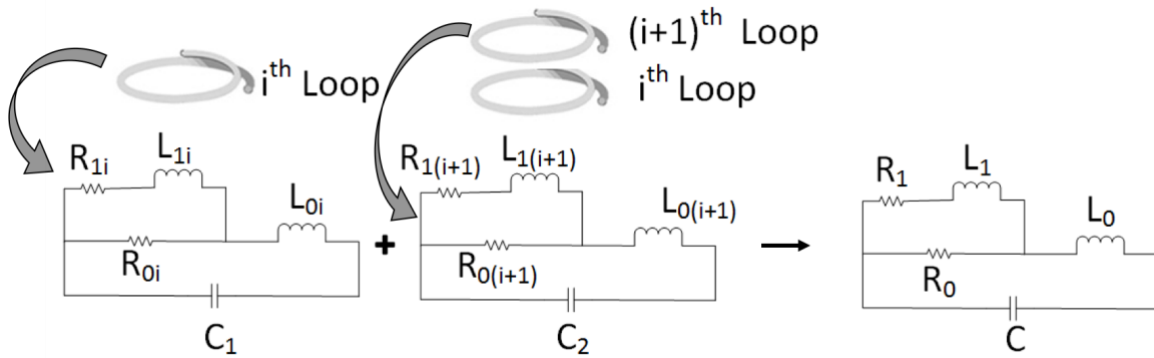
Figure 7-5. Equivalent circuit model for the Rx coil.

Distributed resistive effects from the finite resistivity of the conductor, along with inductive effects from the coiled copper conductor, and dielectric effects from the insulation around the conductor altogether constitute the electrical properties of the Rx coil. An approximation of the electrical characteristics due to the effects of these components is of great importance, as they determine the efficiency and effectiveness of the inductive link towards a successful operation of the whole setup. To facilitate the design of the micro-coil, we studied an equivalent circuit model of the Rx coil that provides an estimation of the distributed passive components. As shown in Figure 7-5, R_{0i} and L_{0i} are the DC resistance and self-inductance of the i-loop wire within a multi-loop coil, respectively. R_{1i} and L_{1i} are estimated to be in effect by the tendency of alternating current being distributed within the conductor, commonly known as the skin effect. The distributed circuit

model in Figure 7-5 can be simplified using a combined lump model, where R_0, R_1, L_0, and L_1 represents the lumped resistances and inductances responsible for the impedance change with frequency while considering the skin effect [157], and the capacitor C is the total effective capacitance across the coil. The self-inductance L_0 and the DC resistance R_0 could be calculated from the following equations:

$$L_0 = \frac{N^2 \mu A_c}{l_c} \dots\dots\dots\dots\dots\dots\dots\dots\dots\dots\dots\dots\dots Eqn\ (1)$$

$$R_0 = \frac{\rho D}{T} \dots\dots\dots\dots\dots\dots\dots\dots\dots\dots\dots\dots\dots Eqn\ (2)$$

where, N is the number of turns of the coil, μ the permeability of the core, Ac is the cross-sectional area of the coil, and lc is the length of the solenoid coil. While calculating the DC resistance, ρ is the resistivity of the conductor metal (in this work, copper), D being the total length of the coiled conductor wire and T is the cross-sectional area of the used conductor wire. The skin effect components, R_1 and L_1 could be represented by the following equations,

$$L_1 = \frac{L_0}{\alpha_L} \dots\dots\dots\dots\dots\dots\dots\dots\dots\dots \dots\dots\dots\dots Eqn\ (3)$$

$$R_1 = \alpha_R R_0 \dots\dots\dots\dots\dots\dots\dots\dots \dots\dots\dots\dots\dots Eqn\ (4)$$

where $\alpha_L = 0.315 \alpha_R$ and $\alpha_R = \frac{0.53 * wire\ radius}{\delta_{max}}$. The skin depth in conductors, δ_{max}, is represented

by $\delta_{max} = \sqrt{\frac{2}{\omega \mu \sigma}}$, where ω is the resonant frequency, μ is the magnetic permeability in vacuum, and σ is the conductivity of the conductor metal. The constant term 0.53 is derived from the following equation

$$C = \frac{r}{2r - \delta_{max}}$$

The impedance of the lumped equivalent circuit could be represented by the following equation:

$$Z = \frac{R_1R_0 - \omega^2 L_1L_0 + j\omega(R_1L_0 + R_0L_1 + R_0L_0)}{R_1 + R_0 + j\omega(L_1 + R_1R_0C - \omega^2 L_1L_0C) - \omega^2 C(R_1L_0 + R_0L_1 + R_0L_0)} \dots\dots\dots\dots\dots\dots\dots\dots\text{Eqn (5)}$$

Given the theoretical inductances and resistances that are derived from Eqn (1)-(4), the parasitic capacitance C of the coil can be estimated based on the measured impedance by curve fitting, as shown in Figure 7-7(b).

7.1.3 Device fabrication, assembly, and packaging

The fabrication of the flexible stimulator started by depositing 10 µm Parylene-C on a 3-inch Si wafer. Desired properties of an implant include biocompatibility, flexibility, and excellent optical transmission properties - all of which are present in Parylene-C as the substrate. A 500 nm copper (Cu) film on a 5 nm titanium (Ti) adhesion layer was deposited on the Parylene-C substrate using a thermal evaporator (Edward Auto306, Edwards). A photoresist mask (Shipley S1813, MICROCHEM Corp.) was patterned via ultraviolet (UV) lithography. After that, Cu and Ti thin films were deposited and patterned chemically using Cu etchant (Ferric Chloride by MG chemicals) and hydrofluoric acid (HF), respectively, to form the metal pads and traces for µLED and coil assembly. After removing the photoresist mask in acetone and rinsing the wafer in isopropyl alcohol (IPA) and deionized (DI) water, the metal patterns were encapsulated with 5 µm Parylene-C, followed by oxygen plasma etching of Parylene-C with 58 sccm O2 at 250W (PX-250, Nordson March) to create the contact vias on the µLED and coil bonding pads, using a photoresist mask. Commercially available blue µLEDs (TR2227tm, CREE Inc.) were manually aligned on the exposed metal contacts and bonded with low melting point (LMP) solder (melting point at ~ 62 °C, 144 ALLOY Field's Metal, Rotometals, Inc.).

The μ-reflector was fabricated in a separate step, initiated with thermal evaporation of 500 nm Cu on a 300-nm thick, commercial low-pressure chemical vapor deposited (LPCVD) nitride-on-silicon wafer (University wafers, Boston). Because of its low etching rate under SF_6 plasma [], Cu was used as a mask to pattern the LPCVD nitride with 20 sccm SF_6 at 250 W RF power for 45s. After nitride patterning, the Cu mask was removed using Cu etchant, followed by DI water rinse. The nitride masked Si wafer was then submerged in an HF and nitric acid (HNO3) (1:9 by volume) solution for 60 mins, which isotropically etches Si to form hemispherically shaped microcavities[140], [141]. After that, the nitride mask was removed using hot phosphoric acid (H3PO4) at 75 ºC and the wafer was rinsed with DI water. Finally, a 100 nm aluminum (Al) layer was deposited in the cavities using thermal evaporation to form a highly reflective surface for collecting the μLED backside emission and focusing the diverged light beams.

For device assembly, the wafer with the reflector array first was diced into 1 mm × 1 mm chips containing a cavity on each. Manual alignment and positioning were performed to couple the μLED substrate and the Al-coated cavity reflector under an optical microscope while bonding using a medical grade epoxy (Atom adhesives AABond- FDA2), and cured at room temperature (25 ºC) for 24 hrs. The Rx coil was later wound around the Si base of the reflector and electrically connected to the contact pads on the μLED substrate using conductive silver paste. Finally, the assembled device was completely encapsulated using Parylene-C.

7.2 Device characterization

7.2.1 Optical property measurement

The surface roughness of the Al-coated reflective layer was measured using a Surface Profilometer (NanoMap-500LS) as shown in Figure 7-3(e, f). The average surface roughness of the metal coated cavity was ~15 nm, indicating minimal scattering of the reflected light. The light intensity of the as-fabricated neuro stimulator penetrating through different thicknesses brain tissue was measured using a Newport 818-SL optical detector coupled with an OD3 attenuator and Newport 843-R series optical power meter, and data was compared with that of a bare μLED.

The brain tissue slices with thicknesses of 100-500 μm were prepared from fixed cortical tissues of rats. The animals were euthanized with an Intra-peritoneal injection of heparin followed by an overdose of pentobarbital sodium. Then, they were perfused transcardially with 4% paraformaldehyde in 0.1 M phosphate buffer (pH 7.4). Post perfusion, the brain was exposed and the head immersed in the same fixative at 4°C for at least 24 hrs then in phosphate-buffered saline (PBS). Finally, the brain tissues were cut into serial 100-500μm coronal sections using a Vibratome (Lancer).

7.2.2 Thermal property measurement

The temperature profile of the stimulator during continuous operation provides critical information to study the effect of trapped heat due to the silicon reflector, and also gives an insight on how tissue sections might be able to help in dissipation of the heat from the stimulator to surrounding medium. Hence, we measured the thermal energy distribution of the device while

stimulating over a 500 µm rat cortical tissue slice using a high resolution, thermal imaging camera (FLIR E6, FLIR® Systems, Inc). The temperature increase was quantified with respect to the ambient temperature (22ºC) and compared with that of a bare µLED.

7.2.3 Electromagnetic properties measurement

The electromagnetic properties of the Tx coil, Rx coil, and 2-coil inductive link were characterized using a microwave network analyzer (Keysight N5227A PNA, Keysight Technologies). The two-port S parameter (S21) for the 2 coil coupling link was measured to calculate the change in PTE with respect to the number of turns of the Rx coil. The resonance frequency of the coupling was also measured from the S parameter. The experimental results were compared with the simulated results. Furthermore, the impedance for the Rx coil was measured using an impedance analyzer (HP 4192, Hewlett Packard), and the obtained data was used to calculate the parasitic capacitance of the Rx coil based on Eqn (5). For all the measurements, the Tx coil had an inner diameter of 5 mm, outer diameter of 5.08 mm, and 6 turns.

7.3 In vivo experiment

7.3.1 Animal handling and viral transfection

Adult female Sprague Dawley rat (300-400 g) were used in all experiments. Rats were housed in the animal facility of the Michigan State University, USA under standard conditions at a constant temperature of 22 ºC supplied with food and water. Virus injection and device implantation were performed using sterile surgical protocols approved by the Institutional Animal Care and Use Committee (IACUC) at Michigan State University. All efforts were made to minimize the number

of animals used and prevent or ameliorate their suffering.

For virus injection, rats were fixed on a stereotaxic frame while anesthetized with 2-4% isoflurane and oxygen mixture. A 3~4 cm incision was made in the skin overlying the skull and small cavities were made bi-laterally on the skull to get access to the primary visual cortex (V1, lateral: 3.6 mm, anteroposterior: 6.3 mm relative to Bregma) using a precision surgical drill. Channelrhodopsin-2 expression was induced by administration of a viral solution of AAV-hSyn-hChR2 (H134R)-mcherry (10^{12}~10^{13} genome/mL). The process followed a 1 µL aliquot being delivered to each cavity by slow pressure injection from a Hamilton syringe. One (1) µL aliquot was delivered through two loads, with 0.5 µL per load followed by a 10 min wait after each load to allow sufficient diffusion of the virus to the surrounding tissues. After the syringe was retracted, the cortical cavity was filled with surgical wax and the craniotomy wound was sutured. Prior to suturing the skin, the cortex opening was covered with gel foam. The animals were given appropriate postoperative care (analgesic, fluids) and placed on the heat pad. The animals were returned to the facility and housed separately after recovery from anesthesia, and prevention of infection and relief from surgical discomfort was ensured by providing topical antibiotics and subcutaneous pain medication, respectively.

7.3.2 Device implantation and stimulation

For device implantation, two weeks' post-injection, the transfected rat was placed back onto the stereotaxic apparatus and underwent the anesthetic process mentioned previously. A unilateral craniotomy was performed by opening a small hole on top of both the right and left V1 lobes while the dura remained intact. A wireless neuro-stimulator was placed in the skull opening[158]. For

inductive power transmission, the Tx coil was aligned over the implant and driven by a function generator (AFG3102, Tektronix) with a sinusoidal voltage of 10 Vp-p and a resonant frequency <100 MHz. During the optical stimulation, one V1 lobe was stimulated continuously for 55 mins, while the other was considered as a control.

7.3.3 Perfusion, histology and fluorescent microscopy image analysis

After the stimulation, the rat was given a 75~90 min survival period. Upon completion of the experiments, animals were euthanized with pentobarbital sodium and then perfused transcardially with 4% paraformaldehyde fixative for histological studies. The brain tissue was post-fixed overnight at 4 °C in the same solution. Tissue sections (500 μm thickness) were cut in chilled 0.1 M phosphate buffer solution and were stored in 24-well tissue culture plates for post-immuno-histology chemical processing. The processed sections were later mounted on microscope glass slides while covering by coverslips with an anti-fade solution for c-Fos (an activity-dependent biomarker) expression. Microscope images were taken using a fluorescent microscope (Nikon MICROPHOT-FXA) to analyze the c-Fos and m-Cherry expressions.

7.4 Characterization and experiment results

7.4.1 Optical properties

The optical analysis illustrated in Figure 7-6(a) indicates the superior optical performance of the reflector-coupled stimulator. Figure 7-6(b) shows the captured intensity after the light passed through a 500 um tissue section. Our data indicates that although the intensity reduces heavily with introductions of thicker tissue sections, the threshold (1 mW/mm^2) for opsin activation[11] is

achieved even for a 500 μm thickness section, establishing an elementary yet efficient method for brain stimulation without tissue invasion. Figure 7-6(b) shows the intensity increase in percentage, where a reflector-coupled stimulator was compared with a bare stimulator. Light intensity, along with illumination depth significantly increases by over 60%, which was measured through 500-μm-thick tissue slices. This advantage makes our reflector-coupled stimulator a considerable competitor for deep brain stimulation, capable of optical stimulation from the cortical surface rather than brain tissue invasion[159].
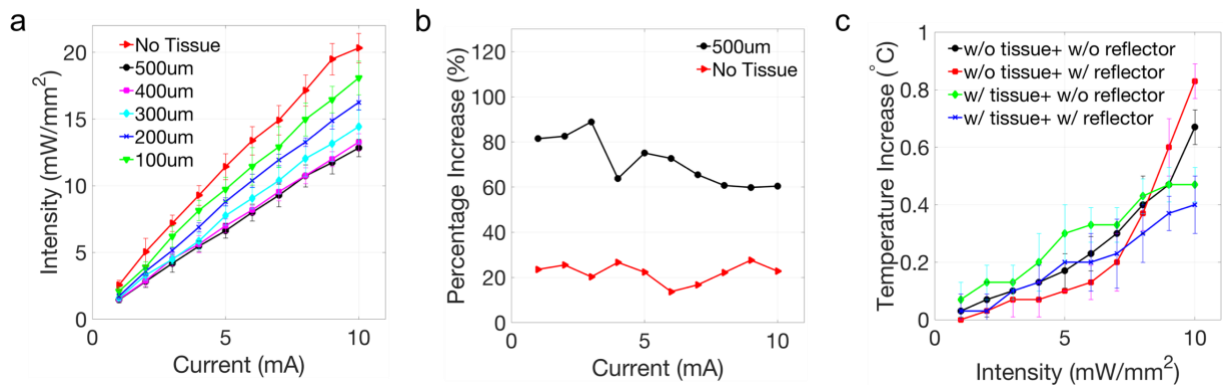
Figure 7-6. (a) Light penetration through tissue sections with a coupled reflector (n=5), (b) Intensity improvement of reflector coupled stimulator compared with a bare μ-LED (c) Change in temperature for devices stimulating through a 500 μm cortical tissue slice (n=3)

7.4.2 Thermal properties

The temperature increase of the reflector-coupled stimulator under different operating conditions is plotted in Figure 7-6(c), and compared to that of a bare μLED stimulator (i.e. without the integrated μ-reflector component). The addition of a reflector reduces the heat dissipation to the silicon substrate due to thermally insulating materials (i.e. polymer, epoxy, and air) in the reflective cavity, thereby resulting in higher temperature increases. Most importantly, the overall temperature rise of the reflector-coupled stimulators falls below 0.5°C, complying with the
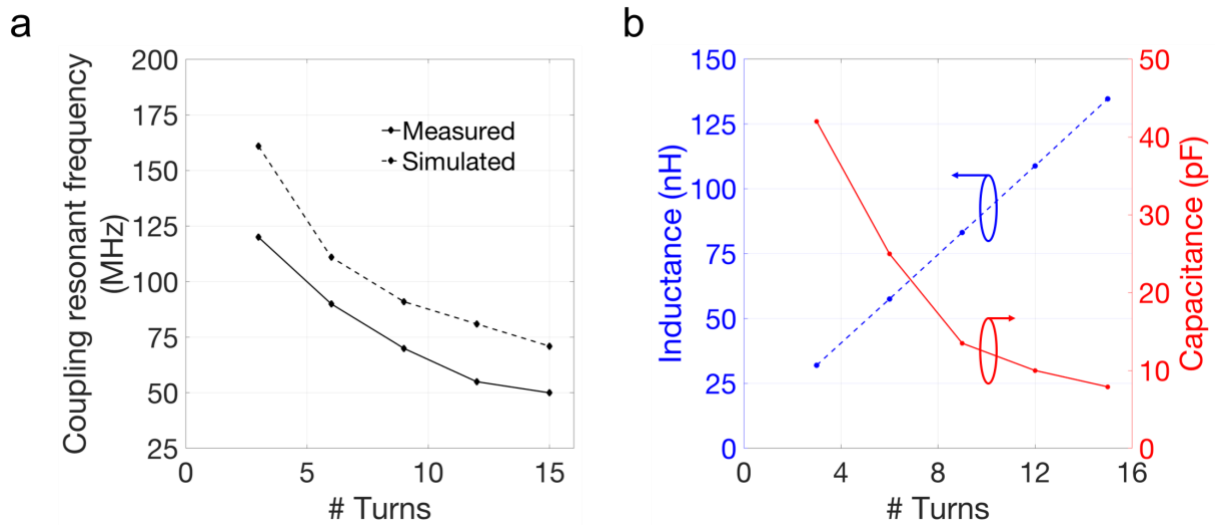
Figure 7-7. (a) Resonant frequency of the two coil inductive link with respect to the number of turns of the Rx coil. b) Inductance and parasitic capacitance of the Rx coil as functions of the number of turns, calculated using impedance fitting based on the analytical models.

American Association of Medical Instrumentations (ANSI/AAMI) standard limit of 2 ºC increase for

chronic biomedical implants for neuro-stimulators (ISO-14708-1).

7.4.3 Electromagnetic properties

Figure 7-7(a) shows the resonant frequency with respect to the number of turns of the Rx coil.

With an increase in the loops, the resonant frequency was found to be decreasing and for ≥ 9

turns, both our experiments and simulations provide a resonant frequency of < 100MHz. A low

resonant frequency is highly desirable to maintain nerve vitality, which effectively minimizes the

electromagnetic exposure to living tissues and reduce the risk of radiation[100]. The decrease in

resonant frequency is due to the increase in flux linkage that increases with the turns for the Rx.

However, increasing the turns or the coil length simultaneously increases the device dimensions

and thereby makes it challenging towards fabricating a fully implantable stimulator. It should be

noted that, for experimental purposes, the coils were manually constructed using a winding rod so the actual devices have a slight deviation in pitch and length than the simulation model, resulting in the difference in their resonant frequencies between the simulation and experimental conditions. Figure 7-7(b) shows the inductance calculated based on Eqn (1) and the capacitance derived from impedance fitting based on Eqn (5).

Figure 7-7(a) shows the measured and simulated PTE values with respect to the number of turns of the Rx coil. The measured PTE harmonizes with the simulated model, with a maximum efficiency of 12.82% for a 15 loop implant coil. It is also noted that, given the same Tx coil, the Rx coils with more turns have relatively higher PTE but larger dimensions. Considering the tradeoff between PTE and miniaturization of the implant, we utilized a 9-loop Rx coil in the first generation prototype for the following animal studies. Prior to animal studies, it is critical to understand the effects of the separation and misalignment of the coil link on the electromagnetic coupling performance and the optical properties of the optical stimulator. Therefore, we studied the optical intensity of the stimulation under various vertical and horizontal displacements between the Tx and Rx coils. As shown in Figure 7-7(b), the optical intensity is higher when the Rx coil of the stimulator is closer to the center region of the Tx coil, while the opsin activation threshold (>1 mW/mm2) is achieved at the separation of less than 0.8 mm from the bottom plane of the Tx coil. This phenomenon is supported by our simulation results as plotted in Figure 7-4, which demonstrates the gradual diminution of the magnetic flux from the Tx coil center/middle cross-sectional plane towards the bottom plane.

In addition, our results suggest better coupling and hence better optical intensity can be achieved when the Rx coil is intersecting with stronger magnetic fluxes generated by the Tx coil, preferably towards the periphery of the Tx coil. As illustrated in Figure 7-8(c), a stimulator with a 9-loop coil could achieve as high as 15% intensity enhancement if it is shifted to the periphery from the center of the Tx coil. Our experimental results could be qualitatively supported by the simulations from Figure 7-4, where a stronger magnetic flux is observed towards the perimeter of the Tx coil. This concentrated distribution of magnetic flux at the edge, however, becomes evenly allocated across the diameter, when displaced towards the bottom plane. Further improvement of the stimulator performance could be achieved in the future using a three-coil telemetry configuration[160], [161].
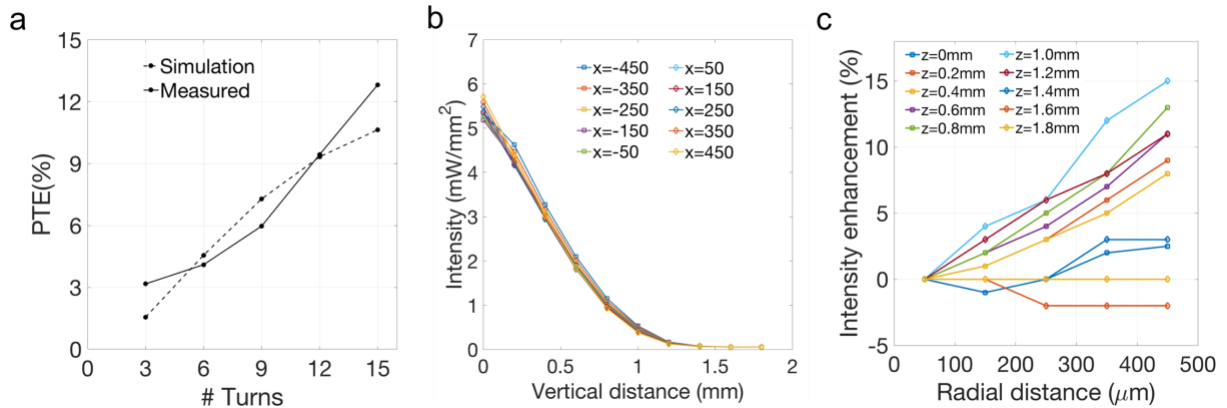
Figure 7-8. (a) PTE change with respect to the Rx coil turns (b) Optical intensity obtained from a 9-loop coiled stimulator under different vertical displacements of the coils. Symbol "x" in (µm) indicates the horizontal position of the Rx center compared with the Tx center, while vertical distance (mm) indicates the displacement from the bottom horizontal plane Rx, compared with the bottom plane of Tx. (h) Intensity enhancement of a 9-loop coiled stimulator under different horizontal displacements of the coils, Z or x-axis indicates Tx and Rx both on the same vertical axis and same horizontal plane.

7.5 In vivo results

In vivo experiments were performed on three (n=3) transfected rats following the protocols mentioned at the end of this chapter. Figure 7-9(a) shows a 9-loop coiled stimulator placed over one V1 lobe and coupled to a Tx coil. The other V1 lobe of the same animal was used as a control. Immunochemical analysis was performed on the post perfusion fixed brain tissue to identify the presence of mcherry and c-Fos biomarkers, in order to validate the efficacy of the cell transfection and optical stimulation, respectively. Existence of m-cherry expressed cells (in red) are visible, as seen in Figure 7-9(c, e). These figures demonstrates the effectiveness of our viral transfection process, for both the control and stimulated lobes on an experimental animal. Figure 7-9(d, f), on the other hand, provide the evidence of c-Fos (in green) expressed cells in both the control and stimulated lobes of the transfected animal. The stimulated V1 lobe in Figure 7-9(f) has more cells expressing c-Fos as compared to the control side in Figure 7-9(d), suggesting stronger neural activity induced by optical stimulation. It should be noted that due to the natural activity of the visual cortex, there will be a population of cells expressing c-Fos even at the absence of any stimulation, while a larger population of cells are expected to show c-Fos expression as a result of the optogenetic stimulation. To provide a robust evidence towards the efficacy of the optogenetic stimulation, we repeated the above optical stimulation on a naïve animal without virus transfection, and the cortical tissues were processed immuno-biologically using the above method to analyze the c-Fos expression of the stimulated lobe versus the non-stimulated lobe. As shown
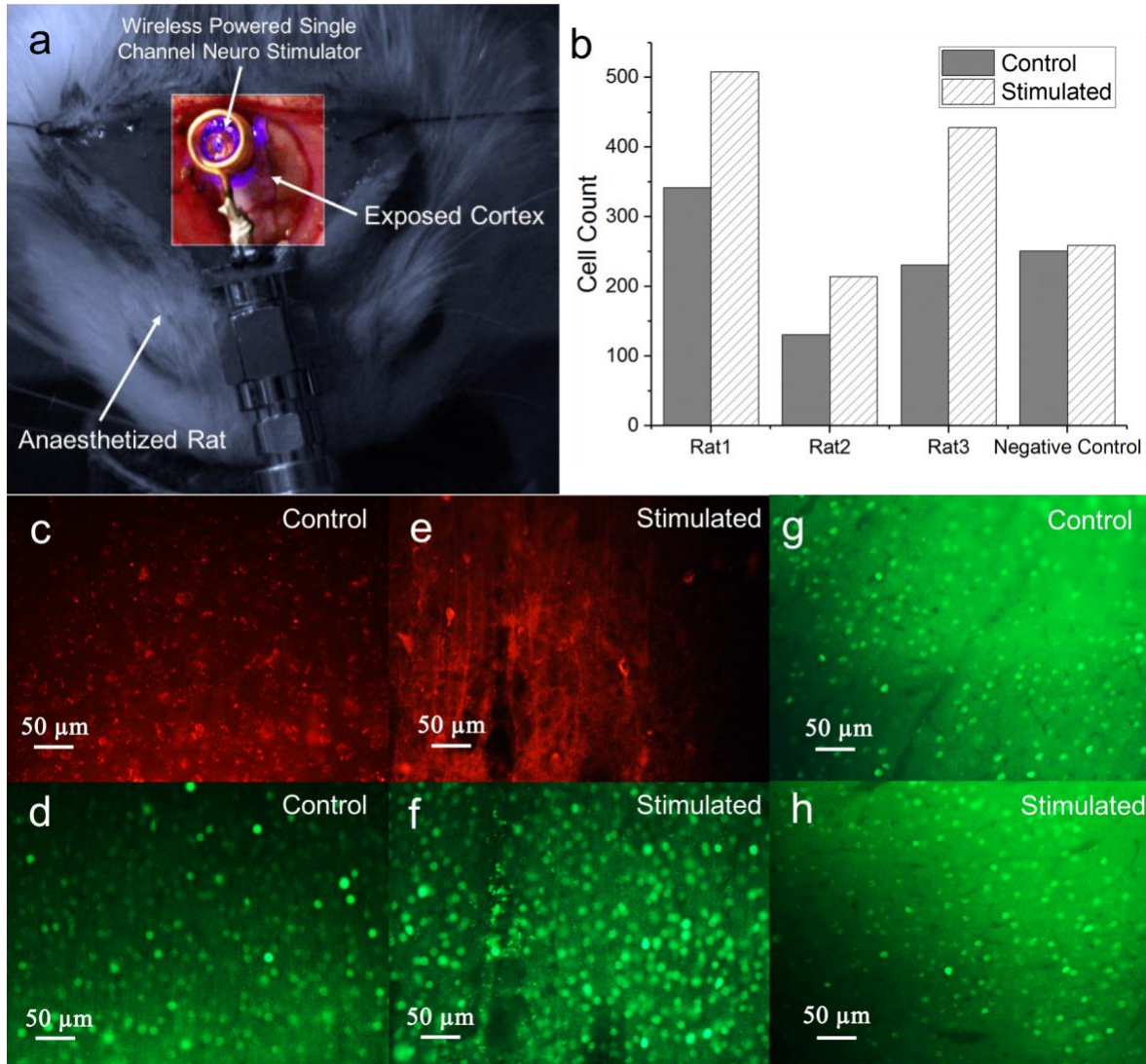
Figure 7-9. (a) In vivo stimulation using a wirelessly-powered neurostimulator on the V1 of an anaesthetized rat. (b) quantitative representation of c-Fos expressed cells using cell sorting. Fluorecent images of mCherry (c) and (e) as well as c-Fos (d) and (f) expressions of the control and stimulated cortices, respectively, obtained from the same cortical areas of the same transfected animal. (g) and (h) c-Fos expressions of the control and stimulated cortices, respectively, obtained from a non-transfected animal.

in Figure 7-9(g) and (h), there is no visible significant difference in the c-Fos expression between

the stimulated lobe and the non-stimulated control side. The presence of c-Fos expression in both

the simulated and non-stimulated lobes is attributed to the spontaneous neural activity in the

animal cortex. This result demonstrates that the elevated c-Fos expression in the virus transfected cortex is indeed induced by LED stimulation, eliminating the possibility of other interferences, such as heat or tissue injuries.

A quantitative measurement of the expressions, such as cell sorting, was performed based on the fluorescent images of the tissue sections. Using an in-house Matlab script, computer vision techniques allowing basic morphological operations along with watershed algorithm was utilized to define cell segmentation and an approximate count of cells expressing c-Fos. In concert with the qualitative data, Figure 7-9(b) indicates that the transfected cortices with optical stimulation show a significant increase in the cells expressing c-Fos, and this is consistent among the three subjects. There is a negligible difference in cell activity between control and stimulated cortices of a non-transfected naïve animal, supporting our claim of increased cell activity due to the applied stimulation.

Table 7-2 lists the specifications of some recent advances in the development of inductive link battery-free wireless optical neurostimulators and our work. The comparison shows a competitive advantage of our stimulator as a fully implantable biomedical neurostimulator with very lightweight, compact size (mm scale), and low operating frequency.

Table 7-2. Comparison of the proposed two coil inductively coupled concept and

neurostimulators reported by other groups

Work	Architecture	Substrate	Weight (mg)	Dimensions (mm)	Frequency	channels	Available intensity (mW/mm²)
Kim et al [68]	Discrete device	Flexible/rigid PCB	700	14x12.5x3	910MHz	4	17.7
Montgomery et al [72]	Discrete device	Rigid PCB	20-50	2x2x2	1.6 GHz	1	25.8
Shin et. al. [162]	Discrete device	Flexible PCB	30	10mm diameter, thickness<1.3mm	13.6 MHz	1,2	100
Aldaoud et al [163]	Discrete Device	Rigid PCB	1000	5x2.5x2.5	20, 13.4/15.6 MHz	1,2,16	_
Park et al.[164]	Discrete device	Rigid PCB	70	2.4x3.5x8.5	1.6-2.5 GHz	4	_
Park et al [165]	Discrete device	Stretchable Polymer	16	3.8x6x0.7	2.0-2.5 GHz	1	10
Lee et al [94]	LSI	Stacked rigid PCB	1600	12x7x11	2.4GHz	1	27
Our work	**Discrete Device**	**Flexible PCB**	**20**	**2.8x4.2x2.1**	**<100 MHz**	**1**	**5.8**

In this section, the author has proposed a design, fabrication method, and characterization of a reflector-coupled, wirelessly-powered single-channel optical neuro-stimulator with an mm-sized receiver coil for untethered optogenetic neuromodulation. The optical analysis shows that our reflector-coupled stimulator enables over 60% performance improvement when compared to a bare μ-LED stimulator, simultaneously surpassing the required effective optogenetic activation intensity threshold. The temperature increase of the stimulator is less than 2 ºC, well below the safety limit for biomedical implants. The performances of the two-coil telemetry link were studied using analytical circuit models, FEM simulation, and experimental approaches. Inductive coupling between the Tx and a prototype Rx coil was optimized at a <100 MHz carrier frequency, providing a convincing PTE while maintaining small geometries of the coils. The efficacy of optical neuro-stimulation was demonstrated by *in vivo* experiments on the visual cortex of an anesthetized rat, using qualitative and quantitative immunohistochemical analysis. The increased expression of activity-dependent biomarkers upon optical stimulation establishes a clear evidence of upregulated cell activity due to the optogenetic stimulation.

Chapter 8. Conclusion

Chronically implanted microscale wireless electronic sensors and actuators are emerging for a wide range of applications in humans and animals. One subset of interest to us are the sensors applied for light evoked neural activity for medical diagnostics or therapeutic purposes. In comparison to battery powered or wired stimulators, these wireless neural stimulators are advantageous in aspects such as less invasiveness, interfaces with better longevity towards central and peripheral nervous systems. Wires are a common mode for the failure indeed, and in addition, percutaneous wires are not immune to infection. Implanted wires, simultaneously limits the stimulator's ability to position itself with the tissue in consideration, eventually leading to create a foreign body response and contact area reduction of the target tissue. Particularly, in the wires in the peripheral devices could be subjected to chronic stress and strain, thereby leading to connection failure with the stimulator and jeopardizing the primary objective of the implant. The social behavior of the experimental subjects are of particular interest in some of the studies, where introduction of wires within the smaller animals like mice and rats has potential to interfere with the natural behavior of the animal when interacting with a group of animals.

This dissertation therefore have focused on the stimulator development process to eliminate these difficulties. However, primary challenge in the development process is to create efficient miniature devices for normal activity in animal and human patients, and ensure a reliable operation beneath skull, bone and tissues. Although these miniaturized devices, preferably at sub centimeter lengths could be fully implanted in the periphery and provide light weight to be implemented for unrestricted animal behavior; however efficient power delivery remains to be

the primary challenge for devices this small. To be considered as a method for power transfer, propagating electromagnetic waves requires antenna feature sizes to be comparable to the electromagnetic wavelength. Hence, when considering millimeter/sub-millimeter devices, such as the one described in this dissertation, effective power-transfer frequencies lie in the GHz range. For this electromagnetic wave range, the radiation is absorbed by the body of the subject, limiting the that needs to be safely transmitted to the implants in the deep tissue region. Typical solution is to concentrate on magnetic induction or batteries to power the implants; however, these approaches significantly affects the degree of miniaturization. Magnetic induction requires heavier and larger magnets to create the magnetic field while batteries increase the size of the device and add considerable weight. Battery replacement or recharge cycles are also problematic towards the potential goal of a long term reliable implant. Therefore, the concentration of this dissertation was directed to inductive coupling, as smaller and lighter miniaturized coils could be utilized to provide the necessary electromagnetic radiation required for powering the implants. However, the generated power for a receiving coil is directly related to the amount of captured flux by the area of the coils. Therefore, when the receiver coils are miniaturized, a reduction of output power is observed which in addition, is sensitive to angular placement between the transmitter and receiver and also to the perturbations in the distance. An effort have been established in this dissertation to optimize the power transfer while considering these challenges.

In addition, this dissertation discusses a fabrication process of an added optical element-a microscale reflector. Along with the fabrication process, the surface morphology of the as fabricated reflectors was characterized after the isotropic etching. The electrical, optical and

thermal characteristics of the fabricated neuro stimulators were quantified. The characterization data indicated that the proposed neuro stimulators provide enhanced optical intensity for lower applied power compared with the bare µ-LED array stimulators. The reflectors enhanced the intensity by at least 48% with a maximum of 65%. The opsin activation threshold was achieved at low current (~2mA) and low power consumption (<5mW). This low power requirement makes this 1st generation stimulator a promising candidate for further development towards a untethered interface.

To implement an untethered interface, a head-mounted battery powered bi-directional module have been proposed and developed, consisting of a 4 channel µ-LED array stimulator and a 2 channel recording electrode. The efficacy of the wireless signal receiving and data transmission using Bluetooth low energy was shown, as well as simultaneous data and real time representation of ECoG recordings on a GUI was demonstrated. Efficacy of the stimulation was validated through immuno-histology analysis and signal processing of the phase synchrony. It was found that application of higher current (10mA) provides a prominent phase lock synchrony of 200ms after stimulation while applying 5mA current generates a 150ms phase lock.

This dissertation demonstrates the analytical validation of optically induced opsin expression provided by the proposed stimulator by immunohistology analysis (c-Fos expression of neurons) performed on an anaesthetized rat. Our implemented stimulator could be wirelessly powered at lower frequency spectrum (<100MHz) with a transfer efficiency of 4%. A compact size (<25mm^3), lightweight (20mg) and low operating temperature increase (<1C) gives this stimulator a

competitive edge as a fully implantable bio-interface.

As mentioned previously, these miniaturized wireless devices are aimed to be applied as chronic implants towards medical and therapeutic diagnostic approaches. In addition, they serve as research tools for the biological studies in general. Notable to mention are their use in brain mapping, as the functions of brain neurons are yet to be well understood. Proper placement and implementation of these miniaturized devices could interpret the functions of different brain regions to neuroscientists. That said, it is worthy of mentioning that this dissertation discusses stimulators with an effective stimulation volume constituted by a collection of neurons, and the recorded electrical signals (ECoG) are also the collective signal from a group of neurons. An enhanced illustration of the neuron activity would be possible to achieve by utilizing single neuron stimulation and signal recording, which demands further development of these proposed devices.

Widely considered as light switches, the neurostimulators provide in vivo experimental approach for the developed light-gated proteins, and thereby allows better understanding from the cell biology or pharmacology point of view for the target neurons. Interesting studies such as stimulation using multiple optical wavelengths generated from one implant allows to understand the complex function of the neurons. Exciting one set of neuron by an excitatory protein (post stimulation), and inhibiting another set of neurons could extract more detailed information on the neuron activities as well as the structure of the neural circuitry. Understanding of the biological neural network allows further implementation of the artificial neural networks motivated by algorithms and mathematical derivations. Lack of a clear interpretation on the biological network

level could potentially create a bottleneck in the merger of these neural networks. The development of the neural stimulators, in conjunction with the development of light sensitive proteins could lead towards a complete understanding of the neural circuitry.

While a rapid expansion is being experienced in the development of neural stimulators, not only in the research or laboratory stage prototypes but also with many devices within the commercialization pipeline, however, this development process is expensive as well as time consuming. Due to their complex nature and the high risk they impose towards human patients, they are classified as class III implantable devices by the regulatory. Class III implants require a very rigorous regulatory approval process before clinical use. Proper and conclusive preclinical studies could play a vital role in this approval process. Designing towards a safe neural stimulator followed by in vitro, in vivo (animal) and or ex vivo (e.g. human cadaver) studies accompanied by a suite of preclinical evaluation can demonstrate device safety.

For a successful demonstration of neural stimulator, from prototype to commercialization, significant effort should be directed towards both device design and its preclinical evaluation to increase the implant lifetime and reduce associated cost when considering a new device. A successful demonstration of a miniaturized neural stimulator is achieved through close collaboration between many disciplines including engineers, scientists and the surgical/clinical team.

Some key components of any preclinical evaluation could include in vitro studies to determine materials suitability and device reliability, might also focus on accelerated testing under highly controlled environments; while in vivo experiments could use appropriate animal models of the disease or injury in order to assess safety and, if feasible, the efficacy of the technology. In this dissertation, the author have taken an effort to implement the above mentioned preclinical studies and have attempted to come to a conclusion based on the findings of the experiments. Although not within scope of this dissertation, human cadaver studies designed to ensure the device's form factor could unfold important information conforming to human anatomy, optimize the surgical approach and to develop any specialty surgical tooling.

Future investigations could be executed on the in vitro assessment of materials for biological cell–stimulator surface interactions, glial scarring and cytotoxicity of the stimulators discussed in this dissertation. Further In vitro analysis using accelerated aging techniques, including elevated temperatures, harsh electrolyte environments and accelerated mechanical testing, would provide a quantitative guideline towards the implant lifetime, also would assist in the material screening for hermetic encapsulation. Small animal models have been utilized throughout the studies for this dissertation, that do establish the in vivo efficacy however are not considered suitable for the long-term evaluation of device safety or for human surgical approach. Appropriate large animal models would be a better reflection of the anatomy, define a more accurate surgical approach and the bio-mechanical environment towards a clinical trial of a neural stimulator.

APPENDIX

MATLAB code for image processing:

```
clc
close all

A = imread('image_name.tif');

figure (1)
imshow(A)

I = rgb2gray(A); %convert the image to grayscale:

I = adapthisteq(I); % local contrast adjustments to extract the dimmer cells

I = imclearborder(I); % To eliminate the objects on the borders. This border objects might be
caused by noise/artifacts.

I = wiener2(I, [20 20]); %Noise removal by adaptive filtering, using a small window (in this case
20x20 pixels). Although barely noticeable to human eye, this step allows to reduce the number of
incorrect cells.

bw = im2bw(I, graythresh(I)); %The first step to extract the perimeters of cell or cell groups
following a binarization technique. These set of morphological operations allow further removal
of objects that are too small to be cells.

bw2 = imfill(bw,'holes'); %Step to fill the image regions and holes. This helps when the cells have
varying contrast within themselves.

bw3 = imopen(bw2, strel('disk',2)); %Step to perform morphological opening using a disc kernel:

bw4 = bwareaopen(bw3, 100); %Step to remove all connected components (cells) that have fewer
than 100 pixels. This is the performance limiting step to identify the size of cells. In my case, I
restricted my cell sizes to 100 pixels to clearly identify the activated neurons.

bw4_perim = bwperim(bw4); %Many cells would be grouped. An overlay of this step with the
grayscale image allows to visualize the grouped cells. The image overlay function is implemented
in the next step.

overlay1 = imoverlay(I, bw4_perim, [1 .3 .3]);

%The watershed algorithm helps to partially divide the groups into distinct cells. The watershed
algorithm interprets the gray level of pixels as a threshold. It is needed to modify the image for the
cell borders to have the highest intensity and to have the background clearly marked. The process
would be to find the maxima which would approximately correspond to the cell center.
```

```matlab
% Discover putative cell centroids
maxs = imextendedmax(I,  5);
maxs = imclose(maxs, strel('disk',3));
maxs = imfill(maxs, 'holes');
maxs = bwareaopen(maxs, 2);
overlay2 = imoverlay(I, bw4_perim | maxs, [1 .3 .3]);

% Modify the image so that the background pixels and the extended maxima pixels are prominent
in the image.
Jc = imcomplement(I);
I_mod = imimposemin(Jc, ~bw4 | maxs);


%Applying the watershed algorithm:

L = watershed(I_mod, 8);
labeledImage = label2rgb(L);


%Counting the number of discovered cells.

[L, num] = bwlabel(L);
```

%Overlay of the detected cells over the original grayscale image to visually evaluate the
performance of the algorithm:

```matlab
mask = im2bw(L, 1);
overlay3 = imoverlay(I, mask, [1 .3 .3]);

overlay4 = imoverlay(A, mask, [1 .3 .3]);

figure (2)
imshow(overlay4)
```

BIBLIOGRAPHY

BIBLIOGRAPHY

[1]   K. Deisseroth, "Optogenetics," *Nat. Methods*, vol. 8, no. 1, pp. 26–29, Jan. 2011, doi: 10.1038/nmeth.f.324.

[2]   L. Grosenick, J. H. Marshel, and K. Deisseroth, "Closed-Loop and Activity-Guided Optogenetic Control," *Neuron*, vol. 86, no. 1, pp. 106–139, Apr. 2015, doi: 10.1016/j.neuron.2015.03.034.

[3]   K. Deisseroth, G. Feng, A. K. Majewska, G. Miesenböck, A. Ting, and M. J. Schnitzer, "Next-Generation Optical Technologies for Illuminating Genetically Targeted Brain Circuits," *J. Neurosci.*, vol. 26, no. 41, pp. 10380–10386, Oct. 2006, doi: 10.1523/JNEUROSCI.3863-06.2006.

[4]   D. H. Lim, J. LeDue, M. H. Mohajerani, M. P. Vanni, and T. H. Murphy, "Optogenetic approaches for functional mouse brain mapping," *Front. Neurosci.*, vol. 7, 2013, doi: 10.3389/fnins.2013.00054.

[5]   R. C. Wykes *et al.*, "Optogenetic and Potassium Channel Gene Therapy in a Rodent Model of Focal Neocortical Epilepsy," *Sci. Transl. Med.*, vol. 4, no. 161, pp. 161ra152-161ra152, Nov. 2012, doi: 10.1126/scitranslmed.3004190.

[6]   G. Aston-Jones and K. Deisseroth, "Recent advances in optogenetics and pharmacogenetics," *Brain Res.*, vol. 1511, no. Supplement C, pp. 1–5, May 2013, doi: 10.1016/j.brainres.2013.01.026.

[7]   J. A. Steinbeck *et al.*, "Optogenetics enables functional analysis of human embryonic stem cell–derived grafts in a Parkinson's disease model," *Nat. Biotechnol.*, vol. 33, no. 2, pp. 204–209, Jan. 2015, doi: 10.1038/nbt.3124.

[8]   K. M. Tye and K. Deisseroth, "Optogenetic investigation of neural circuits underlying brain disease in animal models," *Nat. Rev. Neurosci. Lond.*, vol. 13, no. 4, pp. 251–66, Apr. 2012, doi: http://dx.doi.org.proxy1.cl.msu.edu/10.1038/nrn3171.

[9]   T. H. Lindsay, T. R. Thiele, and S. R. Lockery, "Optogenetic analysis of synaptic transmission in the central nervous system of the nematode Caenorhabditis elegans," *Nat. Commun.*, vol. 2, p. 306, May 2011, doi: 10.1038/ncomms1304.

[10]   D. C. Klorig and D. W. Godwin, "A magnetic rotary optical fiber connector for optogenetic experiments in freely moving animals," *J. Neurosci. Methods*, vol. 227, pp. 132–139, 2014.

[11] A. M. Aravanis *et al.*, "An optical neural interface: in vivo control of rodent motor cortex with integrated fiberoptic and optogenetic technology," *J. Neural Eng.*, vol. 4, no. 3, p. S143, 2007, doi: 10.1088/1741-2560/4/3/S02.

[12] K. Deisseroth, "Optogenetics: 10 years of microbial opsins in neuroscience," *Nat. Neurosci.*, vol. 18, no. 9, pp. 1213–1225, Aug. 2015, doi: 10.1038/nn.4091.

[13] F. Zhang *et al.*, "The Microbial Opsin Family of Optogenetic Tools," *Cell*, vol. 147, no. 7, pp. 1446–1457, Dec. 2011, doi: 10.1016/j.cell.2011.12.004.

[14] G. Nagel *et al.*, "Channelrhodopsin-2, a directly light-gated cation-selective membrane channel," *Proc. Natl. Acad. Sci.*, vol. 100, no. 24, pp. 13940–13945, Nov. 2003, doi: 10.1073/pnas.1936192100.

[15] E. S. Boyden, F. Zhang, E. Bamberg, G. Nagel, and K. Deisseroth, "Millisecond-timescale, genetically targeted optical control of neural activity," *Nat. Neurosci. N. Y.*, vol. 8, no. 9, pp. 1263–8, Sep. 2005, doi: http://dx.doi.org.proxy1.cl.msu.edu/10.1038/nn1525.

[16] E. Stark, T. Koos, and G. Buzsáki, "Diode probes for spatiotemporal optical control of multiple neurons in freely moving animals," *J. Neurophysiol.*, vol. 108, no. 1, pp. 349–363, Jul. 2012, doi: 10.1152/jn.00153.2012.

[17] J. A. Cardin *et al.*, "Targeted optogenetic stimulation and recording of neurons *in vivo* using cell-type-specific expression of Channelrhodopsin-2," *Nat. Protoc.*, vol. 5, no. 2, p. 247, Feb. 2010, doi: 10.1038/nprot.2009.228.

[18] V. Gradinaru, K. R. Thompson, and K. Deisseroth, "eNpHR: a Natronomonas halorhodopsin enhanced for optogenetic applications," *Brain Cell Biol.*, vol. 36, no. 1–4, pp. 129–139, Aug. 2008, doi: 10.1007/s11068-008-9027-6.

[19] B. Y. Chow *et al.*, "High-Performance Genetically Targetable Optical Neural Silencing via Light-Driven Proton Pumps," *Nature*, vol. 463, no. 7277, pp. 98–102, Jan. 2010, doi: 10.1038/nature08652.

[20] D. Oesterhelt and W. Stoeckenius, "Rhodopsin-like Protein from the Purple Membrane of *Halobacterium halobium*," *Nature. New Biol.*, vol. 233, no. 39, p. 149, Sep. 1971, doi: 10.1038/newbio233149a0.

[21] A. R. Adamantidis, F. Zhang, A. M. Aravanis, K. Deisseroth, and L. de Lecea, "Neural substrates of awakening probed with optogenetic control of hypocretin neurons," *Nature*, vol. 450, no. 7168, p. 420, Nov. 2007, doi: 10.1038/nature06310.

[22] V. Gradinaru *et al.*, "Targeting and readout strategies for fast optical neural control in vitro and in vivo," *J. Neurosci.*, vol. 27, no. 52, pp. 14231–14238, 2007.

[23] X. Han, "In Vivo Application of Optogenetics for Neural Circuit Analysis," *ACS Chem. Neurosci.*, vol. 3, no. 8, pp. 577–584, Aug. 2012, doi: 10.1021/cn300065j.

[24] L. Buchen, "Neuroscience: Illuminating the brain," *Nat. News*, vol. 465, no. 7294, pp. 26–28, May 2010, doi: 10.1038/465026a.

[25] E. E. Steinberg, D. J. Christoffel, K. Deisseroth, and R. C. Malenka, "Illuminating circuitry relevant to psychiatric disorders with optogenetics," *Curr. Opin. Neurobiol.*, vol. 30, no. Supplement C, pp. 9–16, Feb. 2015, doi: 10.1016/j.conb.2014.08.004.

[26] D. A. McCormick and D. Contreras, "On The Cellular and Network Bases of Epileptic Seizures," *Annu. Rev. Physiol.*, vol. 63, no. 1, pp. 815–846, 2001, doi: 10.1146/annurev.physiol.63.1.815.

[27] E. Krook-Magnuson, C. Armstrong, M. Oijala, and I. Soltesz, "On-demand optogenetic control of spontaneous seizures in temporal lobe epilepsy," *Nat. Commun.*, vol. 4, p. 1376, Jan. 2013, doi: 10.1038/ncomms2376.

[28] M. Ledri *et al.*, "Altered profile of basket cell afferent synapses in hyper-excitable dentate gyrus revealed by optogenetic and two-pathway stimulations," *Eur. J. Neurosci.*, vol. 36, no. 1, pp. 1971–1983, Jul. 2012, doi: 10.1111/j.1460-9568.2012.08080.x.

[29] J. T. Paz *et al.*, "Closed-loop optogenetic control of thalamus as a tool for interrupting seizures after cortical injury," *Nat. Neurosci.*, vol. 16, no. 1, p. 64, Jan. 2013, doi: 10.1038/nn.3269.

[30] A. V. Kravitz *et al.*, "Regulation of parkinsonian motor behaviours by optogenetic control of basal ganglia circuitry," *Nature*, vol. 466, no. 7306, p. 622, Jul. 2010, doi: 10.1038/nature09159.

[31] V. Gradinaru, M. Mogri, K. R. Thompson, J. M. Henderson, and K. Deisseroth, "Optical Deconstruction of Parkinsonian Neural Circuitry," *Science*, vol. 324, no. 5925, pp. 354–359, Apr. 2009, doi: 10.1126/science.1167093.

[32] P. L. Gildenberg, "History of Electrical Neuromodulation for Chronic Pain," *Pain Med.*, vol. 7, no. suppl_1, pp. S7–S13, May 2006, doi: 10.1111/j.1526-4637.2006.00118.x.

[33] J. Wang *et al.*, "Integrated device for combined optical neuromodulation and electrical recording for chronic in vivo applications," *J. Neural Eng.*, vol. 9, no. 1, p. 016001, 2012, doi: 10.1088/1741-2560/9/1/016001.

[34] L. Petreanu, D. Huber, A. Sobczyk, and K. Svoboda, "Channelrhodopsin-2–assisted circuit mapping of long-range callosal projections," *Nat. Neurosci.*, vol. 10, no. 5, p. 663, May 2007, doi: 10.1038/nn1891.

[35] F. Zhang, L.-P. Wang, E. S. Boyden, and K. Deisseroth, "Channelrhodopsin-2 and optical control of excitable cells," *Nat. Methods*, vol. 3, no. 10, p. 785, Oct. 2006, doi: 10.1038/nmeth936.

[36] H. Wang *et al.*, "High-speed mapping of synaptic connectivity using photostimulation in Channelrhodopsin-2 transgenic mice," *Proc. Natl. Acad. Sci.*, vol. 104, no. 19, pp. 8143–8148, May 2007, doi: 10.1073/pnas.0700384104.

[37] B. R. Arenkiel *et al.*, "In Vivo Light-Induced Activation of Neural Circuitry in Transgenic Mice Expressing Channelrhodopsin-2," *Neuron*, vol. 54, no. 2, pp. 205–218, Apr. 2007, doi: 10.1016/j.neuron.2007.03.005.

[38] W. Yang, W. Khan, J. Wu, and W. Li, "Single-channel opto-neurostimulators: a review," *J. Micromechanics Microengineering*, vol. 29, no. 4, p. 043001, 2019.

[39] O. Yizhar, L. E. Fenno, T. J. Davidson, M. Mogri, and K. Deisseroth, "Optogenetics in Neural Systems," *Neuron*, vol. 71, no. 1, pp. 9–34, Jul. 2011, doi: 10.1016/j.neuron.2011.06.004.

[40] Z. Jia *et al.*, "Stimulating Cardiac Muscle by Light: Cardiac Optogenetics by Cell Delivery," *Circ. Arrhythm. Electrophysiol.*, p. CIRCEP.111.964247, Jan. 2011, doi: 10.1161/CIRCEP.111.964247.

[41] F. Zhang *et al.*, "Optogenetic interrogation of neural circuits: technology for probing mammalian brain structures," *Nat. Protoc.*, vol. 5, no. 3, pp. 439–456, Mar. 2010, doi: 10.1038/nprot.2009.226.

[42] F. Zhang, A. M. Aravanis, A. Adamantidis, L. de Lecea, and K. Deisseroth, "Circuit-breakers: optical technologies for probing neural signals and systems," *Nat. Rev. Neurosci.*, vol. 8, no. 8, p. 577, Aug. 2007, doi: 10.1038/nrn2192.

[43] J. G. Bernstein and E. S. Boyden, "Optogenetic tools for analyzing the neural circuits of behavior," *Trends Cogn. Sci.*, vol. 15, no. 12, pp. 592–600, Dec. 2011, doi: 10.1016/j.tics.2011.10.003.

[44] O. G. S. Ayling, T. C. Harrison, J. D. Boyd, A. Goroshkov, and T. H. Murphy, "Automated light-based mapping of motor cortex by photoactivation of channelrhodopsin-2 transgenic mice," *Nat. Methods*, vol. 6, no. 3, p. 219, Mar. 2009, doi: 10.1038/nmeth.1303.

[45] L. Roux, E. Stark, L. Sjulson, and G. Buzsáki, "In vivo optogenetic identification and manipulation of GABAergic interneuron subtypes," *Curr. Opin. Neurobiol.*, vol. 26, no. Supplement C, pp. 88–95, Jun. 2014, doi: 10.1016/j.conb.2013.12.013.

[46] F. Pisanello *et al.*, "Multipoint-Emitting Optical Fibers for Spatially Addressable In Vivo Optogenetics," *Neuron*, vol. 82, no. 6, pp. 1245–1254, Jun. 2014, doi: 10.1016/j.neuron.2014.04.041.

[47] L. Campagnola, H. Wang, and M. J. Zylka, "Fiber-coupled light-emitting diode for localized photostimulation of neurons expressing channelrhodopsin-2," *J. Neurosci. Methods*, vol. 169, no. 1, pp. 27–33, Mar. 2008, doi: 10.1016/j.jneumeth.2007.11.012.

[48] Y. Iwai, S. Honda, H. Ozeki, M. Hashimoto, and H. Hirase, "A simple head-mountable LED device for chronic stimulation of optogenetic molecules in freely moving mice," *Neurosci. Res.*, vol. 70, no. 1, pp. 124–127, May 2011, doi: 10.1016/j.neures.2011.01.007.

[49] U. Nussinovitch and L. Gepstein, "Optogenetics for *in vivo* cardiac pacing and resynchronization therapies," *Nat. Biotechnol.*, vol. 33, no. 7, p. 750, Jul. 2015, doi: 10.1038/nbt.3268.

[50] O. J. Abilez, "Cardiac optogenetics," in *2012 Annual International Conference of the IEEE Engineering in Medicine and Biology Society*, 2012, pp. 1386–1389, doi: 10.1109/EMBC.2012.6346197.

[51] A. B. Arrenberg, D. Y. R. Stainier, H. Baier, and J. Huisken, "Optogenetic Control of Cardiac Function," *Science*, vol. 330, no. 6006, pp. 971–974, Nov. 2010, doi: 10.1126/science.1195929.

[52] T. D. Y. Kozai and A. L. Vazquez, "Photoelectric artefact from optogenetics and imaging on microelectrodes and bioelectronics: new challenges and opportunities," *J. Mater. Chem. B*, vol. 3, no. 25, pp. 4965–4978, 2015, doi: 10.1039/C5TB00108K.

[53] A. V. Kravitz and A. C. Kreitzer, "Optogenetic manipulation of neural circuitry in vivo," *Curr. Opin. Neurobiol.*, vol. 21, no. 3, pp. 433–439, Jun. 2011, doi: 10.1016/j.conb.2011.02.010.

[54] S. Dufour and Y. D. Koninck, "Optrodes for combined optogenetics and electrophysiology in live animals," *Neurophotonics*, vol. 2, no. 3, p. 031205, Jul. 2015, doi: 10.1117/1.NPh.2.3.031205.

[55] J. Zhang *et al.*, "Integrated device for optical stimulation and spatiotemporal electrical recording of neural activity in light-sensitized brain tissue," *J. Neural Eng.*, vol. 6, no. 5, p. 055007, 2009, doi: 10.1088/1741-2560/6/5/055007.

[56] T. V. F. Abaya, S. Blair, P. Tathireddy, L. Rieth, and F. Solzbacher, "A 3D glass optrode array for optical neural stimulation," *Biomed. Opt. Express*, vol. 3, no. 12, pp. 3087–3104, Dec. 2012, doi: 10.1364/BOE.3.003087.

[57]   J. Zhang *et al.*, "A microelectrode array incorporating an optical waveguide device for stimulation and spatiotemporal electrical recording of neural activity," in *2009 Annual International Conference of the IEEE Engineering in Medicine and Biology Society*, 2009, pp. 2046–2049, doi: 10.1109/IEMBS.2009.5333947.

[58]   J. Wang *et al.*, "Approaches to optical neuromodulation from rodents to non-human primates by integrated optoelectronic devices," in *2011 Annual International Conference of the IEEE Engineering in Medicine and Biology Society*, 2011, pp. 7525–7528, doi: 10.1109/IEMBS.2011.6091855.

[59]   S. Dufour *et al.*, "A Multimodal Micro-Optrode Combining Field and Single Unit Recording, Multispectral Detection and Photolabeling Capabilities," *PLOS ONE*, vol. 8, no. 2, p. e57703, Feb. 2013, doi: 10.1371/journal.pone.0057703.

[60]   B. Fan and W. Li, "Miniaturized optogenetic neural implants: a review," *Lab. Chip*, vol. 15, no. 19, pp. 3838–3855, 2015, doi: 10.1039/C5LC00588D.

[61]   Z. Fekete, "Recent advances in silicon-based neural microelectrodes and microsystems: a review," *Sens. Actuators B Chem.*, vol. 215, no. Supplement C, pp. 300–315, Aug. 2015, doi: 10.1016/j.snb.2015.03.055.

[62]   F. Wu *et al.*, "An implantable neural probe with monolithically integrated dielectric waveguide and recording electrodes for optogenetics applications," *J. Neural Eng.*, vol. 10, no. 5, p. 056012, 2013, doi: 10.1088/1741-2560/10/5/056012.

[63]   M. Schwaerzle, K. Seidl, U. T. Schwarz, O. Paul, and P. Ruther, "Ultracompact optrode with integrated laser diode chips and SU-8 waveguides for optogenetic applications," in *2013 IEEE 26th International Conference on Micro Electro Mechanical Systems (MEMS)*, 2013, pp. 1029–1032, doi: 10.1109/MEMSYS.2013.6474424.

[64]   K. Y. Kwon, B. Sirowatka, A. Weber, and W. Li, "Opto- #x03BC;ECoG Array: A Hybrid Neural Interface With Transparent #x03BC;ECoG Electrode Array and Integrated LEDs for Optogenetics," *IEEE Trans. Biomed. Circuits Syst.*, vol. 7, no. 5, pp. 593–600, Oct. 2013, doi: 10.1109/TBCAS.2013.2282318.

[65]   B. Rubehn, S. B. E. Wolff, P. Tovote, M. Schuettler, A. Lüthi, and T. Stieglitz, "Polymer-based shaft microelectrodes with optical and fluidic capabilities as a tool for optogenetics," in *2011 Annual International Conference of the IEEE Engineering in Medicine and Biology Society*, 2011, pp. 2969–2972, doi: 10.1109/IEMBS.2011.6090815.

[66]   Y. Son *et al.*, "A new monolithically integrated multi-functional MEMS neural probe for optical stimulation and drug delivery," in *2015 28th IEEE International Conference on Micro Electro Mechanical Systems (MEMS)*, 2015, pp. 158–161, doi: 10.1109/MEMSYS.2015.7050910.

[67]   D. R. Sparta, A. M. Stamatakis, J. L. Phillips, N. Hovelsø, R. van Zessen, and G. D. Stuber, "Construction of implantable optical fibers for long-term optogenetic manipulation of neural circuits," *Nat. Protoc.*, vol. 7, no. 1, p. 12, Jan. 2012, doi: 10.1038/nprot.2011.413.

[68]   T. -i. Kim *et al.*, "Injectable, Cellular-Scale Optoelectronics with Applications for Wireless Optogenetics," *Science*, vol. 340, no. 6129, pp. 211–216, Apr. 2013, doi: 10.1126/science.1232437.

[69]   A. N. Yaroslavsky, P. C. Schulze, I. V. Yaroslavsky, R. Schober, F. Ulrich, and H.-J. Schwarzmaier, "Optical properties of selected native and coagulated human brain tissues in vitro in the visible and near infrared spectral range," *Phys. Med. Biol.*, vol. 47, no. 12, p. 2059, 2002, doi: 10.1088/0031-9155/47/12/305.

[70]   J. S. Ho *et al.*, "Self-Tracking Energy Transfer for Neural Stimulation in Untethered Mice," *Phys. Rev. Appl.*, vol. 4, no. 2, p. 024001, Aug. 2015, doi: 10.1103/PhysRevApplied.4.024001.

[71]   C. T. Wentz, J. G. Bernstein, P. Monahan, A. Guerra, A. Rodriguez, and E. S. Boyden, "A wirelessly powered and controlled device for optical neural control of freely-behaving animals," *J. Neural Eng.*, vol. 8, no. 4, p. 046021, 2011, doi: 10.1088/1741-2560/8/4/046021.

[72]   K. L. Montgomery *et al.*, "Wirelessly powered, fully internal optogenetics for brain, spinal and peripheral circuits in mice," *Nat. Methods*, vol. 12, no. 10, pp. 969–974, Aug. 2015, doi: 10.1038/nmeth.3536.

[73]   K. Y. Kwon, A. Khomenko, M. Haq, and W. Li, "Integrated slanted microneedle-LED array for optogenetics," in *2013 35th Annual International Conference of the IEEE Engineering in Medicine and Biology Society (EMBC)*, 2013, pp. 249–252, doi: 10.1109/EMBC.2013.6609484.

[74]   K. Kwon and W. Li, "Integrated multi-LED array with three-dimensional polymer waveguide for optogenetics," in *2013 IEEE 26th International Conference on Micro Electro Mechanical Systems (MEMS)*, 2013, pp. 1017–1020, doi: 10.1109/MEMSYS.2013.6474421.

[75]   T. Tokuda *et al.*, "CMOS on-chip bio-imaging sensor with integrated micro light source array for optogenetics," *Electron. Lett.*, vol. 48, no. 6, pp. 312–314, Mar. 2012, doi: 10.1049/el.2011.4087.

[76]   N. Grossman *et al.*, "Multi-site optical excitation using ChR2 and micro-LED array," *J. Neural Eng.*, vol. 7, no. 1, p. 016004, 2010, doi: 10.1088/1741-2560/7/1/016004.

[77]   B. McGovern *et al.*, "A New Individually Addressable Micro-LED Array for Photogenetic Neural Stimulation," *IEEE Trans. Biomed. Circuits Syst.*, vol. 4, no. 6, pp. 469–476, Dec. 2010, doi: 10.1109/TBCAS.2010.2081988.

[78] H. G. Rhew, J. Jeong, J. A. Fredenburg, S. Dodani, P. G. Patil, and M. P. Flynn, "A Fully Self-Contained Logarithmic Closed-Loop Deep Brain Stimulation SoC With Wireless Telemetry and Wireless Power Management," *IEEE J. Solid-State Circuits*, vol. 49, no. 10, pp. 2213–2227, Oct. 2014, doi: 10.1109/JSSC.2014.2346779.

[79] R. Ameli, A. Mirbozorgi, J. L. Néron, Y. LeChasseur, and B. Gosselin, "A wireless and batteryless neural headstage with optical stimulation and electrophysiological recording," in *2013 35th Annual International Conference of the IEEE Engineering in Medicine and Biology Society (EMBC)*, 2013, pp. 5662–5665, doi: 10.1109/EMBC.2013.6610835.

[80] T. Komine and M. Nakagawa, "Fundamental analysis for visible-light communication system using LED lights," *IEEE Trans. Consum. Electron.*, vol. 50, no. 1, pp. 100–107, Feb. 2004, doi: 10.1109/TCE.2004.1277847.

[81] K. Y. Kwon, H.-M. Lee, M. Ghovanloo, A. Weber, and W. Li, "Design, fabrication, and packaging of an integrated, wirelessly-powered optrode array for optogenetics application," *Front. Syst. Neurosci.*, vol. 9, May 2015, doi: 10.3389/fnsys.2015.00069.

[82] B. Y. Chow and E. S. Boyden, "Optogenetics and Translational Medicine," *Sci. Transl. Med.*, vol. 5, no. 177, pp. 177ps5-177ps5, Mar. 2013, doi: 10.1126/scitranslmed.3003101.

[83] L. Madisen *et al.*, "A toolbox of Cre-dependent optogenetic transgenic mice for light-induced activation and silencing," *Nat. Neurosci.*, vol. 15, no. 5, p. 793, May 2012, doi: 10.1038/nn.3078.

[84] Y. Jia, B. Lee, S. A. Mirbozorgi, M. Ghovanloo, W. Khan, and W. Li, "Towards a free-floating wireless implantable optogenetic stimulating system," in *2017 IEEE 60th International Midwest Symposium on Circuits and Systems (MWSCAS)*, 2017, pp. 381–384, doi: 10.1109/MWSCAS.2017.8052940.

[85] I. Trujillo-Pisanty, C. Sanio, N. Chaudhri, and P. Shizgal, "Robust optical fiber patch-cords for in vivo optogenetic experiments in rats," *MethodsX*, vol. 2, no. Supplement C, pp. 263–271, Jan. 2015, doi: 10.1016/j.mex.2015.05.003.

[86] D. S. Freedman, J. B. Schroeder, G. I. Telian, Z. Zhang, S. Sunil, and J. T. Ritt, "OptoZIF Drive: a 3D printed implant and assembly tool package for neural recording and optical stimulation in freely moving mice," *J. Neural Eng.*, vol. 13, no. 6, p. 066013, 2016, doi: 10.1088/1741-2560/13/6/066013.

[87] M. Komatsu, E. Sugano, H. Tomita, and N. Fujii, "A Chronically Implantable Bidirectional Neural Interface for Non-human Primates," *Front. Neurosci.*, vol. 11, 2017, doi: 10.3389/fnins.2017.00514.

[88] X. Bi, T. Xie, B. Fan, W. Khan, Y. Guo, and W. Li, "A Flexible, Micro-Lens-Coupled LED Stimulator for Optical Neuromodulation," *IEEE Trans. Biomed. Circuits Syst.*, vol. 10, no. 5, pp. 972–978, Oct. 2016, doi: 10.1109/TBCAS.2016.2599406.

[89] M. Creed, V. J. Pascoli, and C. Lüscher, "Refining deep brain stimulation to emulate optogenetic treatment of synaptic pathology," *Science*, vol. 347, no. 6222, pp. 659–664, Feb. 2015, doi: 10.1126/science.1260776.

[90] S. Miocinovic, S. Somayajula, S. Chitnis, and J. L. Vitek, "History, Applications, and Mechanisms of Deep Brain Stimulation," *JAMA Neurol.*, vol. 70, no. 2, pp. 163–171, Feb. 2013, doi: 10.1001/2013.jamaneurol.45.

[91] V. Poher *et al.*, "Micro-LED arrays: a tool for two-dimensional neuron stimulation," *J. Phys. Appl. Phys.*, vol. 41, no. 9, p. 094014, 2008, doi: 10.1088/0022-3727/41/9/094014.

[92] N. McAlinden, E. Gu, M. D. Dawson, S. Sakata, and K. Mathieson, "Optogenetic activation of neocortical neurons in vivo with a sapphire-based micro-scale LED probe," *Front. Neural Circuits*, vol. 9, May 2015, doi: 10.3389/fncir.2015.00025.

[93] J. G. McCall *et al.*, "Fabrication and application of flexible, multimodal light-emitting devices for wireless optogenetics," *Nat. Protoc.*, vol. 8, no. 12, p. 2413, Dec. 2013, doi: 10.1038/nprot.2013.158.

[94] S. T. Lee, P. A. Williams, C. E. Braine, D. T. Lin, S. W. M. John, and P. P. Irazoqui, "A Miniature, Fiber-Coupled, Wireless, Deep-Brain Optogenetic Stimulator," *IEEE Trans. Neural Syst. Rehabil. Eng.*, vol. 23, no. 4, pp. 655–664, Jul. 2015, doi: 10.1109/TNSRE.2015.2391282.

[95] M. Hashimoto, A. Hata, T. Miyata, and H. Hirase, "Programmable wireless light-emitting diode stimulator for chronic stimulation of optogenetic molecules in freely moving mice," *Neurophotonics*, vol. 1, no. 1, p. 011002, May 2014, doi: 10.1117/1.NPh.1.1.011002.

[96] F. B. Carr and V. Zachariou, "Nociception and pain: lessons from optogenetics," *Front. Behav. Neurosci.*, vol. 8, Mar. 2014, doi: 10.3389/fnbeh.2014.00069.

[97] A. J. Yeh, J. S. Ho, Y. Tanabe, E. Neofytou, R. E. Beygui, and A. S. Y. Poon, "Wirelessly powering miniature implants for optogenetic stimulation," *Appl. Phys. Lett.*, vol. 103, no. 16, p. 163701, Oct. 2013, doi: 10.1063/1.4825272.

[98] S. K. Arfin, M. A. Long, M. S. Fee, and R. Sarpeshkar, "Wireless Neural Stimulation in Freely Behaving Small Animals," *J. Neurophysiol.*, vol. 102, no. 1, pp. 598–605, Jul. 2009, doi: 10.1152/jn.00017.2009.

[99]   A. D. Mickle *et al.*, "A wireless closed-loop system for optogenetic peripheral neuromodulation," *Nature*, vol. 565, no. 7739, pp. 361–365, Jan. 2019, doi: 10.1038/s41586-018-0823-6.

[100] D. I. McRee and H. Wachtel, "Pulse Microwave Effects on Nerve Vitality," *Radiat. Res.*, vol. 91, no. 1, pp. 212–218, 1982, doi: 10.2307/3575828.

[101] D. Uttamchandani, *Handbook of Mems for Wireless and Mobile Applications*. Elsevier, 2013.

[102] A. A. Bergh and P. J. Dean, "Light-emitting diodes," *Proc. IEEE*, vol. 60, no. 2, pp. 156–223, 1972, doi: 10.1109/PROC.1972.8592.

[103] H. Lee, D. B. Oberman, and J. S. H. Jr, "Reactive ion etching of GaN using CHF3/Ar and C2ClF5/Ar plasmas," *Appl. Phys. Lett.*, vol. 67, no. 12, pp. 1754–1756, Sep. 1995, doi: 10.1063/1.115039.

[104] J. K. Sheu *et al.*, "White-light emission from near UV InGaN-GaN LED chip precoated with blue/green/red phosphors," *IEEE Photonics Technol. Lett.*, vol. 15, no. 1, pp. 18–20, Jan. 2003, doi: 10.1109/LPT.2002.805852.

[105] B. W. Lim *et al.*, "8 × 8 GaN Schottky barrier photodiode array for visible-blind imaging," *Electron. Lett.*, vol. 33, no. 7, pp. 633–634, Mar. 1997, doi: 10.1049/el:19970377.

[106] I. Ichimura, F. Maeda, K. Osato, K. Yamamoto, and Y. Kasami, "Optical Disk Recording Using a GaN Blue-Violet Laser Diode," *Jpn. J. Appl. Phys.*, vol. 39, no. 2S, p. 937, Feb. 2000, doi: 10.1143/JJAP.39.937.

[107] D. M. Dacey and B. B. Lee, "The 'blue-on' opponent pathway in primate retina originates from a distinct bistratified ganglion cell type," *Nature*, vol. 367, no. 6465, pp. 731–735, Feb. 1994, doi: 10.1038/367731a0.

[108] A. Kleinschmidt, B. B. Lee, M. Requardt, and J. Frahm, "Functional mapping of color processing by magnetic resonance imaging of responses to selective P- and M-pathway stimulation," *Exp. Brain Res.*, vol. 110, no. 2, pp. 279–288, Jul. 1996, doi: 10.1007/BF00228558.

[109] "Nitride-based semiconductors for blue and green light-emitting devices - ProQuest." [Online]. Available: http://search.proquest.com/openview/74352578e2717c17891057f6e0d98191/1?pq-origsite=gscholar&cbl=40569. [Accessed: 26-Mar-2017].

[110] B. Fan, K. Y. Kwon, A. J. Weber, and W. Li, "An implantable, miniaturized SU-8 optical probe for optogenetics-based deep brain stimulation," in *2014 36th Annual International*

Conference of the IEEE Engineering in Medicine and Biology Society, 2014, pp. 450–453, doi: 10.1109/EMBC.2014.6943625.

[111] C. A. Carosella, B. Molnar, S. Schiestel, and J. A. Sprague, "Wet Etching of Ion-implanted GaN Crystals by AZ-400K Photoresist," *MRS Online Proc. Libr. Arch.*, vol. 595, Jan. 1999, doi: 10.1557/PROC-595-F99W11.70.

[112] A. Szczęsny, P. Śniecikowski, J. Szmidt, and A. Werbowy, "Reactive ion etching of novel materials—GaN and SiC," *Vacuum*, vol. 70, no. 2–3, pp. 249–254, Mar. 2003, doi: 10.1016/S0042-207X(02)00651-6.

[113] S. J. Pearton, C. R. Abernathy, F. Ren, J. R. Lothian, P. W. Wisk, and A. Katz, "Dry and wet etching characteristics of InN, AlN, and GaN deposited by electron cyclotron resonance metalorganic molecular beam epitaxy," *J. Vac. Sci. Technol. A*, vol. 11, no. 4, pp. 1772–1775, Jul. 1993, doi: 10.1116/1.578423.

[114] B. Humphreys, M. Govett, and A. Goodyear, "The application of high density plasma sources for optoelectronic devicefabrication," *Vacuum*, vol. 51, no. 4, pp. 511–517, Dec. 1998, doi: 10.1016/S0042-207X(98)00243-7.

[115] S. Bouchoule *et al.*, "Reactive ion etching of high optical quality GaN∕sapphire photonic crystal slab using CH4–H2 chemistry," *J. Appl. Phys.*, vol. 101, no. 4, p. 043103, Feb. 2007, doi: 10.1063/1.2433770.

[116] S. Park *et al.*, "Vacuum pump age effects by the exposure to the corrosive gases on the Cr etch rate as observed using optical emission spectroscopy in an Ar/O2/Cl2 mixed plasma," *Thin Solid Films*, vol. 603, no. Supplement C, pp. 154–159, Mar. 2016, doi: 10.1016/j.tsf.2016.01.051.

[117] L. Henry and P. Granjoux, "Novel process for integration of optoelectronic devices using reactive ion etching without chlorinated gas," *Electron. Lett.*, vol. 23, no. 24, pp. 1253-, Nov. 1987, doi: 10.1049/el:19870870.

[118] J. W. Lee, Y. D. Park, J. R. Childress, S. J. Pearton, F. Sharifi, and F. Ren, "Copper Dry Etching with Cl2 / Ar Plasma Chemistry," *J. Electrochem. Soc.*, vol. 145, no. 7, pp. 2585–2589, Jul. 1998, doi: 10.1149/1.1838685.

[119] S. J. Pearton *et al.*, "The incorporation of hydrogen into III-V nitrides during processing," *J. Electron. Mater.*, vol. 25, no. 5, pp. 845–849, doi: 10.1007/BF02666647.

[120] M. E. Lin, Z. F. Fan, Z. Ma, L. H. Allen, and H. Morkoç, "Reactive ion etching of GaN using BCl3," *Appl. Phys. Lett.*, vol. 64, no. 7, pp. 887–888, Feb. 1994, doi: 10.1063/1.110985.

[121] I. Adesida, A. Mahajan, E. Andideh, M. A. Khan, D. T. Olsen, and J. N. Kuznia, "Reactive ion etching of gallium nitride in silicon tetrachloride plasmasa)," *Appl. Phys. Lett.*, vol. 63, no. 20, pp. 2777–2779, Nov. 1993, doi: 10.1063/1.110331.

[122] S. J. Pearton, C. R. Abernathy, and F. Ren, "Low bias electron cyclotron resonance plasma etching of GaN, AlN, and InN," *Appl. Phys. Lett.*, vol. 64, no. 17, pp. 2294–2296, Apr. 1994, doi: 10.1063/1.111648.

[123] C. R. Abernathy *et al.*, "Hydrogen incorporation in GaN, AlN, and InN during Cl2/CH4/H2/Ar ECR plasma etching," *Electron. Lett.*, vol. 31, no. 10, pp. 836–837, May 1995, doi: 10.1049/el:19950558.

[124] I. Adesida, J. N. Kuznia, A. T. Ping, and M. Asif Khan, "Reactive ion etching of gallium nitride using hydrogen bromide plasmas," *Electron. Lett.*, vol. 30, no. 22, pp. 1895–1897, Oct. 1994, doi: 10.1049/el:19941247.

[125] D. Basak *et al.*, "Reactive ion etching of GaN layers using ##IMG## [http://ej.iop.org/images/0268-1242/12/12/019/toc_img1.gif]," *Semicond. Sci. Technol.*, vol. 12, no. 12, p. 1654, 1997, doi: 10.1088/0268-1242/12/12/019.

[126] W. Khan, X. Bi, B. Fan, and W. Li, "GaN LEDs fabricated using SF6 plasma RIE," *Micro Nano Lett.*, vol. 13, no. 9, pp. 1255–1259, 2018.

[127] K. R. Williams, K. Gupta, and M. Wasilik, "Etch rates for micromachining processing-part II," *J. Microelectromechanical Syst.*, vol. 12, no. 6, pp. 761–778, Dec. 2003, doi: 10.1109/JMEMS.2003.820936.

[128] Q. Z. Liu and S. S. Lau, "A review of the metal–GaN contact technology," *Solid-State Electron.*, vol. 42, no. 5, pp. 677–691, May 1998, doi: 10.1016/S0038-1101(98)00099-9.

[129] S. Ruvimov *et al.*, "Microstructure of Ti/Al and Ti/Al/Ni/Au Ohmic contacts for n-GaN," *Appl. Phys. Lett.*, vol. 69, no. 11, p. 1556, 1996, doi: 10.1063/1.117060.

[130] C. Wang and N.-Y. Kim, "Electrical characterization and nanoscale surface morphology of optimized Ti/Al/Ta/Au ohmic contact for AlGaN/GaN HEMT," *Nanoscale Res. Lett.*, vol. 7, no. 1, p. 107, Feb. 2012, doi: 10.1186/1556-276X-7-107.

[131] H.-J. Wang, C.-P. Chen, and R.-J. Jeng, "Polythiophenes Comprising Conjugated Pendants for Polymer Solar Cells: A Review," *Materials*, vol. 7, no. 4, pp. 2411–2439, Mar. 2014, doi: 10.3390/ma7042411.

[132] S. Tachi, K. Tsujimoto, and S. Okudaira, "Low-temperature reactive ion etching and microwave plasma etching of silicon," *Appl. Phys. Lett.*, vol. 52, no. 8, pp. 616–618, Feb. 1988, doi: 10.1063/1.99382.

[133] K. Zhu, "Evolution of surface roughness of AlN and GaN induced by inductively coupled Cl[sub 2]/Ar plasma etching," *J. Appl. Phys.*, vol. 95, no. 9, p. 4635, 2004, doi: 10.1063/1.1688993.

[134] "Cree TR2227 LED Chips." [Online]. Available: http://www.cree.com/LED-Chips-and-Materials/Chips/Chips/TR/TR2227-LED. [Accessed: 16-Oct-2016].

[135] E. Stark, T. Koos, and G. Buzsáki, "Diode probes for spatiotemporal optical control of multiple neurons in freely moving animals," *J. Neurophysiol.*, vol. 108, no. 1, pp. 349–363, Jul. 2012, doi: 10.1152/jn.00153.2012.

[136] J. S. Lee, K.-W. Chang, S.-W. Kim, C. Huh, I.-H. Lee, and S.-J. Park, "Dry etch damage in n-type GaN and its recovery by treatment with an N2 plasma," 2000, doi: 10.1063/1.373438.

[137] H. W. Huang, J. T. Chu, T. H. Hsueh, M. C. Ou-Yang, H. C. Kuo, and S. C. Wang, "Fabrication and photoluminescence of InGaN-based nanorods fabricated by plasma etching with nanoscale nickel metal islands," *J. Vac. Sci. Technol. B Microelectron. Nanometer Struct.*, vol. 24, no. 4, p. 1909, 2006, doi: 10.1116/1.2221317.

[138] N. Okada *et al.*, "Formation of distinctive structures of GaN by inductively-coupled-plasma and reactive ion etching under optimized chemical etching conditions," *AIP Adv.*, vol. 7, no. 6, p. 065111, 2017.

[139] S. Joglekar, M. Azize, M. Beeler, E. Monroy, and T. Palacios, "Impact of recess etching and surface treatments on ohmic contacts regrown by molecular-beam epitaxy for AlGaN/GaN high electron mobility transistors," *Appl. Phys. Lett.*, vol. 109, no. 4, p. 041602, Jul. 2016, doi: 10.1063/1.4959831.

[140] W. Khan and W. Li, "Wafer level fabrication method of hemispherical reflector coupled micro-led array stimulator for optogenetics," in *2017 19th International Conference on Solid-State Sensors, Actuators and Microsystems (TRANSDUCERS)*, 2017, pp. 2231–2234, doi: 10.1109/TRANSDUCERS.2017.7994521.

[141] J. Albero *et al.*, "Fabrication of spherical microlenses by a combination of isotropic wet etching of silicon and molding techniques," *Opt. Express*, vol. 17, no. 8, pp. 6283–6292, Apr. 2009, doi: 10.1364/OE.17.006283.

[142] W. Khan, M. Setien, E. Purcell, and W. Li, "Micro-reflector Integrated Multichannel µLED Optogenetic Neurostimulator with Enhanced Intensity," *Front. Mech. Eng.*, vol. 4, p. 17, 2018.

[143] L. B. Motta-Mena *et al.*, "An optogenetic gene expression system with rapid activation and deactivation kinetics," *Nat. Chem. Biol.*, vol. 10, no. 3, pp. 196–202, Mar. 2014, doi: 10.1038/nchembio.1430.

[144] B. M. Winter *et al.*, "Control of cell fate and excitability at the neural electrode interface: Genetic reprogramming and optical induction," in *Life Sciences Conference (LSC), 2017 IEEE*, 2017, pp. 157–161.

[145] T. D. Kozai *et al.*, "Chronic tissue response to carboxymethyl cellulose based dissolvable insertion needle for ultra-small neural probes," *Biomaterials*, vol. 35, no. 34, pp. 9255–9268, 2014.

[146] J. W. Salatino, K. A. Ludwig, T. D. Kozai, and E. K. Purcell, "Glial responses to implanted electrodes in the brain," *Nat. Biomed. Eng.*, vol. 1, no. 11, p. 862, 2017.

[147] P. D. Wolf, "Thermal Considerations for the Design of an Implanted Cortical Brain–Machine Interface (BMI)," in *Indwelling Neural Implants: Strategies for Contending with the In Vivo Environment*, W. M. Reichert, Ed. Boca Raton (FL): CRC Press/Taylor & Francis, 2008.

[148] L. S. Goldstein, M. W. Dewhirst, M. Repacholi, and L. Kheifets, "Summary, conclusions and recommendations: adverse temperature levels in the human body," *Int. J. Hyperthermia*, vol. 19, no. 3, pp. 373–384, 2003.

[149] J. Haveman, P. Sminia, J. Wondergem, J. van der Zee, and M. Hulshof, "Effects of hyperthermia on the central nervous system: What was learnt from animal studies?," *Int. J. Hyperthermia*, vol. 21, no. 5, pp. 473–487, 2005.

[150] "Silicon wafer — Thermophysical Properties," *NETZSCH Analyzing & Testing*. [Online]. Available: https://www.netzsch-thermal-analysis.com/us/materials-applications/photovoltaics/silicon-wafer-thermophysical-properties/. [Accessed: 31-Jul-2018].

[151] Y. Shin *et al.*, "Characterization of fiber-optic light delivery and light-induced temperature changes in a rodent brain for precise optogenetic neuromodulation," *Biomed. Opt. Express*, vol. 7, no. 11, pp. 4450–4471, Oct. 2016, doi: 10.1364/BOE.7.004450.

[152] Y. Jia *et al.*, "Wireless opto-electro neural interface for experiments with small freely behaving animals," *J. Neural Eng.*, vol. 15, no. 4, p. 046032, 2018.

[153] Y. Jia *et al.*, "A mm-sized free-floating wirelessly powered implantable optical stimulation device," *IEEE Trans. Biomed. Circuits Syst.*, vol. 13, no. 4, pp. 608–618, 2019.

[154] Y. Jia *et al.*, "A mm-sized free-floating wirelessly powered implantable optical stimulating system-on-a-chip," in *2018 IEEE International Solid-State Circuits Conference-(ISSCC)*, 2018, pp. 468–470.

[155] J.-M. Hsu, S. Kammer, E. Jung, L. Rieth, R. A. Normann, and F. Solzbacher, "Characterization of Parylene-C film as an encapsulation material for neural interface devices," in *Conference on Multi-Material Micro Manufacture*, 2007.

[156] W. Khan, Y. Jia, F. Madi, A. Weber, M. Ghovanloo, and W. Li, "Inductively coupled, mm-sized, single channel optical neuro-stimulator with intensity enhancer," *Microsyst. Nanoeng.*, vol. 5, no. 1, pp. 1–12, 2019.

[157] Young-Jun Kim and M. G. Allen, "Integrated solenoid-type inductors for high frequency applications and their characteristics," 1998, pp. 1247–1252, doi: 10.1109/ECTC.1998.678896.

[158] W. Khan, Y. Jia, F. Madi, A. Weber, M. Ghovanloo, and W. Li, "A miniaturized, wirelessly-powered, reflector-coupled single channel opto neurostimulator," in *2018 IEEE Micro Electro Mechanical Systems (MEMS)*, 2018, pp. 174–177, doi: 10.1109/MEMSYS.2018.8346512.

[159] J.-W. Jeong *et al.*, "Wireless Optofluidic Systems for Programmable In Vivo Pharmacology and Optogenetics," *Cell*, vol. 162, no. 3, pp. 662–674, Jul. 2015, doi: 10.1016/j.cell.2015.06.058.

[160] M. Kiani, Uei-Ming Jow, and M. Ghovanloo, "Design and Optimization of a 3-Coil Inductive Link for Efficient Wireless Power Transmission," *IEEE Trans. Biomed. Circuits Syst.*, vol. 5, no. 6, pp. 579–591, Dec. 2011, doi: 10.1109/TBCAS.2011.2158431.

[161] S. A. Mirbozorgi, P. Yeon, and M. Ghovanloo, "Robust wireless power transmission to mm-sized free-floating distributed implants," *IEEE Trans. Biomed. Circuits Syst.*, vol. 11, no. 3, pp. 692–702, 2017.

[162] G. Shin *et al.*, "Flexible Near-Field Wireless Optoelectronics as Subdermal Implants for Broad Applications in Optogenetics," *Neuron*, vol. 93, no. 3, pp. 509-521.e3, Feb. 2017, doi: 10.1016/j.neuron.2016.12.031.

[163] A. Aldaoud *et al.*, "Wireless multichannel optogenetic stimulators enabled by narrow bandwidth resonant tank circuits," *Sens. Actuators Phys.*, vol. 271, pp. 201–211, Mar. 2018, doi: 10.1016/j.sna.2017.12.051.

[164] S. I. Park *et al.*, "Ultraminiaturized photovoltaic and radio frequency powered optoelectronic systems for wireless optogenetics," *J. Neural Eng.*, vol. 12, no. 5, p. 056002, 2015, doi: 10.1088/1741-2560/12/5/056002.

[165] S. I. Park *et al.*, "Soft, stretchable, fully implantable miniaturized optoelectronic systems for wireless optogenetics," *Nat. Biotechnol.*, vol. 33, no. 12, pp. 1280–1286, Dec. 2015, doi: 10.1038/nbt.3415.